

A photograph of a laboratory flume experiment. The flume is a long, narrow channel with green metal walls and yellow-painted bottom rails. Dark water flows through the channel, creating white foam and bubbles. Several small, brightly colored plastic debris items (yellow, green, red) are floating in the water. The text is overlaid on the upper half of the image.

# **Influence of Wave Steepness on the Transport of Marine Plastic Debris in the Nearshore Environment: Insights from Laboratory Flume Experiments**

Camilla Coccozza





# Influence of Wave Steepness on the Transport of Marine Plastic Debris in the Nearshore Environment: Insights from Laboratory Flume Experiments

by

Camilla Coccozza

to obtain the degree of Master of Science  
at the Delft University of Technology,  
to be defended publicly on 30th of June 2025.

|                   |                                   |                       |
|-------------------|-----------------------------------|-----------------------|
| Student number:   | 6070957                           |                       |
| Project duration: | February 10, 2025 – June 30, 2025 |                       |
| Thesis committee: | Dr. A (Anne) Baar                 | TU Delft (supervisor) |
|                   | Dr.ir. RW (Rolf) Hut              | TU Delft (supervisor) |
|                   | Dr.ir. TS (Ton) van den Bremer    | TU Delft (supervisor) |
|                   | Prof. Dr. E (Erik) van Sebille    | UU (Advisor)          |
|                   | ME (Marc) Schneider               | UU (Advisor)          |
|                   | Dr.ir. MA (Matthieu) de Schipper  | TU Delft (Advisor)    |

An electronic version of this thesis is available at <http://repository.tudelft.nl/>.





# Preface

This document is the result of my Master's thesis research on "Influence of Wave Steepness on the Transport of Marine Plastic Debris in the Nearshore Environment: Insights from Laboratory Flume Experiments". It has been written as final project to complete the Environmental Engineering MSc program within the Water Resources Engineering – Regional Hydrology track offered by Delft University of Technology. I was engaged in this research project from February 2025 until June 2025.

The research process was characterized by an experimental campaign conducted in the wave flume available at the Hydraulic Engineering Laboratory within the Civil Engineering and Geosciences faculty of Delft University of Technology. Throughout the process of this research I worked in close collaboration with my colleague L.M.J. (Leanne) Swuste who focused on "Density-Driven Effects on Marine Plastic Beaching: Observations from Laboratory Flume Experiments".

While the outcomes of our research are presented as individual works, the collaboration which allowed for their completion needs to be addressed. The design of the experiments and the data processing methods were jointly developed, this resulted in significant shared efforts on the Theoretical Background and Methodology chapters.

This collaboration is acknowledged throughout the current report via a colour-code system. A coloured line on the left side of the text indicates which author(s) was responsible for each section.

1. **Complete overlap:** These sections were written in collaboration between both authors and overlaps exactly between the two MSc thesis reports.
2. **Partial Overlap:** These sections were originally written in collaboration by both authors but were later adapted slightly to align with the specific research questions addressed in each project.
3. **Individual:** These sections were written individually for each report by the respective author and are specific for the topic addressed in each report.

A more detailed description of the collaboration efforts and the individual contribution of both students within the (partly) overlapping texts can be found in Table H.1.

*Camilla Cocozza  
Delft, June 2025*



# Acknowledgements

This report marks the conclusion of my journey as an Environmental Engineering student. The thesis project has been a challenging and rewarding time where I started to discover what it means to work on a research project from the beginning to the end, with all the difficulties, setbacks, and achievements that come with it. I would like to express my sincere gratitude to everyone who has been involved in the project, offered their support, and contributed to making this experience not only possible but also truly enjoyable.

First, I would like to thank my supervisors. Anne Baar, Rolf Hut, and Ton van den Bremer. Through your inputs, I really understood what it means to value research with everything that it entails. The way your different perspectives complemented each other made it possible for me to always find the direction and support needed.

I would like to thank Cem Sevindik, who adjusted his planning according to our needs and kindly allowed us to use his laboratory setup. Thanks to Marion Tissier and Jaime Arriaga García, who shared their knowledge and high-level study material on waves, without which we would still be lost trying to navigate the complexity of this subject. A big thank you goes to Jimena Medina Rubio, whose extra pair of hands and sharp observations were a real help during the experiments.

A rightful mention goes to the Waterlab staff members. Chantal Willems and Pieter van der Gaag, who were always available to help us out in the lab and shared insightful feedback and ideas on how to best design and perform our experiments. Frank Kalkman, who worked behind the scenes to ensure the electronics were always functioning. Jennifer Rietdijk, who welcomed our confusion around camera calibration, and always did her best to answer our questions. Finally, Arie van der Vlies and Arno Doorn who patiently handled our many requests and turned all our ideas for wooden structures into reality.

The help of Jessamy Mol and Dr. Paul Bayle was precious throughout the whole process. Thank you for sharing your expertise. Your accessibility made a big difference; we always felt welcome to drop by your offices, take a moment of your time, and count on your genuine will to help.

I would like to thank my two colleagues and friends with whom I shared this thesis journey. Leanne Swuste, my dedicated and driven lab partner, whose persistence, energy, and long legs I came to value every step of the way. Iris Haagsma, whose determination and willpower will never stop amazing and inspiring me.

Lastly, I would like to thank everyone who has made my time as a student so special.

To my PoliTo friends with whom I started my academic journey. You contributed to countless memories characterised by a fair share of laughter and tears. Without your support, I am quite sure I would still be stuck dealing with some sort of adiabatic expansion.

To all the amazing people I met in Delft, I would never have hoped to make so many new friends in such a short time. A special mention to my MDP group. We learned together how to appreciate the Savannah slow living, one can of baked beans at a time. I could not have wished for better company to share this adventure with.

To my old, new and extended roommates, thank you for being the safe space I could always count on returning to. There was nothing that a nice meal and your company could not fix.

To my friends from home, whose love never failed to reach me despite the distance and my poor skills in keeping in touch. I am lucky enough to have many reasons to always look forward to coming back.

And finally, I want to express my gratitude to my family, my parents and my sister. You blindly believed in me, supporting any decision I made and trusting I could do it even when I failed to do so.

I am looking forward to the future that awaits me, reassured by the strength of my support system and the academic experience I have gained to face whatever comes my way.





# Abstract

Marine plastic debris has become an established concern as a threat to marine and coastal ecosystems. Despite progress in understanding plastic transport dynamics under deep-water conditions, the characterisation of these processes in the nearshore environment remains incomplete. This poses significant challenges in their parametrisation, essential for the accurate representation of coastal transport dynamics in predictive models.

In this study, experimental measurements of the plastic particles wave-induced transport in intermediate to shallow water depths are presented. The focus is put on the influence of wave steepness as a key parameter affecting the transport of marine plastic debris in the transition from deep water to the shoreline. Its potential as a predictive parameter is investigated through controlled laboratory experiments involving the generation of seven regular breaking wave conditions, characterised by varying offshore steepness, propagating in shallow water depth over a sloped bathymetry.

The results reveal a consistent increase in particle drift speed with increasing offshore wave steepness. While the exact functional nature of the observed positive relationship could not be definitively concluded, the trend appears more likely linear than quadratic, aligning with previous findings for particles deviating from perfect tracers undergoing deep water breaking conditions. Furthermore, wave breaking was observed to play an important role in enhancing particle drift speed. Finally, particle drift speeds were consistently underestimated by the Stokes drift and only partially captured by the wave crest speed estimates, progressively diverging from the former and approaching the latter as offshore steepness increased, though remaining consistently lower than crest speeds. This trend was most recognisable in the breaking zone across all the tested wave conditions.

Overall, the findings suggest offshore wave steepness as a robust predictor for marine plastic debris transport in the nearshore environment, proving its value as a classification parameter for future modelling efforts. By investigating how plastic particles respond to changing wave conditions in the nearshore environment, this study aims to contribute to a better understanding of their dynamics.

---

**Legend:**  100% overlap  90% overlap with minimal adjustments  0% overlap

---





# Contents

|          |   |           |
|----------|---|-----------|
| <b>1</b> | <b>Introduction</b>   | <b>1</b>  |
| <b>2</b> | <b>Theoretical Background</b>                                   | <b>5</b>  |
| 2.1      | Marine Plastic Debris . . . . .                                 | 5         |
| 2.2      | Wave Basics . . . . .   | 5         |
| 2.2.1    | Wavelength . . . . .  | 6         |
| 2.2.2    | Wave Steepness . . . . .  | 7         |
| 2.2.3    | Ursell Number . . . . .   | 7         |
| 2.2.4    | Validity Domain . . . . .                                       | 8         |
| 2.2.5    | Iribarren number . . . . .                                      | 8         |
| 2.3      | Coastal Wave Dynamics . . . . .                                 | 9         |
| 2.4      | Wave Propagation Velocities . . . . .                           | 9         |
| 2.4.1    | Phase and Crest Speed . . . . .                                 | 10        |
| 2.4.2    | Stokes Drift . . . . .  | 10        |
| <b>3</b> | <b>Methodology</b>  | <b>13</b> |
| 3.1      | Experimental Setup . . . . .                                    | 13        |
| 3.1.1    | Experimental Facility . . . . .                                 | 13        |
| 3.1.2    | Wave Gauges . . . . .   | 14        |
| 3.1.3    | Camera set up . . . . .   | 16        |
| 3.2      | Experimental Conditions . . . . .                               | 17        |
| 3.2.1    | Wave Conditions . . . . .                                       | 17        |
| 3.2.2    | Identification of Hydrodynamic Zones within the Flume . . . . . | 19        |
| 3.2.3    | Breaking Zone Locations . . . . .                               | 20        |
| 3.2.4    | Plastic Debris . . . . .  | 21        |
| 3.3      | Experimental Procedure . . . . .                                | 21        |
| 3.4      | Hydrodynamic Conditions . . . . .                               | 22        |
| 3.5      | SWASH Model . . . . .   | 23        |
| 3.6      | Particles Drift . . . . .                                       | 24        |
| 3.6.1    | Preliminary Particle Drift Analysis . . . . .                   | 24        |
| 3.6.2    | Particles Detection: Yolo . . . . .                             | 24        |
| 3.6.3    | Tracking Algorithm . . . . .                                    | 25        |
| 3.6.4    | Trajectory Validation with Tracker . . . . .                    | 25        |
| 3.6.5    | Trajectory Processing . . . . .                                 | 25        |

|          |   |           |
|----------|---|-----------|
| 3.7      | Computation of Wave Propagation Speeds . . . . .                          | 26        |
| 3.7.1    | Phase Speed . . . . .   | 26        |
| 3.7.2    | Crest Speed . . . . .   | 26        |
| 3.7.3    | Stokes Drift . . . . .  | 26        |
| <b>4</b> | <b>Results</b>  | <b>29</b> |
| 4.1      | Overview of Experimental Runs . . . . .                                   | 29        |
| 4.2      | Hydrodynamic Conditions and Wave Characterisation . . . . .               | 30        |
| 4.2.1    | Comparison of Target and Generated Wave Conditions . . . . .              | 30        |
| 4.2.2    | SWASH Model Output Validation . . . . .                                   | 31        |
| 4.2.3    | Delineation of Zones . . . . .  | 34        |
| 4.3      | Particle Transport. . . . .   | 35        |
| 4.3.1    | Particle Horizontal Trajectories . . . . .                                | 36        |
| 4.3.2    | Particle Horizontal Drift Speed Along the Flume . . . . .                 | 37        |
| 4.4      | Wave Propagation Velocities. . . . .                                      | 39        |
| 4.4.1    | Stokes Drift . . . . .  | 39        |
| 4.4.2    | Crest Speed . . . . .   | 41        |
| 4.4.3    | Phase Speed and Crest Speed . . . . .                                     | 42        |
| 4.4.4    | Particle Drift Speed vs. Wave Propagation Velocities . . . . .            | 43        |
| <b>5</b> | <b>Discussion</b>   | <b>49</b> |
| 5.1      | MPD Horizontal Drift Speed and Wave Steepness . . . . .                   | 50        |
| 5.2      | Evolution of MPD Horizontal Transport . . . . .                           | 51        |
| 5.3      | MPD Horizontal Drift Speed and Wave Propagation Speed Estimates . . . . . | 52        |
| 5.4      | Limitations and Assumptions . . . . .                                     | 53        |
| 5.5      | Further Research. . . . .   | 56        |
| <b>6</b> | <b>Conclusion</b>   | <b>59</b> |
| <b>A</b> | <b>Camera Calibration and Distance Conversion</b>                         | <b>65</b> |
| A.1      | Camera Distortion . . . . .   | 65        |
| A.2      | Distance Conversion . . . . .   | 65        |
| <b>B</b> | <b>Initial Testing and Setup Refinement</b>                               | <b>67</b> |
| B.1      | Spin-up Time . . . . .  | 67        |
| B.2      | Instrument Deployment Strategy . . . . .                                  | 67        |
| B.3      | Tipping point . . . . .   | 68        |
| B.4      | Cameras Setup Variability Across Wave Conditions . . . . .                | 69        |
| <b>C</b> | <b>Preliminary Particle Drift Analysis</b>                                | <b>71</b> |
| C.1      | Total Travel Velocity . . . . .   | 71        |
| C.2      | Zonal Travel Velocity . . . . .   | 73        |

---

|   |           |
|---|-----------|
| <b>D SWASH Model</b>                        | <b>75</b> |
| D.1 Model Input . . . . .                   | 75        |
| D.1.1 Command File . . . . .                | 75        |
| <b>E YOLO Detection Model</b>               | <b>79</b> |
| <b>F Results</b>                            | <b>81</b> |
| F.1 SWASH Model Output Validation . . . . . | 81        |
| <b>G Code and Data Availability</b>         | <b>85</b> |
| <b>H Contribution Statement</b>             | <b>87</b> |





# Introduction

Plastic pollution represents a clear example of the global impact of human activity on natural ecosystems. With around 60% of all plastic ever produced accumulating in landfills or in natural environments (Geyer et al. 2017), its presence has become an established concern. After entering the environment, the durability and buoyancy of plastic allow for its large-scale transport, ultimately reaching the ocean, where marine plastic debris has been detected across all major basins (Geyer et al. 2017).

Given its properties, according to Villarrubia-Gómez et al. (2018), marine plastic contamination meets two out of the three requirements to be defined as a chemical pollution planetary threat being both globally ubiquitous and irreversible.

The environmental consequences of marine plastic debris are highly considered by regional and local governments, communities and stakeholders, who aim to minimise its impact on marine and coastal communities (Compa et al. 2019), making it a global challenge for society. The main actions to mitigate, assess and prevent its impacts are defined by the United Nations Organization in the Sustainable Development Goal number 14 "Life below water" (Poulain-Zarcos et al. 2024).

Despite concerns regarding plastic pollution, the actual dynamics and amounts and their ecological implications are not fully understood (Hale et al. 2020). A large mismatch is observed between the estimates of land-generated solid plastic waste that enters coastal waters and the total amount of positively buoyant marine plastic debris found at the ocean surface (Onink et al. 2021; Van Sebille et al. 2020). While an estimated 1.15–12.7 million tons of plastic enter the ocean per year (Onink et al. 2021), less than 0.3 million tonnes are measured at sea (Van Sebille et al. 2020). With approximately half of all plastics produced being less dense than seawater, and thus expected to float at sea (Geyer et al. 2017), this imbalance is not explained, and a large fraction of floating marine plastic debris remains unaccounted for. According to Onink et al. (2021), part of the discrepancy between current plastic input estimates and estimates of floating plastic debris in the open ocean is due to high amounts of beached and coastal MPD. Substantial amounts of the missing MPD are hypothesised to end up on coastlines through natural transport processes, with local concentrations varying between 0 and  $647 \text{ kg km}^{-1}$  (Onink et al. 2021).

Coastal zones are of particular interest for marine plastic pollution as they represent the interface between land and sea. They serve as a main source and sink of marine litter coming in as river emissions and lost or discarded fishing gear, and returned by beaching mechanisms (Löhr et al. 2017). Although the main interactions between humans, plastic and marine life occur near the coast, observations of nearshore plastic behaviour and the interacting processes, such as wind, waves and currents, are not yet fully understood and require further investigation (Alsina et al. 2020). Studying the dynamics and interactions of marine plastic debris in coastal environments is therefore of main interest given the dual source-sink role and the still existing open questions.

As a result of the growing concern surrounding marine plastic pollution, the scientific interest regarding the mechanisms behind the presence of plastic in marine environments has increased significantly in the past decade (Compa et al. 2019). The efforts put into understanding the behaviour and environmental role of marine plastic pollution have resulted in a number of publications studying the problem from different perspectives and using different methodologies. Nonetheless, the current knowledge on plastic fluxes, pathways, and fate is not complete (Van Sebille et al. 2020). Oceanographers have been traditionally interested in transport processes within the water column, focusing on how waves, currents, and tides influence the movement of particles through the ocean's depth. On the other side, the actual transition of plastic from floating near the coast to landing on the ground is not as thoroughly considered (Pawlowicz 2021). Most of the existing global numerical models predicting plastic fluxes do not explicitly consider the plastic motion in coastal regions (Alsina et al. 2020), relying on probabilistic approaches to represent the nearshore beaching process (Li et al. 2023).

Significant challenges remain regarding the modelling of plastic transport in near-coastal and surf-zone regions, including the washing-up of plastics on beaches. Better understanding of the physical processing driving plastic beaching is therefore needed to improve these models (Sutherland et al. 2023). The lack of actual data on the physical beaching processes, and the choice of alternative approaches to parametrise it, can be attributed to the fact that most research on marine plastic debris transport is focused on oceanic scales and overlooks coastal processes (Jalón-Rojas et al. 2019). The reliance on statistical methods to represent the interactions of marine plastic debris in coastal zones can therefore result in underestimations of the beached amounts and consequently lead to incorrect modelling, forecasting and warning of beaching events, possibly causing environmental and economic losses (Li et al. 2023).

The hydrodynamics in coastal areas are highly complex due to combined forces from wave, wind, tide, and currents, among which, wave action plays the most relevant role (Li et al. 2023). As waves propagate from deep water to the shoreline, they undergo major changes in shape characterised by an increase in steepness, which leads to sharp crests and flat troughs culminating in wave breaking, after which waves collapse and start surfing towards the shore. Wave steepness was therefore identified to be one of the main parameters controlling the horizontal wave-induced transport (Poulain-Zarcos et al. 2024) and chosen as the main research variable for the current study.

A growing body of literature has been focusing on investigating the role of wave steepness in driving marine plastic debris transport. These experimental efforts have been mainly focused on the deep-water transport. He et al. (2016), Huang et al. (2013), Xiao et al. (2025), and Ross Calvert et al. (2021) conducted experiments in deep water regimes for non-breaking regular waves or wave groups. Lenain et al. (2019), Calvert et al. (2024), and Eeltink et al. (2023) included the effect of breaking in their investigation for deep-water marine plastic debris transport. Recent experiments conducted by Alsina et al. 2020 and Núñez et al. 2023 were performed in intermediate to shallow water conditions and included a simulated beach in their setup. Nonetheless, Alsina et al. (2020) considered regular non-breaking waves, whereas Núñez et al. (2023) focused their investigation on the distribution patterns of marine plastic debris rather than their transport behaviour. The mentioned studies agree on the influence of wave steepness on the drift of plastic particles, showing that increasing wave steepness results in increased drift speed of plastic particles. This positive relationship is observed to be influenced by relative particle size and the occurrence of wave breaking. The presence of the mentioned literature studies highlights the relevance of steepness as a variable driving marine plastic debris transport. Despite these significant contributions, there remains a clear research gap concerning the transport dynamics of marine plastic debris in coastal shallow-water environments characterised by breaking waves.

The current study aims to contribute to the understanding of nearshore plastic transport dynamics by investigating the influence of offshore steepness on the horizontal drift speed of plastic particles undergoing breaking waves travelling over a sloped bottom in intermediate to very shallow water regimes. This was achieved by conducting controlled laboratory flume experiments aimed to address the following research question: "How does wave steepness influence the nearshore horizontal transport and beaching of marine plastic debris under controlled wave conditions?"



The overall research was guided by sub-questions with the goal of effectively characterising the mentioned marine plastic debris transport dynamics: Firstly, is there a clear relationship between offshore steepness and the transport of plastic particles at the coast? If so, at which stage along the particle trajectories does the change in offshore wave steepness have the greatest impact? Secondly, how does the breaking zone influence the horizontal drift speed of marine plastic debris in the nearshore environment? Thirdly, to what degree do characteristic wave propagation speeds, such as crest speed and Stokes drift, accurately represent the actual drift speed experienced by plastic particles? Lastly, can offshore wave steepness be used as a predictor for classifying plastic transport regimes in nearshore environments?

Controlled laboratory experiments were selected to enable the isolation of the effect of wave steepness, which was considered necessary for describing the highly complex coastal transport dynamics. Offshore wave steepness was selected as a study variable according to its relevance as a driver of particle transport. Its importance is considered to be even more accentuated in the nearshore environment where waves non-linearity progressively increases while propagating in the onshore direction. The study aims to understand whether offshore steepness can represent a valid predictor for classifying plastic transport regimes in nearshore environments, linking offshore wave characteristics to the intensity of nearshore drift, despite not capturing local dynamics directly.

The observed particle drift speed was compared to characteristic wave propagation speeds, the Stokes drift and the crest speed. The Stokes drift refers to the net drift velocity in the wave propagation direction experienced by a particle floating on the free surface of a surface gravity wave (Van Sebille et al. 2020). In other words, it corresponds to the difference in wave-averaged velocity following a particle (Lagrangian) and in a stationary reference frame (Eulerian) (Van den Bremer et al. 2017). The crest speed instead refers to the speed at which the highest point of a wave moves across the water surface. The comparison was conducted in order to understand whether marine plastic debris transport in the nearshore environment would align more closely with either of these mechanisms and how wave steepness would influence the extent to which particle drift speed corresponds to one speed estimate over the other.

This investigation is considered highly relevant as previous research conducted by Eeltink et al. (2023), Xiao et al. (2025), and Calvert et al. (2024) highlighted how Stokes drift alone is insufficient to describe the actual transport of objects by surface waves. By definition, the wave-induced transport mechanism is driven by the Lagrangian-mean velocity, which includes both the Stokes drift and the wave-induced Eulerian-mean velocity. In addition, on the rotating Earth, the Eulerian flow is itself modified by surface waves. The Coriolis force in combination with the Stokes drift drives an Eulerian-mean current in the turbulent upper-ocean boundary layer (Calvert et al. 2024), the Ekman–Stokes flow, which needs to be added to the Stokes drift to properly estimate the wave-induced Lagrangian-mean flow (Higgins et al. 2020). While this contribution is not addressed in the context of the current laboratory experiments, it remains important to acknowledge its role. Indeed, on a global scale, the mentioned Ekman–Stokes flow has significant consequences for floating marine litter accumulation patterns (Cunningham et al. 2022).

Additionally, wave breaking was observed to substantially increase the transport of marine plastic debris. Lenain et al. (2019), Deike et al. (2017), Eeltink et al. (2023), and Xiao et al. (2025) provided experimental proof of the influence of deep-water breaking on the drift of particles, which was assessed to increase by one order of magnitude considering breaking and non-breaking deep water conditions. It is therefore hypothesised that a drift enhancement driven by breaking will occur for the current experimental conditions. The dynamics in the breaking zone are specifically investigated, aiming to extend the conclusion of breaking-driven particles drift enhancement to coastal environments. Lastly, the characteristics of the plastic debris itself, mainly size, shape and density, play an important role in the way it is transported by waves. Plastic particles deviating from the perfect Lagrangian tracers have been shown to result in different wave-induced mean transport (Alsina et al. 2020; Calvert et al. 2024; Huang et al. 2013), progressively deviating from the Stokes-dominated drift as the relative size of the objects compared to the wave dimensions increases.

By addressing the proposed research questions, this study sets the goal of improving the understanding of wave steepness as a nearshore hydrodynamic characteristic driving the transport of

marine plastic debris. The results are intended to support the refinement of coastal plastic transport parameterisation in numerical models. By eventually contributing to more accurate predictions of plastic pollution pathways, these insights, together with the emerging literature on the fate of marine plastic debris, hold potential for informing the development of effective coastal management and mitigation strategies in the face of growing marine plastic pollution.

This report is organised as follows. Chapter 2 presents the main concepts required to properly understand the implications of the research. Chapter 3 outlines the methodology that allowed for the observation of the results presented in Chapter 4. Chapter 5 provides a discussion of the findings, the limitations of this study and the recognised potential for further research. Appendices A, B, C, D, and E provide detailed information on specific aspects of the methodology. Appendix F presents supporting data to the Results chapter. A direct link to a GitHub repository where the Python scripts and data are made available can be found in Appendix G. Finally, Appendix H presents a statement of the contribution to the current work.

---

**Legend:**  100% overlap  90% overlap with minimal adjustments  0% overlap

---

# Theoretical Background

This chapter provides the theoretical background necessary to follow the present research. Concepts such as marine plastic debris and fundamental wave parameters are introduced, as well as an overview of the coastal flow dynamics and wave propagation velocities.

## 2.1. Marine Plastic Debris

Marine plastic debris (MPD) is defined as waste created by human activities entering the marine ecosystem. It consists of mixtures of particles with varying size, shape and chemical composition (Van Sebille et al. 2020) which can be found floating on the surface, suspended in the water column, or deposited on the seabed. The primary contributors to MPD are land-based sources such as mismanaged waste and urban runoff which reach the marine environments through river discharge. Sea-based sources, on the other hand, consist of fishing, shipping and touristic activities, which cause direct delivery of plastic particles into the sea (Löhr et al. 2017).

The characteristics of MPD is subject to change over time due to multiple processes, such as embrittlement, fragmentation, bio-fouling, weathering and erosion (Van Sebille et al. 2020). The physical, chemical, and biological processes in the ocean can alter the size, shape, and density of plastic debris. These changes, along with the MPD original characteristics, lead to a wide range of variations in their size, shape, and density.

This research specifically focuses on floating macroplastics particles with densities lower than seawater, which allows them to remain buoyant and interact predominantly with the surface wave dynamics. It is important to note that 'floating plastic' does not consistently remain at the surface; it may temporarily submerge due to ocean turbulence and breaking waves. Nevertheless, owing to its positive buoyancy, it will ascend back to the surface.

## 2.2. Wave Basics

This research focuses on the behaviour of ocean waves as they approach the shoreline, particularly in the context of the interaction of waves with plastic particles. To understand these dynamics, it is essential to first introduce the fundamental characteristics of ocean waves and the theoretical framework used to describe them.

Waves can be described as disturbances that move through a material, such as water, over time and space. These disturbances typically occur over distances and times much larger than the wave's own wavelength and period (Holthuijsen 2007). In this context, a wave refers to the vertical movement of the water surface. In natural ocean settings, ocean wave behaviour is influenced by multiple interacting forces, including wind, tides, and currents. These factors can significantly affect wave

transformation and particle transport. These dynamics and transformations make the study of waves complex, especially in coastal areas, and thus waves are typically assumed to be sinusoidal, periodic waves under idealized conditions, which allows for simplified mathematical descriptions such as linear wave theory.

The main key parameters used throughout this study include:

- **Wave height** ( $H$ ): the vertical distance from trough to crest.
- **Wave period** ( $T$ ): the time it takes for two successive wave crests to pass a fixed point.
- **Water depth** ( $h$ ): the vertical distance from the still water surface to the seabed.
- **Wavelength** ( $\lambda$ ): the distance between two consecutive wave crests or troughs. The wavelength depends on the water depth and the wave period.
- **Wave frequency** ( $f$ ): the inverse of the period,  $f = \frac{1}{T}$ .
- **Wave number** ( $k$ ): defined as  $k = \frac{2\pi}{\lambda}$ .
- **Angular frequency** ( $\omega$ ): given by  $\omega = 2\pi f$ .

This research involved the generation of a train of regular, or monochromatic, waves. The term monochromatic wave refers to the simplest type of wave, characterized by a single value of wave height and wave period. This kind of wave is typically employed in laboratory flume studies as, if the wave's height is small enough compared to its wavelength, its behaviour can be approximated to a sinusoidal variation in surface water elevation and therefore described by linear wave theory (Soulsby 1997).

Given the use of a regular wave train, the wave conditions in this research are fully defined by specifying three input parameters: the wave period ( $T$ ), water depth ( $h$ ), and wave height ( $H$ ). Once these primary parameters are known, all other key wave characteristics—such as wavelength, and dimensionless numbers like the Ursell and Iribarren numbers—can be derived using established theoretical relationships. The following section presents the relevant formulas used to compute the mentioned parameters.

### 2.2.1. Wavelength

The wavelength  $L$  refers to the horizontal distance between two successive wave crests. The dispersion relationship in Equation 2.1 provides an approximation of the wavelength based on wave period and water depth, as wave motion is influenced by both gravity and depth-dependent restoring forces.

$$L = \frac{gT^2}{2\pi} \tanh\left(\frac{2\pi d}{L}\right) \quad (2.1)$$

Where:

- $L$  = wavelength [m]
- $g$  = gravitational acceleration ( $\approx 9.81 \text{ m/s}^2$ )
- $T$  = wave period [s]
- $d$  = water depth [m]

This is an implicit expression which requires an iterative procedure to approximate the wavelength for a given period and depth. Explicit expressions that approximate the solution are available and widely

used, in this context the Fenton approximation was applied (Fenton 1988). Formula 2.2 describes the Fenton approximation (Holthuijsen 2007).

$$kd \approx \frac{\alpha + \beta^2 (\cosh \beta)^{-2}}{\tanh \beta + \beta (\cosh \beta)^{-2}} \quad (2.2)$$

This approximation takes the linear dispersion relation and corrects it for a depth-dependent term. It works well for the varying water depths used in the setup. The solution computed with this method is exact for deep-water and shallow-water regimes and presents an error in wave number ( $k$ ) which is less than 0.05% in all other conditions. The method consists in solving equation 2.1. To use formula 2.2, the parameters  $\alpha$  and  $\beta$  need to be determined. To do so,  $L_0$  and  $k_0$  are to be computed as deep-water approximations of the wavelength and wave number by using relations 2.3 and 2.4.

$$L_0 = \frac{gT^2}{2\pi} \quad (2.3)$$

$$k_0 = \frac{2\pi}{L_0} \quad (2.4)$$

Factor  $\alpha$  can be obtained from the previously computed  $k_0$  by solving equation 2.5.

$$\alpha = k_0 h = \frac{4\pi^2 d}{gT^2} \quad (2.5)$$

Factor  $\beta$  can be then obtained from  $\alpha$  by solving equation 2.6.

$$\beta = \alpha (\tanh \alpha)^{-1/2} \quad (2.6)$$

From the result of the Fenton relation, 2.2, the approximation for the wavelength can be eventually obtained using equation 2.7.

$$L = \frac{2\pi h}{kd} \quad (2.7)$$

### 2.2.2. Wave Steepness

Wave steepness describes the ratio between the wave height ( $H$ ) and the wavelength ( $L$ ), representing how "steep" the wave profile is. Offshore steepness refers to this ratio in deep-water before the wave begins to transform due to its interaction with the sloped bottom throughout regions with decreasing depth. The offshore steepness can be estimated using the definition presented in 2.8.

$$steepness = a \cdot k = \frac{H}{2} \cdot \frac{2\pi}{L} = \frac{\pi H}{L} \quad (2.8)$$

### 2.2.3. Ursell Number

The Ursell number is defined as a dimensionless parameter that helps determine wave breaking. For the wave conditions used in this study, the Ursell number was assessed to ensure that the waves do not break immediately at the wave paddle. In the context of the current study, an Ursell number value below a threshold of 25 ensures that the waves remain in non-breaking conditions as they leave the wave generator paddle (Holthuijsen 2007).

The Ursell number was determined using the formula 2.9.

$$U_r = \frac{H_0 \cdot L^2}{h^3} \leq 25 \quad (2.9)$$

where  $H_0$  is the wave height in metres,  $h$  is the water depth in metres and  $L$  is the wavelength in metres which has to be large compared to the depth ( $L \gg h$ ).

#### 2.2.4. Validity Domain

To ensure proper wave generation in the flume to comply with the operational constraints of the wave maker, the input wave conditions were checked to fall within the valid range of linear or second-order Stokes wave theory. This was done by calculating the relative depth and wave steepness (Equations 2.10 and 2.11) and comparing them to known theory limits. Figure 3.5 shows that the tested conditions fall within an acceptable range for the experiment.

$$relative\_depth = \frac{h}{gT^2} \quad (2.10)$$

$$relative\_steepness = \frac{H}{gT^2} \quad (2.11)$$

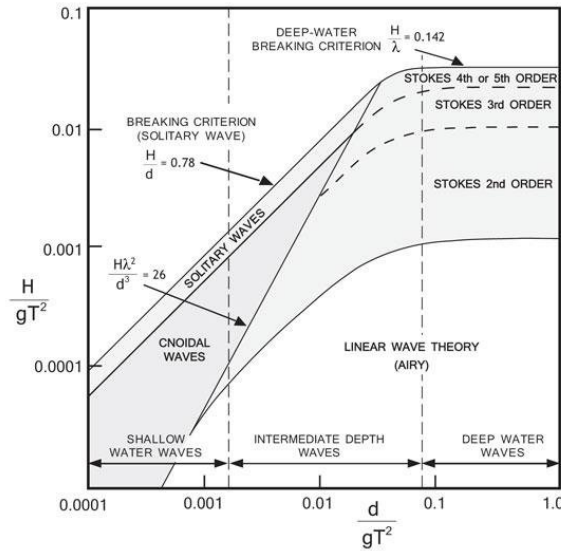


Figure 2.1: Ranges of applicability of the various wave theories (Holthuijsen 2007).

#### 2.2.5. Iribarren number

Wave breaking is the most non-linear process influencing waves in coastal waters (Holthuijsen 2007). To predict the type of breaking, empirical formulas are often used—most notably, the Iribarren number, which serves as a key indicator for distinguishing between different breaker types. This dimensionless parameter is used to distinguish between spilling, plunging, collapsing, or surging waves. Spilling breakers occur on gentle slopes and gradually lose energy as the wave crest spills forward. Plunging breakers are more energetic and form a curling motion with a sudden crash, typically seen on moderate slopes. Collapsing and Surging breakers appear on steep slopes and do not break in the traditional sense but rush up the slope with high speed. Identifying the breaker type was relevant as it gives an indication on the energy dissipation and coastal or experimental wave dynamics. The Iribarren number was calculated using formula 2.12.

$$\xi_0 = \frac{\tan \alpha}{\sqrt{H_0/L_0}} \quad (2.12)$$

Where  $\xi_0$  is the Iribarren number,  $\alpha$  is the beach slope angle,  $H_0$  is the deep-water wave height and  $L_0$  is the deep-water wavelength.

in which:

$$\begin{aligned} \text{spilling:} & \quad \text{if } \xi_\infty < 0.5 \\ \text{plunging:} & \quad \text{if } 0.5 < \xi_\infty < 3.3 \\ \text{collapsing or surging:} & \quad \text{if } \xi_\infty > 3.3 \end{aligned}$$

## 2.3. Coastal Wave Dynamics

During the propagation from deep water to the shoreline, waves undergo major changes in shape due to the interaction with the seabed (Alsina et al. 2020).

Deep-water waves approaching the shore start to feel the presence of the seabed, where friction and decreasing depth triggers a non-linear evolution of the waves. As waves approach shallower water, their height increases and their shape becomes horizontally asymmetric, with steep crests and flatter troughs—a process known as shoaling. As waves move further towards the shore, the steepness of the wave front continues to increase, causing instability and eventually degenerating into wave breaking. The breaking front of the wave (surf bore) starts dissipating wave energy while propagating shoreward. Once the shore is reached, friction and gravitational forces cause the surf bore to decelerate and run up on the beach. As the forward motion ceases, water accelerates in the offshore direction during the backwash phase concluding the beach run-up/run-down process. All the mentioned interactions between wave energy and shoreline take place in the nearshore environment (Van der Zanden 2016; Van Sebille et al. 2020) and are visualized in Figure 2.2.

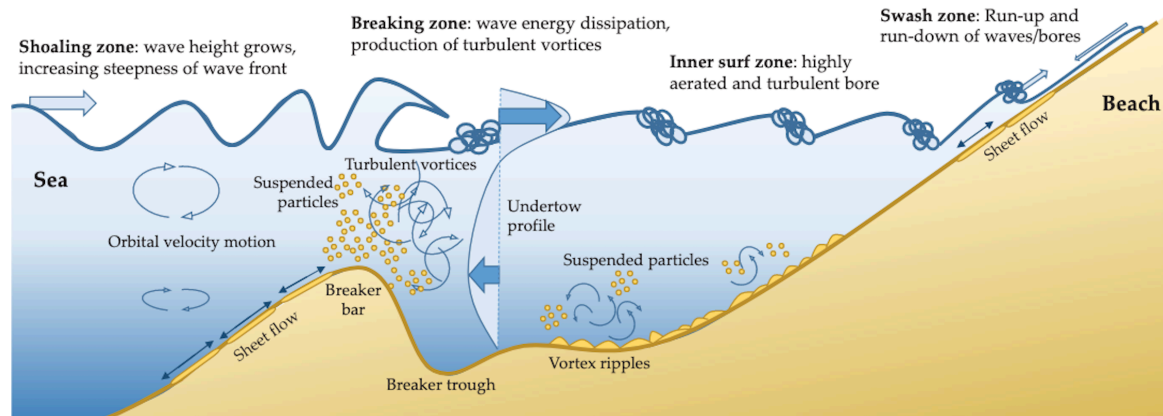


Figure 2.2: Conceptual representation of cross-shore processes in the near-shore region from (Van der Zanden 2016).

## 2.4. Wave Propagation Velocities

To better understand the driving mechanisms behind particle transport, the drift velocities of the MPD were compared to characteristic wave propagation speeds. This comparison helps to place the observed particle dynamics in the broader context of wave-particle interactions. The term wave propagation speed refers to the different characteristic speeds at which different components of a wave field move. Within this research this includes the phase speed, crest speed and Stokes drift. The definition of these components are given in the following sections.

### 2.4.1. Phase and Crest Speed

The phase speed refers to the speed at which a specific phase of the wave travels. Crest speed is the actual speed of the crest itself. For waves that can be described using linear wave theory, the phase speed can be determined using Formula 2.13.

$$c = \frac{\omega}{k} = \sqrt{\frac{g}{k} \tanh(kh)} \quad (2.13)$$

In which:

- $c$  is the phase speed [m/s],
- $\omega$  is the angular frequency [rad/s],
- $k$  is the wave number [rad/m].
- $h$  is the water depth [m].
- and  $g$  is the gravitational constant [ $m/s^2$ ]

This formula can be rewritten to be expressed in terms of wave height, water depth and wave period, which results in 2.14.

$$c = \left( \frac{gT}{2\pi} \right) \tanh \left( \frac{2\pi h}{L} \right) \quad (2.14)$$

For linear waves in deep water, the crest speed is expected to match the phase speed as the wave maintains its shape as it propagates. Waves become increasingly non-linear as they propagate shoreward, the phase speed for non-linear waves is then expected to be higher (Tissier et al. 2011). Linear wave theory allows for reasonable description of wave celerity for deep water, nonetheless, corrections are needed to account for non-linearities during the shoreward movement.

Formulation 2.15 asymptotically approaches the non-linear dispersion relation derived by Hedges (1976) for shallow water, with the modification introduced by Booij (1981) (Martins et al. 2021). This appears to be an upper bound for the propagation speed of wave components in the surf zone (Martins et al. 2021).

$$c = \sqrt{gh(1 + \varepsilon)} \quad (2.15)$$

In which:

- $c$  is the non-linear phase speed [m/s],
- $g$  is the gravitational constant [ $m/s^2$ ],
- $h$  is the water depth [m],
- $\varepsilon$  is the local wave steepness [-].

### 2.4.2. Stokes Drift

The Stokes drift refers to the net drift speed in the wave propagation direction, experienced by a particle floating on the free surface of a surface gravity wave (Van Sebille et al. 2020). In other words, the Stokes drift speed is the difference between the average Lagrangian flow velocity (velocity at which the particle moves) and the average Eulerian flow velocity of the fluid (velocity at which the water moves) (Van Sebille et al. 2020). This happens as particles exposed to a surface wave field travel faster at the top of their orbits than at the bottom, and thus spend more time in crests where



their velocity is positive (Van Sebille et al. 2020).

Stokes drift depends on the shape of the wave, it is proportional to the square of the wave steepness, defined as wave height over wavelength (Soulsby 1997). In coastal areas where waves increase in steepness until they break, the Stokes drift can be especially important for MPD transport.

The Stokes drift can be estimated by applying the derivation for general water depth formalized by Ursell and presented in Equation 2.16 (Van den Bremer et al. 2017). This expression is referred to as "mass-transport velocity" and describes the net motion in the direction of wave propagation.

$$\bar{U} = \frac{a^2 \sigma k \cosh 2k(z - h)}{2 \sinh^2 kh} \quad (2.16)$$

Where:

- $\bar{U}$  is the Stokes drift velocity at elevation  $z$
- $a$  is the wave amplitude
- $\sigma$  is the angular frequency of the wave
- $k$  is the wave number
- $z$  is the vertical coordinate ( $z = 0$ )
- $h$  is the water depth

---

**Legend:** ■ 100% overlap ■ 90% overlap with minimal adjustments ■ 0% overlap

---



# 3

## Methodology

This chapter presents the methodology used to investigate the influence of wave steepness on the beaching behaviour of marine plastic debris in a laboratory flume. The experimental setup is described in detail in order to provide a reproducible account of how this research was conducted. An overview of the flume setup is provided, as well as a description of the tested wave conditions and the different measurement tools. In addition, the use of a SWASH numerical model to simulate wave conditions and guide the design of the experimental campaign is justified and explained in this context.

### 3.1. Experimental Setup

The defined research question *"How does wave steepness influence the nearshore horizontal transport and beaching of marine plastic debris under controlled wave conditions?"* was addressed by conducting experiments in a laboratory flume available at the Hydraulic Engineering Laboratory (HEL) of the Civil Engineering and Geosciences faculty of TU Delft.

During the data collection phase, plastic particles were placed into the flume before the waves breaking point, and their trajectory was tracked until they stabilised on the slope and were considered beached. Multiple experimental runs were repeated by changing the offshore steepness of the generated waves in order to assess its influence on the beaching behaviour of the plastic particles. In the following sections, the experimental setup, measurement tools, and procedure are described in further detail.

#### 3.1.1. Experimental Facility

The experiments were carried out in the Wave Flume presented on the left-hand side of Figure 3.1, available at the HEL as a state-of-the-art wave flume for (MSc) education and research (TU Delft Faculty of Civil Engineering and Geosciences n.d.). The flume presents effective dimensions of 39 metres in length, 0.79 metres in width and 1 metre in height.

Waves can be generated inside the flume using an electrically controlled piston-type wave generator with a maximum stroke of 2 metres, allowing the piston to move up to 2 metres horizontally during its oscillation cycle. The wave generator is capable of reproducing a wide range of wave types and conditions, defined by the user through a user-friendly interface. The machine is equipped with an Active Reflection Compensation system (ARC), which can be activated to minimise wave reflection by dynamically adjusting the motion of the piston.

Preliminary experiments were conducted in the Sediment Flume of the HEL, shown on the right-hand side of Figure 3.1. This flume presents similar dimensions as the Wave Flume (length: 39 metres, width: 0.76 metres, height: 0.85 metres) and is equipped with an equivalent wave generation system.

The similarities between the two flumes allowed for the testing and familiarisation of the available equipment as well as the definition of the experimental design for the data collection campaign prior to its actual start.



Figure 3.1: Wave Flume (left) and Sediment Flume (right) inside the Hydraulic Engineering Laboratory of TU Delft (TU Delft Faculty of Civil Engineering and Geosciences n.d.).

The Wave Flume in its original condition presents a flat bottom. For this experimental campaign, a timber slope was installed inside the flume to simulate a beach profile. The bed was kept horizontal for the first 8 meters. This first flat section was followed by a 1:40 slope, gradually rising to a final height of 60 cm, as illustrated in Figure 3.2. The timber slope has a smooth veneered surface, smoother than most real beaches, as they consist of sand or gravel. This difference in roughness can affect the dynamics of how the waves and the plastics interact with the surface compared to the real world. However, a timber slope was chosen due to practical and technical constraints associated with replicating a sand beach in the flume environment.

#### Total overview of set up (scaled)

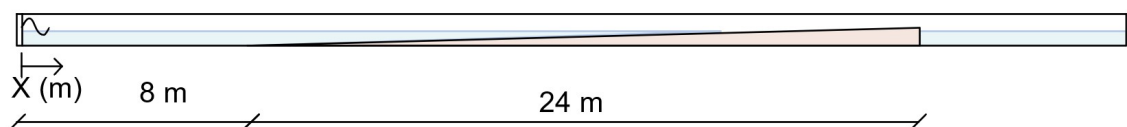


Figure 3.2: Schematic showing the beach profile dimensions within the flume scaled to reality.

#### 3.1.2. Wave Gauges

A set of six wave gauges for the measurement of dynamically varying water levels was installed along the horizontal direction of the flume as depicted in Figure 3.3. The instruments consist of a probe and a control unit. In these electric conductivity-based wave gauges, the probe is made of two parallel stainless steel rods, which function as electrodes. The sensor outputs an analogue signal expressed in Volts that is linearly related to the water level between the rods. The control unit

supplies the meter with power and presents a dial which allows for adjustments in the wave height meter to perform the desired calibration.

A calibration phase was conducted to calculate the factors required to linearly link the recorded voltage to surface elevation values in meters. The factors were computed by gradually varying the water level inside the flume in regular steps, recording the measured voltage and dividing the applied increase in water level by the measured voltage. The average of the factors for each step was calculated and was used as the final factor for the conversion between measured voltage and surface elevation. Equation 3.1 was applied for the conversion, where  $\eta$  refers to the surface elevation in meters and to the measured value in volts. The factors resulting from the calibration are presented in Table 3.1.

$$\eta = factor * x \quad (3.1)$$

Table 3.1: Conversion factors for six wave gauges

| Wave Gauge | Conversion Factor [m/V] |
|------------|-------------------------|
| 1          | 0.0253                  |
| 2          | 0.0248                  |
| 3          | 0.0249                  |
| 4          | 0.0245                  |
| 5          | 0.0244                  |
| 6          | 0.00502                 |

The measuring locations for the six wave gauges were selected to maximise the coverage in horizontal direction and to capture the shoaling zone and the breaking zone for all wave conditions. A representation of the flume with the measuring locations is presented in Figure 3.3. The exact positioning of the instruments is provided in Table 3.2. The instruments deployment strategy is described in detail in Section B.2.

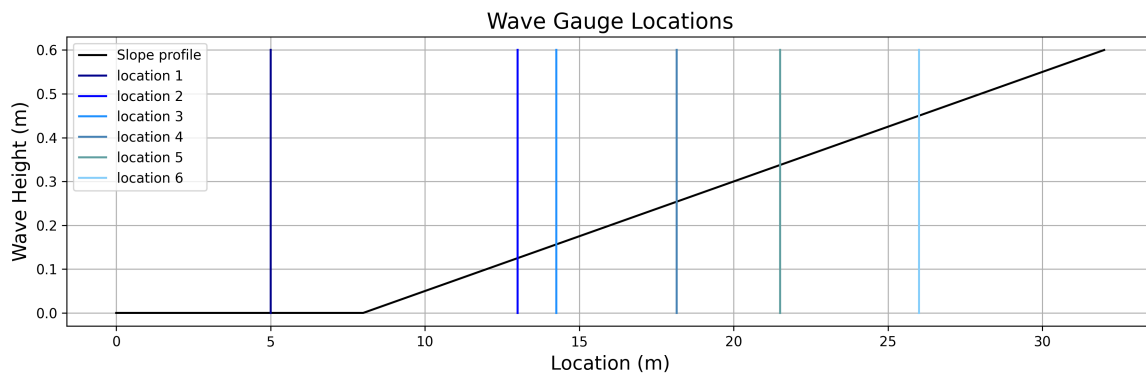


Figure 3.3: Representation of flume set up with measuring locations.

| Location   | x location [m] | Depth above bottom [m] |
|------------|----------------|------------------------|
| Location 1 | 5              | 0.235                  |
| Location 2 | 13             | 0.18                   |
| Location 3 | 14.25          | 0.15                   |
| Location 4 | 18.15          | 0.06                   |
| Location 5 | 21.5           | 0.06                   |
| Location 6 | 26             | 0.003                  |

Table 3.2: Placement depths of wave gauges (WG) at different  $x_f$  locations along the flume.

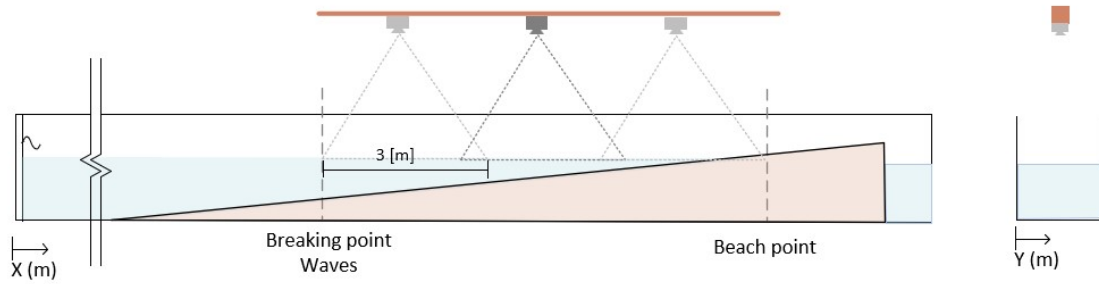
### 3.1.3. Camera set up

To analyse particle movement throughout the flume, six GoPro cameras were used, three of which were mounted overhead to capture the top view, and three were positioned along the side to record the side profile. Two GoPro cameras, model Hero7 and four GoPro cameras model Hero 10 were used, which were all set to record at 30 frames per second in Linear mode in 4k resolution. To allow the cameras to operate for an extended period of time, their batteries were removed and they were connected to power outlets using long USB-C cables. The GoPro cameras were connected to the GoPro Quik app, allowing remote operation using a phone. The video recordings were saved on SD cards and were transferred to hard drives at the end of each set of runs. The GoPro models Hero7 and Hero10 vary slightly in terms of camera consistency (field of view, colour profiles, distortion), which might result in slight differences in video footage. To ensure colour consistency for the colour-based tracking algorithm, three identical GoPro Hero10 cameras were used for the top view. This decision was made to avoid potential colour differences between the Hero7 and Hero10 models, as the top-view recordings were used for quantitative analysis of the particles trajectories and therefore required particular attention.

With regard to the top-view cameras, three GoPro cameras were used to capture footage from above. The overhead cameras were attached under a 12-metre-long wooden beam installed above the length of the flume. The cameras were secured to the underside of the beam, which had been tested to ensure it was level. The beam was positioned at a height of 2.15 metres above the bottom of the flume, centred along the width of the flume. This setup allowed the cameras to capture a 3-meter-long section of the flume in the x-direction while ensuring optimal particle visibility for tracking purposes. A schematic representation of the setup is provided in Figure 3.4.

The exact placement of the cameras along the flume (x-direction) was determined based on the beaching location and the breaking point of each wave condition. To ensure continuous particle tracking, the camera view windows were strategically positioned to have an overlap between the different videos. Given the different breaking behaviours relevant to the tested wave conditions, the camera setup was adapted to always capture the shoaling zone, breaking zone and beginning surf zone across all wave steepness conditions. The final camera set up is described in detail in Section B.4.

Top-view Camera Setup (not to scale)



Side-View Camera Setup (not to scale)

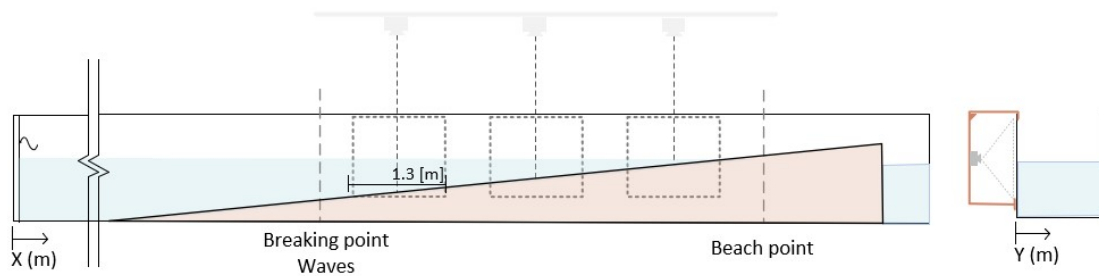


Figure 3.4: Schematic showing placement of the cameras in longitudinal direction and as a cross section along the length of the flume

The side-view cameras were positioned at the same cross-sections as the top-view cameras to ensure spatial correspondence between the two perspectives. These cameras were mounted on a wooden frame placed 0.9 metres away from the glass wall of the flume. Due to this relatively short distance, each camera's field of view covered approximately 1.3 metres in width. As a result, the side-view cameras captured only a portion of the total travel distance of the particles within the flume. However, the missing segments were not considered problematic as the recordings from the side-view cameras were not used for particle tracking. Instead, these videos served as a tool for qualitative analysis. Specifically, the side-view recordings were used for observational purposes to visually inspect the flow and particle behaviour, especially in cases where the top-view recordings indicated unusual or unexpected behaviour.

A camera calibration process was performed in order to avoid any image distortion; the specifics of this are described in Appendix A. No relevant distortion was observed, therefore, the original videos were used in the analysis. Additionally, pixel distances were related to metric distances by using reference frames indicating real-world distances visible on camera. Further elaboration on the reference frames system can be found in Appendix A.

## 3.2. Experimental Conditions

### 3.2.1. Wave Conditions

The wave conditions tested in this study were designed to cover a range of wave offshore steepness values with the goal of investigating the influence of this parameter on the beaching behaviour of plastic debris. This was done by conducting a series of experiments in the wave flume covering seven wave conditions W1 - W7. Steepness in this context was determined at the flume's initial section prior to the slope's start, representing the "offshore steepness" of the waves. This parameter

was modified by maintaining a constant period along all the runs and varying the programmed wave height.

The initial parameters to be defined for the wave generation include the period of the waves, the wave height and the mean still water level in the generation tank. In the context of this research the still water level was set to 0.5 metres. This value was selected as optimal, as high enough to allow for adequate wave generation and at the same time low enough for all the generated waves to propagate within the slope. The period of the generated waves was set to 1.5 seconds and the wave height was varied across the different tested wave conditions.

Waves were further characterised by computing their wavelength, offshore steepness and the relative Ursell and Iribarren numbers. The wavelength was assessed using the dispersion relationship shown in equation 2.1 in Section 2.2. This is an implicit expression which requires an iterative procedure to calculate the wavelength for a given period and depth. Explicit expressions that approximate the solution are available and widely used; in this context, the Fenton approximation was applied (Fenton 1988). The method consists of solving equation 2.1. This was done stepwise as described in Section 2.2. The computation resulted in an offshore wavelength of 2.86 metres.

The offshore steepness was computed according to the definition presented in Section 2.2, Equation 2.8. In the context of this research, it was varied by maintaining the input period fixed at 1.5 seconds and varying the offshore wave height across the different experimental runs from 0.05 m to 0.23 m which allowed for the generation of waves with offshore steepness varying from  $\epsilon = 0.056$  to  $\epsilon = 0.256$ .

According to the method used to vary the input forcing, referring to a wave condition by its height or by its steepness is effectively equivalent. For simplicity, the term *wave height step* or *steepness step* may be used interchangeably to indicate a change in initial wave conditions. In the following sections, the different wave conditions will be referred to as W1 - W7, details on the specifics for each condition are provided in Table 3.3.

Starting from the assessed wave basic parameters, period, wave height, wavelength and steepness, further considerations on the wave generation were made. The Ursell number was evaluated; this criterion combines the wave steepness and relative water depth and is widely used to quantify the degree of nonlinearity of waves (Holthuijsen 2007). This was done according to equation 2.9 presented in Section 2.2.

According to the Ursell criterion, a maximum wave height of 0.39 m could be generated within the wave flume without wave breaking occurring right out of the paddle. This was not observed in the laboratory, where waves started to break right out of the paddle around a wave height of 0.27 m with a period of 1.5 seconds. The definition of the criterion, in fact, ignores the emergence of breaking when waves grow too steep in deep or shallow water (Holthuijsen 2007). The Ursell number was assessed for wave conditions W1 - W7 and is presented in Table 3.3.

In order to ensure proper wave generation within the flume, the input wave conditions had to comply with the domain of linear wave theory or second-order Stokes. This was assessed by computing the relative steepness and relative water depth (respectively 2.10, 2.11) and comparing them with the ranges of applicability of the various wave theories. Figure 3.5 shows the validity domains with an indication of the region where the tested wave conditions fall within, this was considered acceptable for experimental purposes.



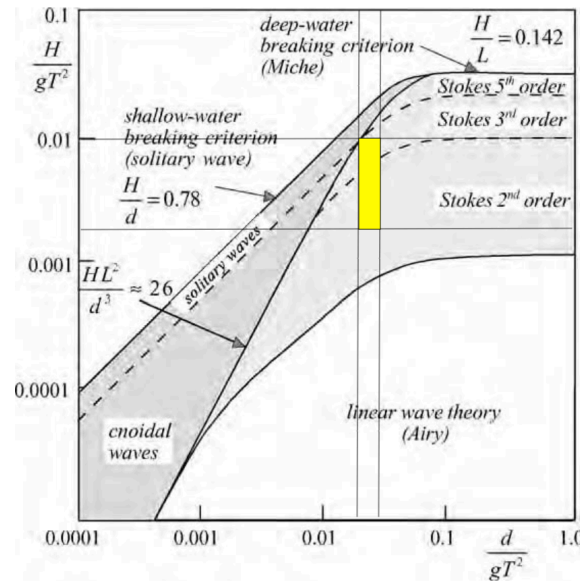


Figure 3.5: Ranges of applicability of the various wave theories (Holthuijsen 2007) with yellow region representing the input wave conditions.

Wave breaking represents the most non-linear process affecting waves in coastal waters (Holthuijsen 2007), and is therefore hypothesised to play an important role in the transport dynamics of MPD. In order to understand the type of breaking the generated waves would undergo under the programmed initial conditions, the Iribarren number was calculated according to equation 2.12. The computed wave properties for the generated conditions W1 - W7 yielded Iribarren numbers consistent with spilling wave breaking. Indicating a more gradual type of wave breaking as opposed to the abrupt nature of plunging or collapsing breakers.

Experiments were conducted for a total of seven wave conditions, summarised in Table 3.3. They comply with the aforementioned criteria and with the limitations of the wave generator. The values of wave height and wave period presented were used as input parameters to the wave maker. This allowed for the generation of wave conditions W1 - W7 with a resulting offshore steepness range ( $\epsilon = ak = 0.056 - 0.256$ ) which was considered representative of low, medium and high steepness scenarios. The Ursell number and Iribarren number are presented, as well as the expected breaking type according to the Iribarren number.

Table 3.3: Wave conditions with corresponding offshore steepness, Ursell number, Iribarren number and breaking type.

| Condition | Wave Height [m] | Wave Period [s] | Steepness [-] | Ursell [-] | Iribarren [-] | Breaking |
|-----------|-----------------|-----------------|---------------|------------|---------------|----------|
| W1        | 0.05            | 1.5             | 0.0556        | 3.19       | 0.188         | Spilling |
| W2        | 0.08            | 1.5             | 0.0889        | 5.11       | 0.149         | Spilling |
| W3        | 0.11            | 1.5             | 0.122         | 7.03       | 0.127         | Spilling |
| W4        | 0.14            | 1.5             | 0.156         | 8.95       | 0.112         | Spilling |
| W5        | 0.17            | 1.5             | 0.189         | 10.9       | 0.102         | Spilling |
| W6        | 0.20            | 1.5             | 0.222         | 12.8       | 0.0940        | Spilling |
| W7        | 0.23            | 1.5             | 0.256         | 14.7       | 0.0877        | Spilling |

### 3.2.2. Identification of Hydrodynamic Zones within the Flume

Waves approaching the coastline experience transformations due to decreasing water depth and interaction with the sloped bottom. The specific wave propagation phases can be associated to distinct zones as outlined in Section 2.3.

Throughout this research, particles were released in the shoaling zone, consistently one meter before the wave breaking point. The breaking point marks the transition between the shoaling zone and the

surf zone. Although this transition is referred to as the 'breaking zone' in the context of this study, its exact boundaries are difficult to define.

The limits identifying the different zones were defined starting from visual observation of wave behaviour within the flume. Additionally, sinking particles were released to further understand the flow dynamics. It was observed that sunken particles tended to consistently accumulate right below the point where waves reached their steepest state, starting to collapse on themselves; this location was referred to as the breaking point. By closely observing the waves, it was determined that waves started to break approximately 50 cm before this accumulation point to then ultimately collapse approximately 50 cm later.

Prior to the breaking zone, waves progressively steepened as they entered shallow water domains, increasing in height and decreasing in wavelength. This domain between the particles release point and the beginning of the breaking zone was defined as the shoaling zone.

Following the end of the breaking zone, wave height suddenly decreased, propagating in progressively shallower water depths. This zone, characterised by further energy dissipation and bore-driven flow, extends until far up the slope and is referred to as the surf zone.

Finally, the swash zone was defined from the onshore end of the surf zone and extended up the wooden slope ending at the maximum run-up limit of incoming waves.

Given the characteristics of the different zones, the breaking zone is hypothesised to play an important role in particle horizontal transport as it corresponds to the sudden release of the energy built up during the shoaling phase. Particular attention is therefore given to this domain in the analysis.

The definition of the different zones followed the same methodology for each tested wave condition, starting from the identification of the breaking point. The deployment of sinking particles allowed for a clear and systematic determination of the said breaking point across the different wave conditions.

### 3.2.3. Breaking Zone Locations

The generation of wave conditions characterised by increasing offshore wave steepness resulted in the variation of the location of the breaking zone within the flume. The generated waves started breaking as they approached the depth-induced breaking limit. Specifically, the steeper the wave, the earlier the breaking occurred in the flume as the critical wave height-water depth ratio was reached earlier for waves characterised by higher steepness values and thus higher initial wave heights. This caused the breaking point to shift from a more onshore location for the less steep wave conditions to a more offshore location for the steepest generated waves. A summary of the breaking locations is presented in Table 3.4 and shown in Figure 3.6.

Table 3.4: Locations of breaking points along the flume.

| Breaking Point | Distance from Flume Start [m] |
|----------------|-------------------------------|
| W1             | 24.10                         |
| W2             | 22.35                         |
| W3             | 20.95                         |
| W4             | 19.06                         |
| W5             | 17.40                         |
| W6             | 15.40                         |
| W7             | 13.58                         |

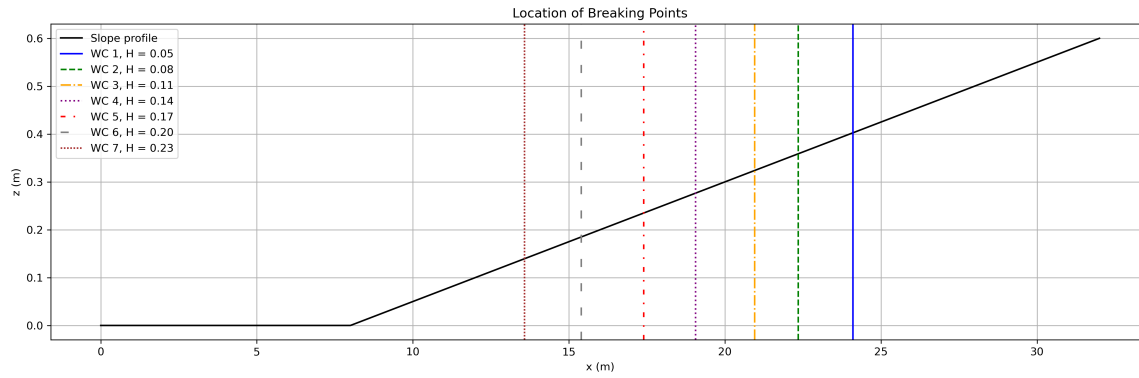


Figure 3.6: Location of breaking points across different wave conditions.

### 3.2.4. Plastic Debris

Marine Plastic Debris (MPD) was simulated in the experiments by the deployment of idealised objects of spherical shape with a diameter of 4 cm and a mass of 25 g. The corresponding non-dimensional properties of the objects were defined as relative density, density of the object over the density of water ( $\rho_{MPD}/\rho_w$ ), and relative size, ratio of the sphere diameter (characteristic length  $l$ ) to the incident wavelength  $\lambda$ . The objects used in this research are characterised by a relative density of 0.75 and a relative size of 0.014 - 0.05, varying throughout the evolution of the waves propagating on the slope. The plastic particles were coated with neon yellow, green and pink paint. This was done to increase their visibility and the performance in simultaneously tracking multiple particles during the processing phase.

## 3.3. Experimental Procedure

The experimental procedure was designed to observe and measure the beaching behaviour of MPD under varying wave conditions.

A series of steps was systematically carried out during a preparatory phase before the start of the actual experiments. The flume was filled up until a stable water level of 0.5 m. This water level was visually inspected using a measuring lint on the side of the flume and detected consistently by the wave generator. The measuring instruments installed at Location 1 were turned on from a designated computer, starting the recording of the surface elevation and velocity values, which were continuously logged for the whole duration of the experimental runs.

Once the target water level was reached and the measuring instruments were on, the wave generator was activated. This was programmed to replicate the desired wave conditions for a total time of 45 minutes. This time frame was selected to keep the generated waves as stable as possible, avoiding them from diverging from the programmed conditions in the long term. In addition, the ARC system was turned on and left on for the whole duration of the experimental runs to absorb waves reflected by the structure, avoiding potential disturbances in the observed wave conditions.

The generator was left on for an initial spin-up time of five minutes before starting the measurements. The definition of the spin-up time is justified in Section B.1. During this time, no experiment was conducted to limit the influence of any initial disturbances on early measurements.

The last step of the preliminary phase consisted of remotely turning on all the installed GoPros. The six GoPros were activated at slightly different times as they had to be turned on one by one. To synchronise the recordings and establish a common reference point across all cameras ( $t = 0$  [s]), a sharp sound was generated at the start of the experiment. This sound, which could be heard across all six recordings, was used to temporally align the datasets.

The actual experimental procedure consisted of carefully placing the plastic particles at their designated starting positions inside the flume. The particle release location was defined based on observations on the transport dynamics specific to the flume set-up; further elaboration on this can be found in Section B.3. The particles were always placed from above, in the middle of the flume in y-direction and approximately one metre before the waves breaking point. The travel time of the particles from the moment they entered the flume until they reached a stable position on the beach was manually measured by recording the time of placement and the time of beaching. Once beached, the particles were retrieved from the flume and placed again with a cadence that allowed for the maximisation of the number of particles travelling in one experimental run.

Due to limitations in video storage capacity, particles were continuously released into the flume over a period of 10 minutes. After this duration, the cameras were stopped, the footage was saved, and the cameras were turned on again for the next run. After the completion of three runs the wave generator was switched off in order to stay within the programmed 45 minutes. The flume was then let to rest until a stable water level was reached again and the procedure could be performed again.

On average, a total of 15 particles were released in each run. The presented procedure was repeated until the desired number of particles fully travelled through the portion of the flume spanning from before the breaking location until the beaching point. Due to limited time availability at the wave flume facility, the desired number of trajectories to obtain within this campaign was set around 60-80 particles for every wave steepness step.

After completing the runs for a given wave steepness condition, the positions of two top-view and side-view cameras were adjusted to capture the breaking zone and the adjacent surf zone for the next wave conditions. The remaining two cameras, focused on the swash zone, remained fixed throughout all seven wave conditions.

### 3.4. Hydrodynamic Conditions

To verify that the generated wave conditions in the flume matched the intended settings and remained consistent throughout the experimental runs, the wave gauge data at Location 1 were analysed. The location of this wave gauge was selected as, at this point, the waves had not yet interacted with the slope. From this data, the initial spin-up time and the end of the time series, where the paddle was turned off and the water began to calm down, were excluded. This was done to ensure the accuracy of the generated wave heights, as particle transport was analysed based on the programmed wave characteristics. It was therefore important that the actual wave heights matched the intended wave height settings.

Additionally, verifying the stationarity of the wave conditions was crucial, as non-stationary wave behaviour could lead to time-dependent variations in the particle trajectory dataset, as the particles were released one by one over time. The verification was done using two different approaches, both described below.

First of all, an analysis of the water surface elevation data was conducted using the zero-crossing method. This method identifies individual waves by locating the points where the water level crosses the mean (zero) line. The wave heights were calculated as the difference between the local crest and trough elevations for each detected wave. The data was then divided into consecutive 15-second blocks (10 waves per block). The average wave height across the blocks was compared to the programmed wave height in order to assess whether the measured wave height remained stable over the entire measurement time.

Secondly, a statistical test was conducted as an additional verification of the stationarity of the surface elevation measurements over time. The Augmented Dickey-Fuller (ADF) test was applied to the wave height series extracted using the zero-crossing method (Plus 2023). The null hypothesis of this test states that the time series has a unit root, implying non-stationarity, while the alternative hypothesis indicates stationarity.

### 3.5. SWASH Model

In order to support the experimental work conducted in the wave flume, a numerical model was developed using SWASH. The following section aims to justify and explain how this was performed.

SWASH (Simulating WAVes till SHore) is a wave-flow model designed to simulate unsteady, non-hydrostatic, free-surface, rotational flow and transport phenomena in coastal waters. Forcing such as waves, tides, buoyancy, and wind can be simulated. It provides a general basis for describing wave transformations from deep to shallow water or even more complex scenarios such as harbours or ports. SWASH is capable of resolving short-wave dynamics such as wave breaking, swash, and overtopping, making it suitable for simulations in wave flumes. In flume research, SWASH can be used to replicate experimental conditions and validate physical measurements. This allows for testing various scenarios digitally before or alongside laboratory experiments in the actual flume.

Within this research, SWASH was used alongside the experiments in the actual flume to simulate the wave conditions generated in the laboratory. The final goal of this analysis was to transition from discretised information about the wave dynamics limited to the locations in the flume where measuring instruments were installed, to a continuous set of data along the horizontal direction of the flume. The results obtained from the SWASH model were compared to the measured wave characteristics to ensure its reliability in representing the experimental conditions. This was achieved by comparing the surface elevation data collected by the six wave gauges installed along the flume (described in Section 3.1.2) to the results of the SWASH model in the exact same measuring locations. Good agreement between simulated and measured wave conditions at all six locations would indicate that the SWASH model reliably captures wave behaviour throughout the entire length of the flume. A more detailed description of the SWASH model design can be found in Appendix D.

The comparative analysis was based on four key hydrodynamic parameters, wave height ( $H_s$ ), wave period ( $T_s$ ), wave asymmetry ( $\mu$ ) and wave skewness ( $\lambda$ ). These were computed starting from the surface elevation time series measured at the real and virtual wave gauges. First, the numerical model and the experimental data were compared using the variance density spectrum. This can show how the wave energy is dispersed throughout the various frequencies, making it a useful first indication of agreement between the model's outcome and the measured data. Beyond the spectral comparison, the above-mentioned wave parameters were used to assess the compliance between the modelled and measured conditions. In order to assess the agreement in shape of the simulated waves, the horizontal asymmetry ( $\mu$ , asymmetry) and vertical asymmetry ( $\lambda$ , skewness) of the waves were computed and compared. These were computed respectively as 3.2 and 3.3 according to Myrhaug et al. (1986).

$$\mu = \frac{\eta'}{H} \quad (3.2)$$

Where:

- $\eta'$  is the crest elevation above the mean water level [m],
- $H$  is the wave height, i.e., the vertical distance from trough to crest [m].

$$\lambda = \frac{T''}{T'} \quad (3.3)$$

Where:

- $T'$  is the time from the preceding zero-crossing to the crest [s],
- $T''$  is the time from the crest to the next zero-crossing [s].

The values of these parameters computed using the complete available surface elevation time series from the modelled and real wave gauges were compared by assessing the relative difference

between them. If the difference of the values was considered small enough for all the computed parameters across the different wave gauges, the model could be considered representative of the experimental conditions inside the flume. Having a representative model would result in a continuous data grid of the wave conditions at each longitudinal location over time. This would help with determining the edges of the different wave zones (shoaling, breaking, surf and swash) and would allow local wave steepness calculations throughout these zones, which is of importance for further analysis.

### 3.6. Particles Drift

This section outlines the methodology used to extract MPD trajectories and assess their drift within the flume. This process entails a first step of transition from raw video footage to complete sets of x and y coordinates of particles position over time using the software YOLO and validated with Tracker. The horizontal drift velocity of the MPD was then computed and compared with other theoretical speed values.

#### 3.6.1. Preliminary Particle Drift Analysis

Initially, a preliminary analysis was conducted regarding the drift speed of each of the different categories to determine the best approach for further analysis. The results of this preliminary analysis are discussed in Appendix C. This analysis yielded significant differences between particles undergoing the seven wave conditions, both in terms of total distance travelled and in the way particles from different categories behave across different hydrodynamic zones.

#### 3.6.2. Particles Detection: Yolo

In this research, YOLO was used to track the particles captured in the video recordings. YOLO (You Only Look Once) is a real-time object detection algorithm that identifies and localises objects within images or video frames (Jocher 2020). To tailor YOLO for this specific application, a training dataset is required. Roboflow was used to upload and label images, split datasets, and export them in the correct format for YOLO training. This process involved extracting frames from video footage and manually labelling the location and colour of each particle.

Once the dataset was prepared, the YOLO model was trained using Python, enabling it to recognize and track particles in new video frames. A Python script then processed each video, applying the YOLO algorithm to detect particles and record their (x, y) position for every frame. These coordinates were stored as text files in a specified output directory.

To ensure accurate and efficient detection, the videos were pre-processed before being fed into YOLO. The following steps were taken:

1. The three overhead camera segments were synchronised using a beep sound audible in all recordings. As the cameras were started sequentially, this beep allowed the videos to be trimmed and aligned at a common  $t = 0$  [s].
2. Videos were rotated and cropped to include only the flume, with the origin of the reference frame in the bottom-left corner, and the other ends of the reference frames forming the top-left and bottom right corners.
3. Compression was applied after confirming that YOLO maintained performance at lower quality, improving processing speed and storage efficiency.

These preprocessing steps ensured that the videos were ready for accurate particle tracking using the trained YOLO model.



### 3.6.3. Tracking Algorithm

This section presents the overall workflow of the tracking algorithm, including the YOLO detection data and all the steps involved in extracting, processing, and analysing particle trajectories. This is initiated from YOLO detection outputs and provides as an output a structured dictionary of particle trajectories for further analysis.

The complete tracking algorithm was developed in Python and was organised in five main components: parameter configuration, detection and tracking, detection processing, trajectory merging and final data organisation. Each part is stored in dedicated scripts made available in a GitHub repository along with a thorough documentation of every function used. A direct link to the repository can be found in Appendix G.

The first step consists of the configuration of all relevant settings and parameters. These are video-specific information and a set of thresholds defined to guide the processing and merging of the trajectories. More on the definition of these thresholds can be found directly in the code documentation.

With all the settings and processing thresholds established, the next phase consists of the actual tracking. Particle detection is done by feeding the preprocessed videos to a YOLO-based model. In this step, single particles in the videos are tracked over time. This results in raw label data consisting of x and y coordinates for every detected particle for every frame of the video. The label data is read and processed to organise the obtained detections into single trajectory pieces. This is done by splitting the data into segments based on the proximity of the detections in both space and time, using defined thresholds for maximum frame and positional gaps. Any potential errors in the tracking process are filtered out by only considering segments with a sufficient number of tracked locations.

Given that each experimental run was recorded from multiple top-view cameras, a merging process was included to be able to reconstruct complete particle trajectories. The obtained partial trajectories of the same particle across different viewpoints were aligned and combined. This was handled by comparing the position, timing and colour of the particles, ensuring accurate merging into continuous paths.

The processed and merged trajectories were finally compiled into a dictionary which includes the whole set of particle trajectories in real-world coordinates, together with the related metadata for each experimental run. Trajectories corresponding to specific runs or experimental conditions can be accessed based on the wave height and the run identification number. This allows for further analysis and comparison across the different wave conditions and experimental runs.

### 3.6.4. Trajectory Validation with Tracker

Tracker is a free, open-source video analysis tool developed by Open Source Physics that allows users to track and analyse object motion in videos. In this research, Tracker was used to generate reference trajectories by combining its auto-tracking feature with manual corrections when the particle was lost by auto-tracking. Real-world distances were determined using the same reference frame setup as in the YOLO-based tracking. By closely supervising the tracking process, it was ensured that the resulting trajectories were reliable, which were then used to validate the automated YOLO tracking. In addition, Tracker was used to track the wave crests to obtain crest speed values.

### 3.6.5. Trajectory Processing

The trajectory data along the flume showed oscillations caused by particle-wave interactions. However, this research focuses primarily on the net drift of the particle, rather than its instantaneous back-and-forth motion.

In order to be able to estimate the net velocity along the full trajectories, the existing gaps in data resulting from the tracking process were filled. This was done by applying a 1D linear interpolation of the x-position data as a function of time. The level of completeness of the trajectory data was satisfactory to yield good results after interpolation. The interpolated data showed perfect agreement

with the initial trajectories and allowed to obtain continuous data along the horizontal direction.

In order to capture the actual net horizontal velocity, a Butterworth low-pass filter was applied to the interpolated trajectories to remove high frequencies from the particles motion. This resulted in a smoothed signal, which allowed for the estimation of the net drift of the particles.

The filtered trajectories were segmented based on a step distance of 0.2 metres. For each segment, the particles horizontal drift speed was estimated by dividing the horizontal displacement by the relevant time interval. The horizontal drift speed values of all trajectories were grouped per bin, and the mean and uncertainty were calculated to obtain average drift speeds for each offshore steepness condition for every 0.2 metres along the length of the flume.

### 3.7. Computation of Wave Propagation Speeds

The wave motion observed in the experiments was characterised by computing key wave propagation parameters: the wave phase speed, the wave crest speed and the Stokes drift. These provide insights on the different wave velocity components and were compared to the particles drift to assess their relation to the MPD transport. The following sections describe the computational approaches used for every parameter.

#### 3.7.1. Phase Speed

As mentioned in 2.4.1, phase velocity describes the speed at which the wave is propagating, which depends on wavelength and period. In this research, the phase speed was determined assuming linear waves, using formula 2.13 and determined with the additional corrections for non-linearity using formula 2.14. Both formulas require wave height (either directly or via the wave number  $k$  and wavelength  $L$ ) and water depth as inputs. Since both the mean wave height and the water depth change along the length of the flume due to the presence of the slope, local phase speed values for 0.1 metres segments along the length of the flume were determined. Within each 0.1 metres segment, the mean still water depth and mean wave height-determined by SWASH-were estimated as constant over the narrow segment.

#### 3.7.2. Crest Speed

Crest speed is the velocity at which the highest point of a wave travels through the water. As mentioned in section 2.4.1, it should be the same or similar to the phase speed. Within this research the crest speed was determined using the SWASH model and the zero-crossing method. For each 0.2-metre segment along the flume, the time at which a specific wave crest passed was recorded at two consecutive points. By calculating the time difference between these two points and dividing the known distance of 0.2 metres by this time difference, the local crest speed was determined for each segment. Repeating this process for approximately 700 waves provided robust estimates of the crest speed.

Additionally, a second method to estimate the crest speed was applied (on one of the used wave conditions) using the top-view video recordings and Tracker. In this approach, the crest of each wave was manually tracked over the first 5.5 meters after the particle release location by marking its position frame by frame for approximately 15 waves. The speed values determined were averaged again over 0.2 metre segments, to allow direct comparison with the crest speed values determined using Swash.

#### 3.7.3. Stokes Drift

In this specific application, the Stokes drift was locally determined along the longitudinal direction of the flume. The presence of a sloped bottom made the estimation of local drift values necessary as the water level, and consequently local steepness, was variable along the flume. Values for Stokes drift were therefore computed every 0.2 metres along the whole length of the flume. This was made



possible by the results of the SWASH model, which provided surface elevation time series for every x-location.

A 0.2 metre discretisation was selected to ensure precise representation of the Stokes drift variability across the slope. The computation was then repeated using increasingly bigger discretisation steps. The variability was assessed by comparing the standard deviation of the drift within each step. The analysis confirmed that a coarser resolution of 0.5 metres still captured the variability with sufficient accuracy.

---

**Legend:**  100% overlap  90% overlap with minimal adjustments  0% overlap

---



# Results

This chapter provides a complete overview of the results of the laboratory experiments conducted to investigate the influence of wave steepness on the horizontal transport and beaching behaviour of marine plastic debris. The findings are divided into three main themes: the hydrodynamic conditions and wave field characterisation, the observed particle trajectory and transport dynamics in relation to the research variable, and the comparison of particle drift with characteristic wave propagation speed estimates. The findings are supported by visualisations and summaries which are described in the following sections, detailed interpretation will be provided in the discussion, Chapter 5.

## 4.1. Overview of Experimental Runs

Seven different wave conditions were generated in the experimental campaign. The programmed wave height was varied across the experimental runs, resulting in seven different offshore wave steepness conditions. In the following sections the experimental conditions will be referred to as W1 - W7, details on the relevant wave properties can be found in Table 4.1.

Table 4.1: Wave conditions with corresponding wave height and offshore steepness ( $\epsilon = ak$ ).

| Condition | Wave Height [m] | Steepness ( $\epsilon$ ) |
|-----------|-----------------|--------------------------|
| W1        | 0.05            | 0.0556                   |
| W2        | 0.08            | 0.0889                   |
| W3        | 0.11            | 0.122                    |
| W4        | 0.14            | 0.156                    |
| W5        | 0.17            | 0.189                    |
| W6        | 0.20            | 0.222                    |
| W7        | 0.23            | 0.256                    |

A total of 37 experimental runs were conducted. This yielded a variable number of final particle trajectories per wave condition, summarised in Table 4.2.

The variability behind the number of trajectories between the tested conditions can be attributed to different sources. The particle tracking process performed by YOLO showed high variability in the performance across single trajectories, leading to some particles not being consistently recognised and producing unusable trajectory data. While the model showed good accuracy in the detection of individual particles (92–93%), it presented limitations in clearly distinguishing particles from the background. This caused misdetection issues and contributed to the variable number of complete trajectories being recognised. A more detailed overview of the model performance can be found in Appendix E. In addition, the merging process of the different trajectory pieces based on temporal and spatial alignment between videos described in Section 3.6.3 was highly susceptible to human

error. This caused some of the actual trajectories to be excluded from the analysis because not correctly aligned.

Table 4.2: Total number of trajectories obtained per wave condition

| Wave Condition | Number of Trajectories |
|----------------|------------------------|
| W1             | 51                     |
| W2             | 40                     |
| W3             | 32                     |
| W4             | 53                     |
| W5             | 40                     |
| W6             | 56                     |
| W7             | 31                     |

It is important to mention the variability of spatial coverage relevant to each wave condition. As described in Section 3.2.3, the location of the breaking zone varied across the different wave conditions. It was decided to consistently capture the shoaling zone, the breaking zone and the beginning of the surf zone for all the experimental runs. This allowed for the complete coverage of the particle trajectory for W1 and W2. However, for conditions W3 - W7, where the breaking point was located progressively more onshore, the trajectories were only partially caught on camera. To allow for fair comparison between the different conditions, all trajectories were aligned to start from the release point and extend as far as their motion was visible within the camera frame.

## 4.2. Hydrodynamic Conditions and Wave Characterisation

An analysis of the generated wave field within the flume was conducted in order to confirm good agreement between the wave conditions programmed at the wave generator and the actual wave conditions observed in the flume. Additionally, in order to be able to get continuous information on the wave characteristics across the entirety of the flume, a SWASH model was built and validated against the surface elevation data available from the wave gauges. The results of this analysis are presented in the following sections.

### 4.2.1. Comparison of Target and Generated Wave Conditions

The time series of the wave elevation data measured by the wave gauge installed at Location 1 (the most offshore location) was analysed for W1 - W7. This resulted in a statistical summary of the individual wave heights computed using a zero-crossing method considering 10 minutes of continuous measurements with a sampling frequency of 20 Hz, accounting for 360 passing waves. The results of the analysis of the wave elevation data yielded average wave height values which are presented in Table 4.3 for every wave condition.

Table 4.3: Statistical summary of individual wave heights at Location 1 for wave conditions W1-W7.

| Wave Condition | Programmed H [m] | Mean [m] | Std [m] | Min [m] | Max [m] |
|----------------|------------------|----------|---------|---------|---------|
| W1             | 0.05             | 0.048    | 0.0004  | 0.047   | 0.049   |
| W2             | 0.08             | 0.078    | 0.0005  | 0.077   | 0.079   |
| W3             | 0.11             | 0.109    | 0.0005  | 0.107   | 0.110   |
| W4             | 0.14             | 0.138    | 0.0007  | 0.136   | 0.139   |
| W5             | 0.17             | 0.170    | 0.0011  | 0.168   | 0.174   |
| W6             | 0.20             | 0.202    | 0.0016  | 0.198   | 0.207   |
| W7             | 0.23             | 0.234    | 0.0024  | 0.228   | 0.240   |

The mean and standard deviation of wave height, minimum and maximum wave height measured were used as quantitative metrics for the analysis. By comparing these statistics with the pro-

grammed values of wave height across the different wave conditions, it can be concluded that the wave maker is able to reproduce the desired wave characteristics with good accuracy and precision. The mean wave height values are close to the programmed ones at the millimetre scale and show standard deviation values of at least two orders of magnitude lower than the mean value. The standard deviation of the mean wave height shows an increase with the increasing programmed wave height, suggesting that more energetic wave conditions led to slightly more variability in individual wave heights. This variability is still considered acceptable for all the wave conditions. Minimum and maximum values of the generated waves do not show relevant anomalies, ensuring that the required wave height is correctly produced across the complete time series.

The Augmented Dickey-Fuller (ADF) test was conducted to ensure stationarity of the time series. The test yielded p-values approximately around 0.005 for all the tested wave conditions, well below the 0.05 threshold set within this research. This allowed the null hypothesis of non-stationarity to be rejected, confirming that the wave height time series was statistically stationary.

A power spectral density analysis was conducted on the surface elevation data from Location 1 across the different wave conditions to ensure that the generated waves consistently matched the intended wave period  $T = 1.5$  s. The results of the analysis are presented in Figure 4.1.

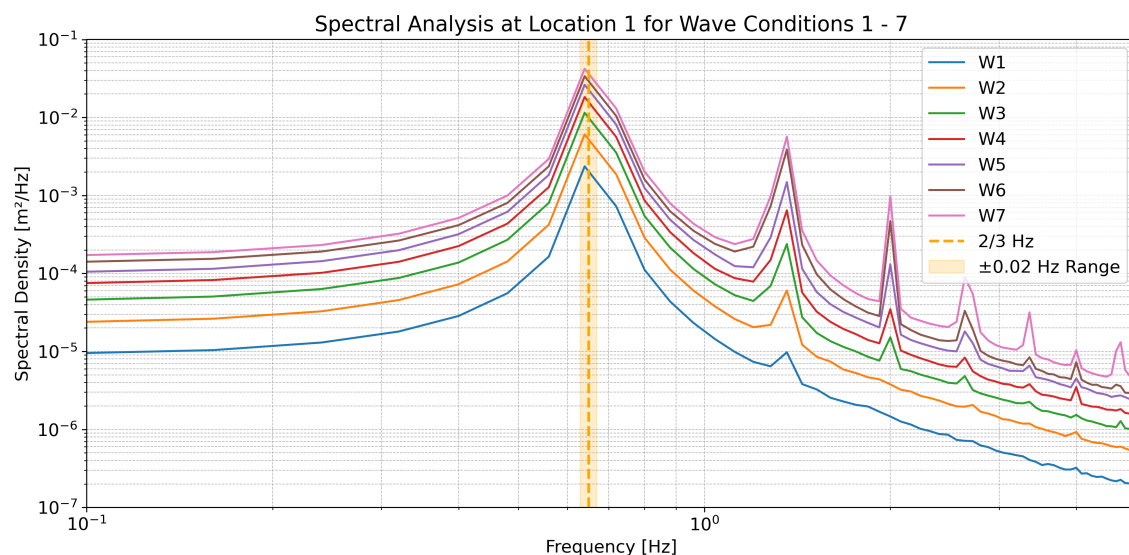


Figure 4.1: Wave spectra for all wave conditions (W1 - W7) along with a shaded acceptable region of  $\pm 0.02$  Hz around the target frequency.

All wave spectra present a clear peak around 0.67 Hz which is the target frequency corresponding to a 1.5 s wave period. A  $\pm 0.02$  Hz area around the target frequency represents the variability allowance, all spectral peaks fall within this area. It is therefore concluded that the desired wave period is met across all wave conditions. Minor peaks are visible at superior harmonics of the main frequency, these are hypothesised to result from wave reflection. Their intensity increases for the more energetic waves but remains consistently two orders of magnitude lower than the main peak.

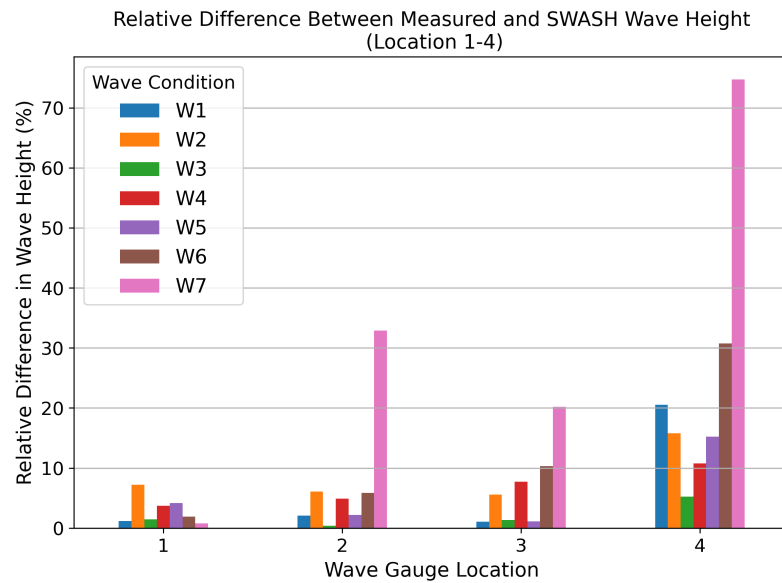
#### 4.2.2. SWASH Model Output Validation

The complete set of measurement instruments positioned at Locations 1 - 6 along the flume was used to assess the evolution of the wave properties on the sloped bathymetry of the flume. This limited the available information to six discrete locations. A SWASH model was therefore built and, in order to safely use it for further computation, it was validated against the actual data measured by the wave gauges.

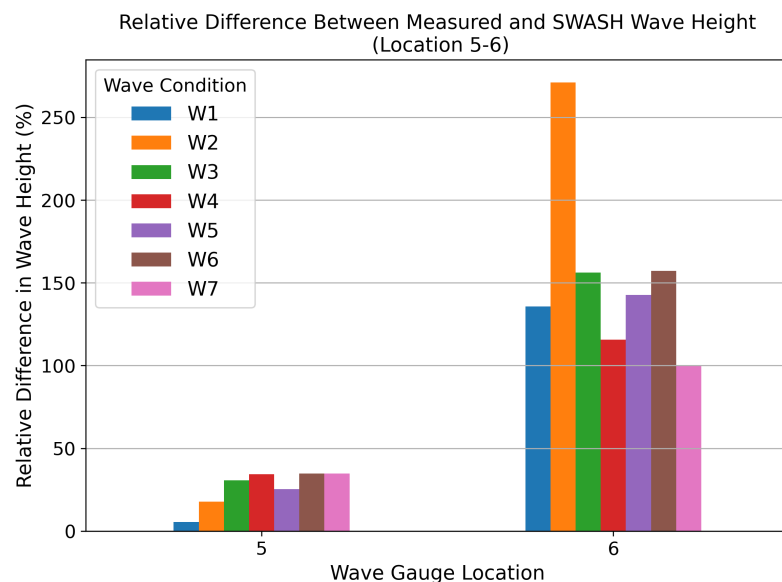
The simulated and measured wave heights were compared at the six locations. Figure 4.2a shows

the relative difference in wave height between the measured values obtained from the wave gauges and the simulated output obtained from the SWASH model for Locations 1 -4. Locations 1 to 4 show good agreement (relative difference between measured and simulated wave height generally below 5%) between the measured and simulated data for wave conditions W1 - W4 for which they were located at least one meter before the breaking point. For wave conditions W5 - W7 an increasing difference between the measured and simulated values is already noticeable from Location 3 on (relative difference between measured and simulated wave height increased to 15% - 70%). Figure 4.2b shows the relative difference in wave height at Locations 5 -6. The simulated values at Locations 5 and 6 perform worse in representing the measured wave height values for all the tested wave conditions. It has to be noticed that the water level at those locations was very low; this might have hindered the ability of the wave gauges to measure reliable surface elevation data. A detailed overview of the measured and simulated wave height values can be found in Appendix F.

The results of the analysis of the wave height values show good agreement between the measured and the simulated surface elevation data until the breaking zone, specific to each wave condition. From these observations it is possible to conclude that the SWASH model successfully simulates the wave dynamics until the breaking, after which it starts to overestimate the wave height until it is unable to represent the actual conditions in the swash zone. Overall, the performance of the model is considered satisfactory and very reliable until the breaking zone.



(a) Locations 1–4



(b) Locations 5 and 6

Figure 4.2: Relative difference in wave height between measured and SWASH outputs across wave conditions W1–W7. (a) Locations 1–4; (b) Locations 5 and 6.

A power spectral analysis was conducted on the surface elevation time series obtained from the SWASH simulation. This was done in order to ensure that the simulated waves consistently matched the intended wave period  $T = 1.5$  s. This analysis confirmed the presence of distinct spectral peaks corresponding to the target wave frequency (approximately 0.67 Hz) across all measurement locations and wave conditions. The complete results of the power spectral density for wave conditions W1 - W7 computed at Locations 1-6 can be found in Appendix F.

Finally, to complement the validation of the SWASH results, the shape parameters  $\mu$  (asymmetry) and  $\lambda$  (skewness) were computed from both the measured and simulated time series. Relative differences in asymmetry were generally low for Locations 1-5, with values below 10%, with most values

ranging between 1% and 6%. While the relative difference in asymmetry at Location 6 exceeded 20% for all wave conditions.

Regarding the skewness parameter, the relative differences were more pronounced, especially for the more energetic wave conditions. While most comparisons at Locations 1 - 4 showed differences below 15%, Locations 5 and 6 systematically showed stronger differences (up to 60% for wave conditions W5 and W6).

### 4.2.3. Delineation of Zones

Starting from visual observations in the laboratory, the breaking zone for every wave condition was identified and located in the simulated wave height profile for wave conditions W1 - W7. The SWASH wave height horizontal profile is displayed in Figure 4.3 together with a vertical shaded area representing the breaking point. The spatial domain displayed in the figure represents the flume from the toe of the slope, located at  $x = 8$  m.

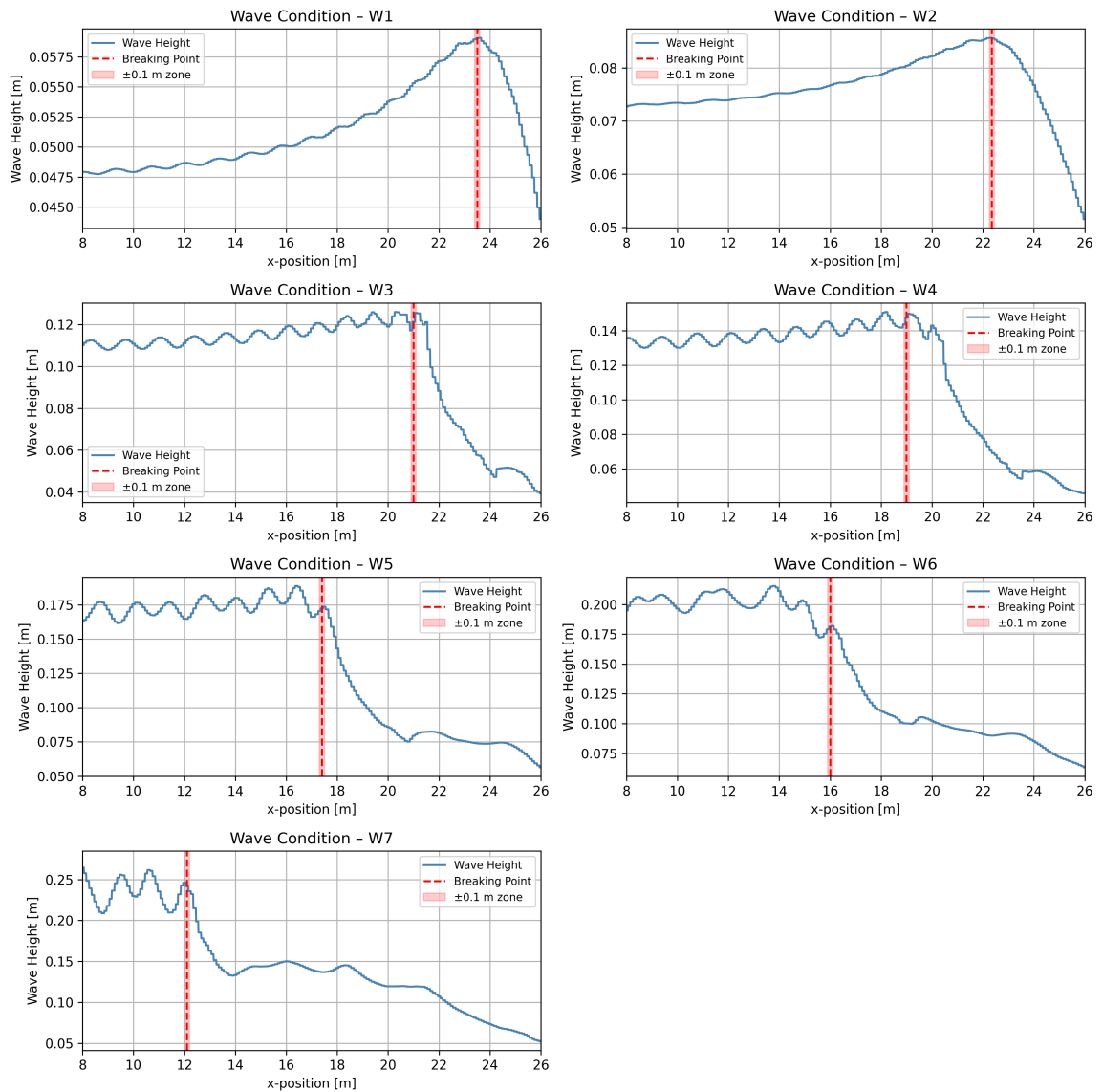


Figure 4.3: Wave height horizontal profile for all wave conditions (W1 - W7) from the toe of the slope with indication of the experimentally determined breaking zone.



Figure 4.3 shows the evolution of the wave height along the flume. Periodic oscillatory patterns in wave height are recognisable for all wave conditions. This can be linked to wave energy reflection. While propagating along the flume, waves encountered boundaries such as the slope and the flume physical boundaries, which caused part of their energy to be reflected back towards the wave generator. The interaction between the incoming and outgoing energy led to interference, causing oscillatory patterns in wave height. The entity of these disturbances progressively increases with the more energetic wave conditions. Their amplitude increases from the order of magnitude of 0.1 millimetres for W1 to approximately 1 centimetre for W7. In addition, the patterns lose their clear regularity as the wave conditions become more energetic.

A clear trend in the wave height evolution can be observed for all wave conditions. The wave height increases steadily from the toe of the slope ( $x = 8\text{m}$ ) onwards up to a peak, after which it drastically drops. This sudden drop in wave height is nicely aligned with the experimentally determined breaking zone. The observed wave height profile correctly represents the expected behaviour of wave propagation towards the shoreline. This confirms the ability of the model to reproduce the wave shoaling, capture the instability that causes breaking and simulate the energy dissipation in the surf zone. Nonetheless, anomalies in the simulated results arise after breaking. For wave conditions W3 to W7, the wave height evolution displays unexpected patterns immediately following the dissipation of most wave energy. This further supports the argument that SWASH provides reliable results up to the point of breaking, but that its output beyond this point should be interpreted with caution.

The simulated data obtained from SWASH were aligned at the particle deployment zone for fair comparison between the wave conditions. Figure 4.4 shows the relevant spatial domain for each wave condition, the x-axis is set at 0 at the particle release point, which was set to be one meter before breaking.

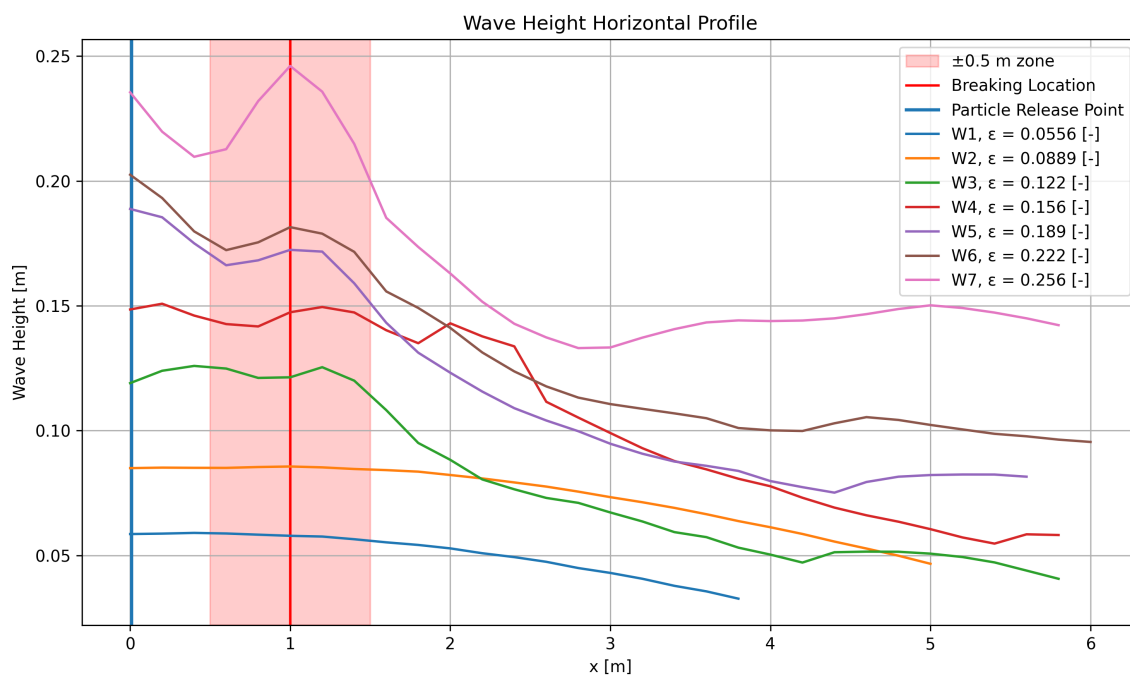


Figure 4.4: Wave height horizontal profile for all wave conditions (W1 - W7) aligned at particle release point (one meter before the breaking point) with indication of the experimentally determined breaking zone.

### 4.3. Particle Transport

This section presents the observed particle transport behaviour under the seven experimental wave conditions. Particles were released one metre before wave breaking and their movement was

recorded by cameras filming from the top and from the side. The results presented below will be focused on the top-view trajectories obtained from the tracking algorithm described in Section 3.6.3.

### 4.3.1. Particle Horizontal Trajectories

This research primarily focused on the movement of the simulated MPD along the horizontal direction of the wave flume. The horizontal displacement of all particle trajectories is summarised in Figure 4.5, each wave condition W1 - W6 was assigned a different colour, two types of lines are visible, the bold solid line represents the average particle horizontal displacement, whereas single trajectories are shown with thin, faint lines. The horizontal displacement for particles experiencing wave condition W7 are not displayed in the plot as data was only available for the first two metres from the release point. Notable differences in both distance travelled and time spent in the flume can be observed for the particles undergoing the different wave conditions. For all the displayed wave conditions, a window in horizontal distance of 4.5 to 5 metres was captured, within which particle motion was quantitatively assessed. Nonetheless, particles undergoing wave conditions W1 and W2 never travelled such distances. This is because of the shift in breaking point location along the flume, discussed in Section 3.2.3. The particles undergoing the less energetic conditions (W1 - W2) went through breaking further onshore on the slope. For these two scenarios the amount of measured x-displacement was limited by the particles reaching the end of the slope and beaching which occurred within the measuring window after respectively 3 metres and 4.5 metres on average.

There is a clear distinction between the average trajectories of the particles undergoing the different wave conditions. This observation strengthens the initial hypothesis that offshore steepness can be used as a parameter to categorise particles behaviour based on the offshore steepness characterising the waves they are subject to, as it is shown to influence the extent and timing of particles horizontal motion across the different wave conditions. It is possible to observe how the steepness of the lines representing x-displacement over time increases gradually from wave condition W1 to wave condition W6. This indicates an increase in particle horizontal drift velocity with the increasing offshore steepness values related to W1 - W6. In addition, particles reach their maximum displacement more quickly as the waves become more energetic, showing a faster initial transport for wave conditions W5 and W6, which reach their maximum displacement on average within 10 seconds, compared to W1 and W2 which take substantially longer (an average of 40 seconds and 30 seconds respectively).

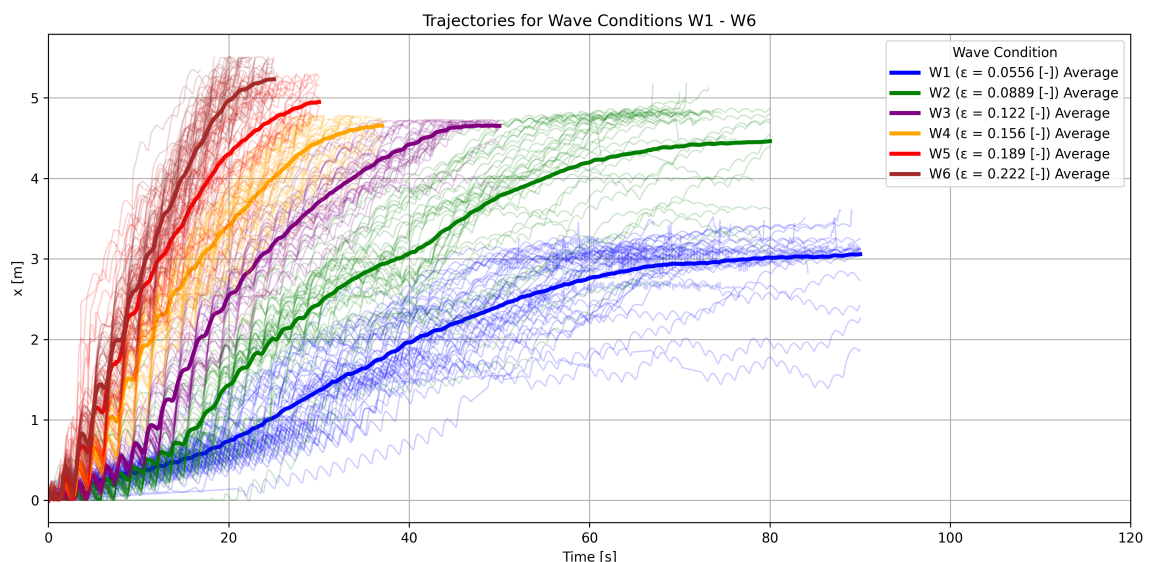


Figure 4.5: Particle x-coordinate over time for wave conditions W1 – W6. Each faint line represents an individual particle trajectory, and bold lines indicate the average trajectory for each condition.

### 4.3.2. Particle Horizontal Drift Speed Along the Flume

To provide an initial overview of the effect of offshore wave steepness on the transport of plastic particles, the mean particle speed was computed for wave conditions W1 - W7 and is shown in Figure 4.6. The results suggest an increase in average drift speed with increasing offshore steepness ( $\epsilon$ ).

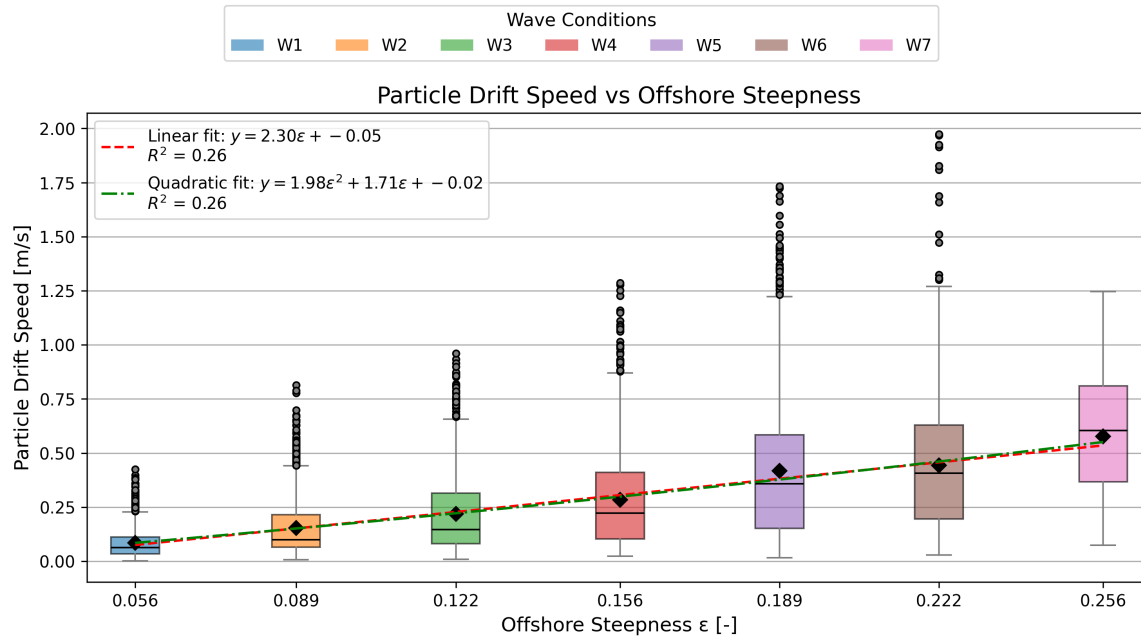


Figure 4.6: Mean horizontal particle speed for wave conditions W1 to W7. Bars represent the average transport speed computed across all particle trajectories for each wave condition, with error bars indicating the standard deviation, diamonds representing the means and outliers depicted as dots. A trend line and a quadratic fit are applied to the whole dataset, and an indication of the  $R^2$  value of the fit is provided.

The overall particle horizontal drift speed was divided into relevant zones, shoaling (0 - 0.5 m), breaking (0.5 - 1.5 m) and surf (1.5 - 2.5 m) zones, for which the mean speed was computed. Figure 4.8 shows the distribution across the zones of the computed particle drift for each wave condition, characterised by increasing offshore steepness represented on the x-axis. The mean values are highlighted and a trend line was fit through the whole dataset. In all three zones, particle drift speed tends to increase with offshore steepness, but the rate and the variability of this increase vary spatially. In the shoaling zone, speeds are lower and show the least response to the changing offshore steepness with the linear fit presenting a slope of 2.01 m/s per unit  $\epsilon$ . Particle drift speed values generally increase in the breaking zone and the sensitivity to changes in offshore steepness becomes more intense with a slope of 2.89 m/s per unit  $\epsilon$ . Lastly, in the surf zone, particles continue to be pushed onshore by the residual energy after breaking, the speed values are lower than at breaking and increase with the increasing offshore steepness at a rate of 2.16 m/s per unit  $\epsilon$ .

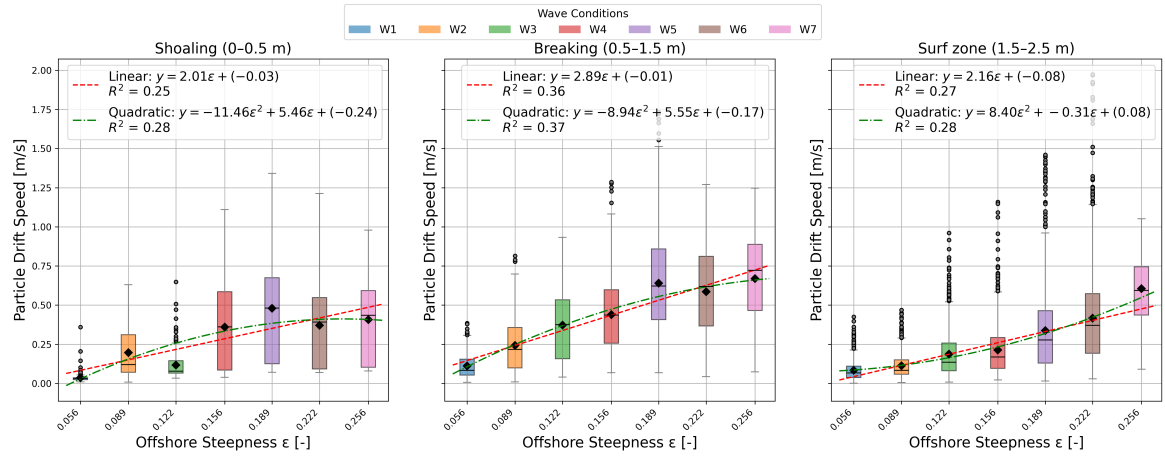


Figure 4.7: Mean horizontal particle speed for wave conditions W1 to W7 for the shoaling, breaking and surf zone plotted against offshore steepness. Bars represent the average transport speed computed across all particle trajectories for each wave condition, with error bars indicating the standard deviation, diamonds representing the means and outliers depicted as dots. A trend line and a quadratic fit are applied to the whole dataset, and an indication of the  $R^2$  value of the fit is provided.

A similar analysis was conducted relating the particle horizontal drift speed relative to the three flow regimes to the local steepness in each zone. This resulted in local steepness values increasing according to the increasing offshore steepness for the shoaling and breaking zones, with the exception of wave conditions W5 and W6, which showed similar steepness values in both zones. For the surf zone, the computed local steepness values did not follow the increasing offshore steepness. This can be attributed to the fact that the shape of the waves after their complete collapse during breaking limits the meaning and the reliability of the determination of local steepness in this zone.

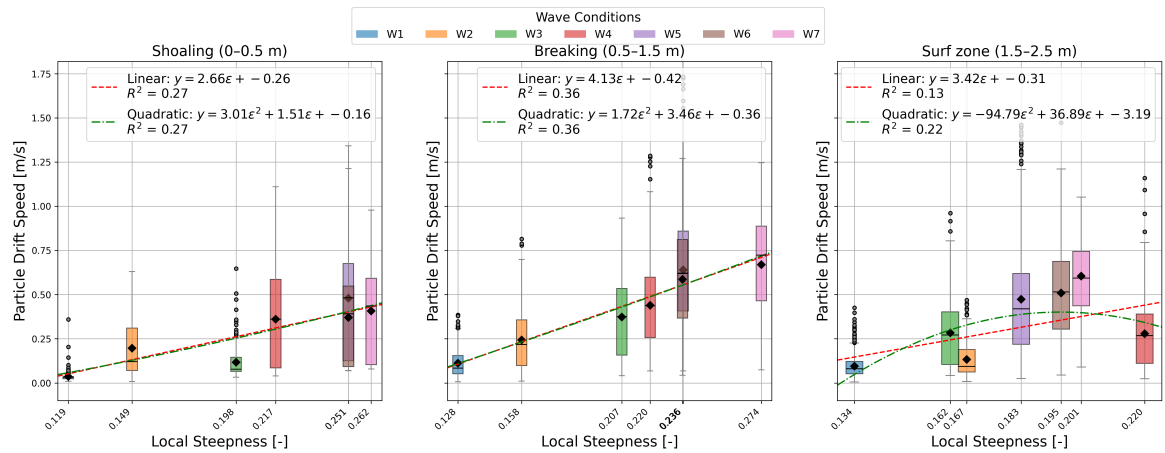


Figure 4.8: Mean horizontal particle speed for wave conditions W1 to W7 for the shoaling, breaking and surf zone plotted against local steepness. Bars represent the average transport speed computed across all particle trajectories for each wave condition, with error bars indicating the standard deviation, diamonds representing the means and outliers depicted as dots. A trend line and a quadratic fit are applied to the whole dataset, and an indication of the  $R^2$  value of the fit is provided.

The particle horizontal drift speed was further analysed to better understand the evolution of the transport along the flume. Each curve shown in Figure 4.9 represents the mean horizontal drift velocity binned in 0.2 metres intervals for particles undergoing wave conditions W1 - W7, represented in different colours. The vertical error bars indicate the standard deviation within each bin. A red shaded region is included showing the particles release location and a grey shaded area marks the breaking zone. Wave condition W7 is included in the plot despite the limited data availability in horizontal direction.

For all conditions the particle horizontal speeds follow a common evolution pattern. A rapid increase in speed is observed from the release zone until the breaking zone, where speed values peak and are followed by a more gradual decrease. The extent and intensity of the peak identified around the breaking zone vary across the wave conditions.

It is possible to observe how wave conditions W6 - W7 lead to higher particle speeds throughout the whole region of interest. Lower energy waves instead (W1, W2) result in lower particle speeds, especially after breaking.

For wave conditions W6 and W7 particles continue to move at higher speeds also after the breaking zone, up until 3.5 metres after the release zone, indicating stronger post-breaking transport mechanisms. Wave conditions W1 and W2, instead, show a quicker decrease in speed after the peak. Overall, consistent trends can be identified across the wave conditions considering the confidence bounds, with clear differences in magnitude between the extreme tested conditions W1 - W2 and W6 - W7.

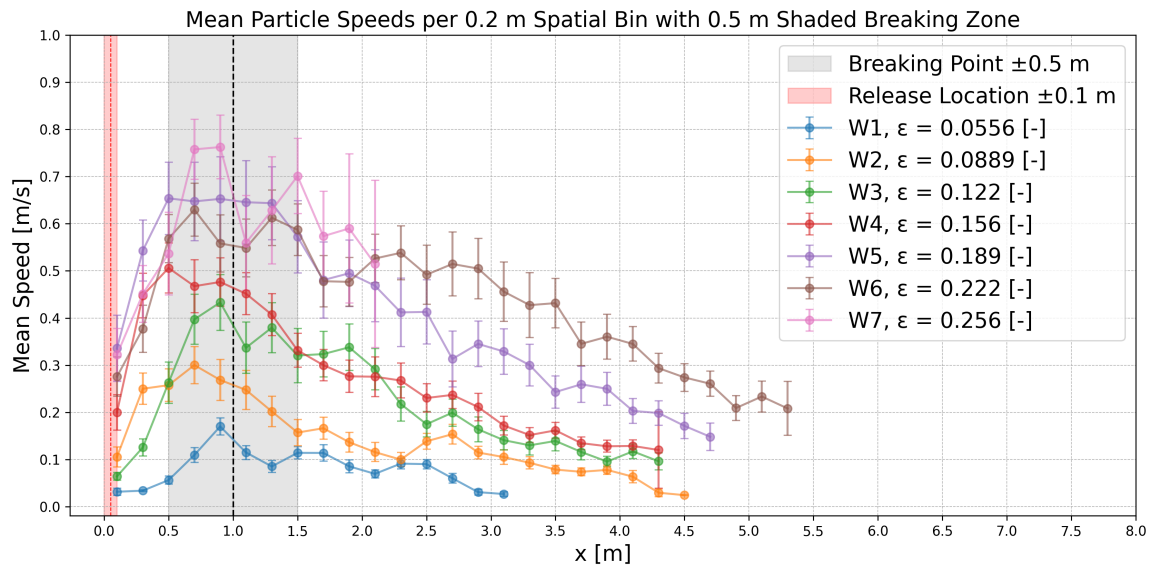


Figure 4.9: Mean particle horizontal drift velocity along the flume, evaluated in 0.2-metre segments along the flume, for wave conditions W1 to W7. Each curve represents the average speed of the particles, with error bars indicating their standard deviation. The red shaded area marks the particle release zone, while the grey shaded region and dashed line indicate the experimentally determined location of wave breaking.

## 4.4. Wave Propagation Velocities

The wave dynamics experienced by the plastic particles during their movement in the flume were further analysed by computing three characteristic wave propagation velocities: the Stokes drift, the crest speed and the phase speed.

### 4.4.1. Stokes Drift

The Stokes drift was estimated along the relevant sections of the flume by using the mean wave height values obtained from the SWASH simulations. It was important to examine how the Stokes drift evolved along the flume, as it is influenced by the local wave steepness, which is subject to changes as waves propagate toward the shore according to the sloped bathymetry. The obtained Stokes drift values are presented for wave conditions W1 - W7 in Figure 4.10. For each condition, both Stokes drift and local steepness are plotted against the x-direction of the flume. As waves propagate along the slope, the local steepness increases culminating at the breaking zone. This results in an increase in Stokes drift, highlighting its dependence on local steepness.

For wave conditions W3 - W7, for which the change in local steepness at breaking is more accentuated, it is possible to observe a variability in both steepness and Stokes drift in the order of magnitude of 0.01 metres in the breaking region. This can be linked to the high complexity of the wave transformation dynamics at breaking, which seem not to be perfectly captured by the SWASH model.

It is important to notice how the mean wave height values used for the computation of the Stokes Drift are obtained by averaging the model's results over a large number of waves (360). This causes the final Stokes drift values to be affected by both the implicit model uncertainty and the uncertainty behind the averaging process. This last contributor was computed and assessed to be negligible, it is therefore not provided in Figure 4.10 and Figure 4.12. The determination of the Stokes drift is considered robust until the breaking point and less applicable from there on according to the results presented in Section 4.2.2. All of the mentioned contributions need to be taken into account while interpreting the results.

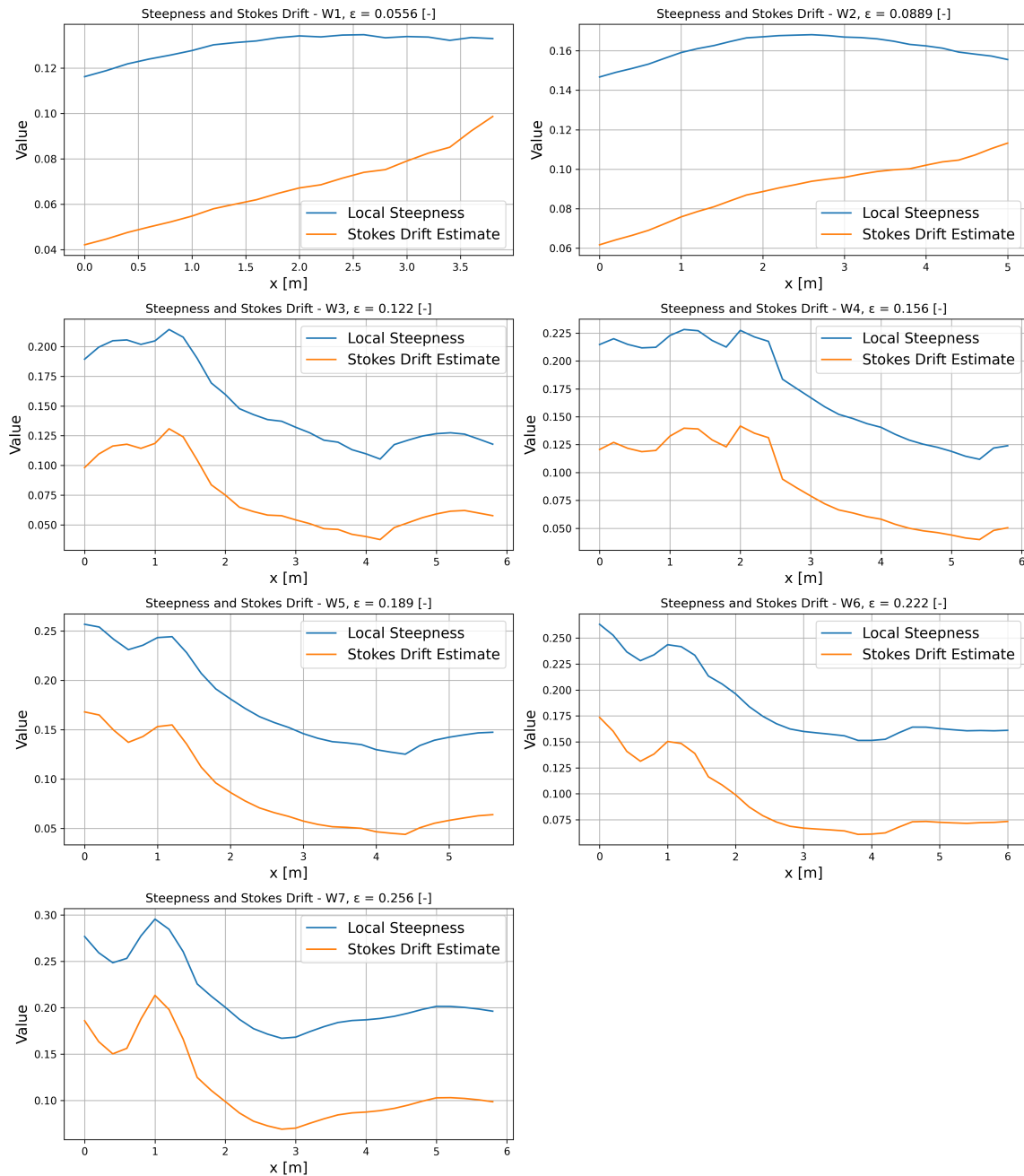


Figure 4.10: Mean Stokes drift and local wave steepness for wave conditions W1 - W7 along the flume computed from the results of the SWASH simulations.

#### 4.4.2. Crest Speed

The crest speed was determined using the simulated surface elevation data obtained from the SWASH model. In order to ensure good agreement with the actual observed crest speed values, the simulated crest speed was validated against a set of manually tracked crest speed values for wave condition W3. The results of the comparison are displayed in Figure 4.11.



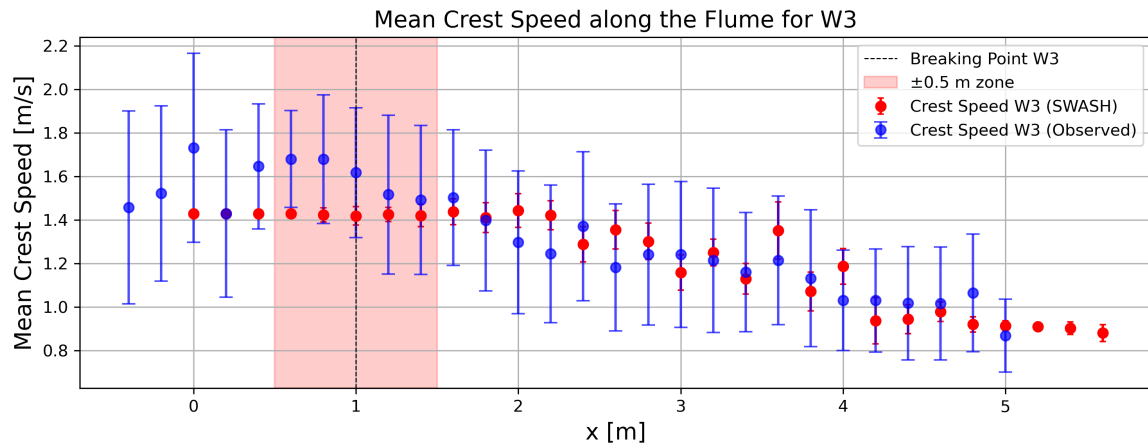


Figure 4.11: Mean crest speed along the flume measured from video tracking (blue) and simulated using SWASH (red). Error bars indicate the standard deviation behind the observed and modelled values. The dashed line marks the experimentally determined breaking point. The shaded area represents the breaking zone.

It is possible to notice how the simulated and measured crest speed values align considering the confidence bounds. The uncertainty behind these values can be attributed to the averaging over a space domain of 0.2 metres for both methods. In addition, for the measured values, a source of uncertainty must be linked to the limited number of waves manually tracked and to human error in the tracking process. Considering the uncertainty behind both derivations of the crest speed, the two methods are considered equivalent in computing reliable values. This conclusion is therefore extended to all the remaining wave conditions for which crest speed is estimated based on the SWASH model results.

#### 4.4.3. Phase Speed and Crest Speed

Phase speed was theoretically determined starting from the simulated mean wave height profiles. This was done by applying its formulation according to the linear wave theory and a second expression to account for non-linear behaviour. This was done for wave conditions W1 - W7 and is displayed in Figure 4.12.

Figure 4.12 presents both the crest speed values obtained from the SWASH simulations and the theoretical phase speed estimates. The shaded grey area between the two theoretical curves represents the deviation introduced by non-linear effects. The evolution of crest speed and phase speed along the x-direction of the flume follows a similar pattern, as expected. As the water depth decreases along the x-direction of the flume towards the end of the slope, the wavelength decreases accordingly and the phase and crest speeds of the wave become gradually lower. Both phase speed and crest speed increase progressively with increasing offshore steepness from W1 to W7, reflecting the influence of the offshore wave steepness on wave propagation speeds.

The theoretical estimates for phase speed according to linear wave theory consistently lie below the non-linear approximation and the simulated crest speed, causing an underestimation of both. This is to be expected given the dominance of non-linear effects arising from the interaction of the waves with the sloped bathymetry of the flume as they propagate onshore.

The crest speed values obtained from SWASH tend to align more closely with the non-linear approximation of phase speed, especially for the steeper conditions. As anticipated, the crest speed estimates for the more energetic conditions (especially W7) show greater uncertainty which should be taken into account in the analysis. Nonetheless, crest speed estimates, considering the confidence intervals, lie between the lower bound (phase speed, linear approximation) and upper bound (phase speed, non-linear approximation) for all wave conditions. The shaded area will therefore be used as a reference for the estimates of phase and crest speeds.



## Crest and Phase Speeds for All Wave Conditions

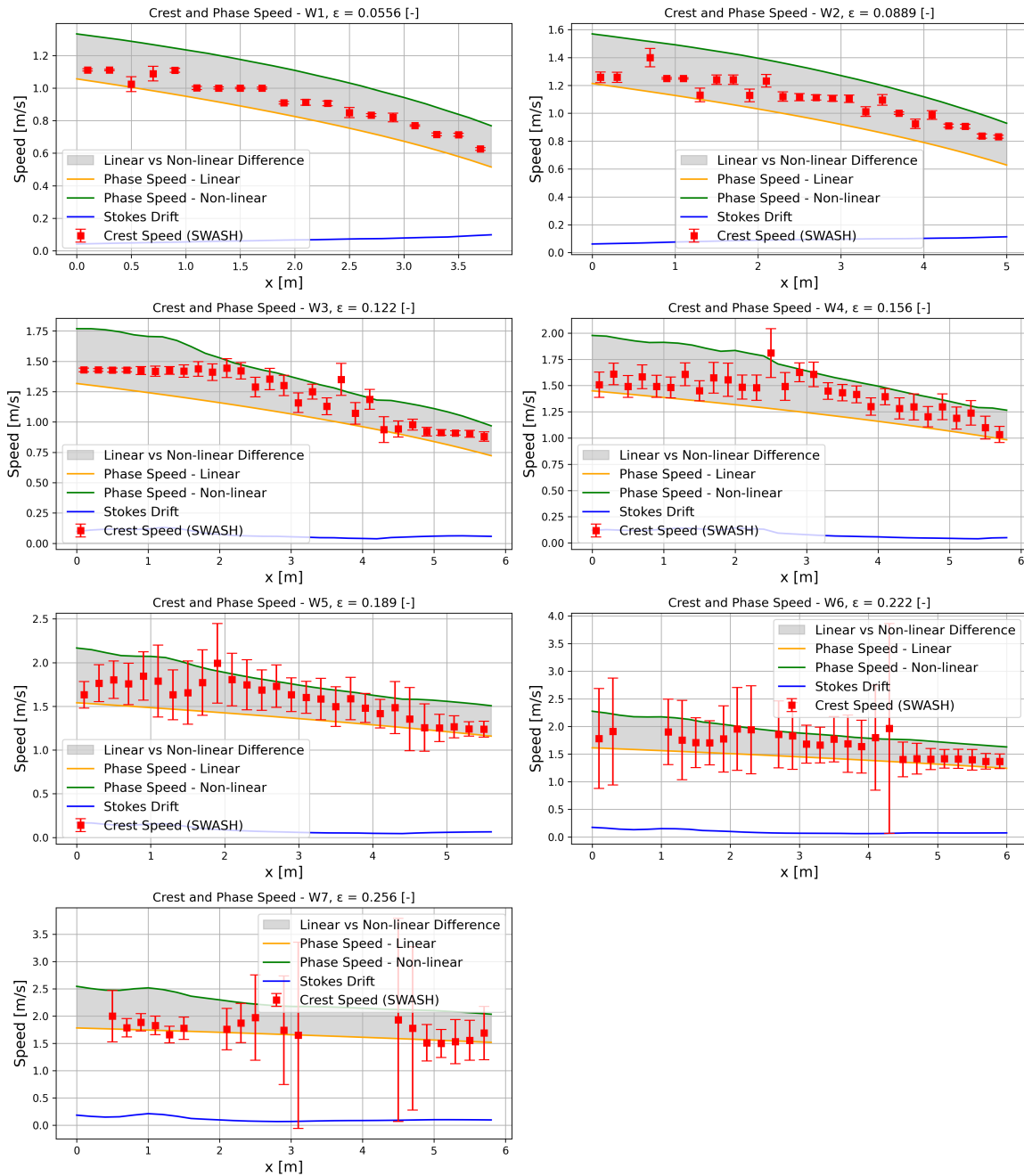


Figure 4.12: Crest and phase speed estimates along the flume for wave conditions W1 - W7. Phase speed is shown using both linear (orange) and non-linear (green) approximations, with a shaded grey area indicating the difference between them. Red squares represent crest speed values obtained from SWASH simulations with error bars showing the standard deviation.

#### 4.4.4. Particle Drift Speed vs. Wave Propagation Velocities

In order to describe the behaviour of plastic particles in the last meters before beaching, the horizontal drift speed of the particles was compared to the computed crest speed, phase speed and Stokes drift.

Given the necessity to assess the evolution of the wave propagation velocities and the particle horizontal drift velocity along the flume for the seven wave conditions, the results are summarised in

a three-dimensional plot shown in Figure 4.14. The visualisation includes the spatial distribution of horizontal particle drift velocity, Stokes drift, and the theoretical phase speed ranges along the flume plotted against the offshore wave steepness, unique for every wave condition. Each colour represents one wave condition W1 - W7, with an indication of the relative offshore steepness value ( $\epsilon$ ). For each condition, shaded bands show the range between linear and non-linear phase speeds, solid lines the modelled Stokes drift and scatter points the experimental mean particle horizontal drift speed.

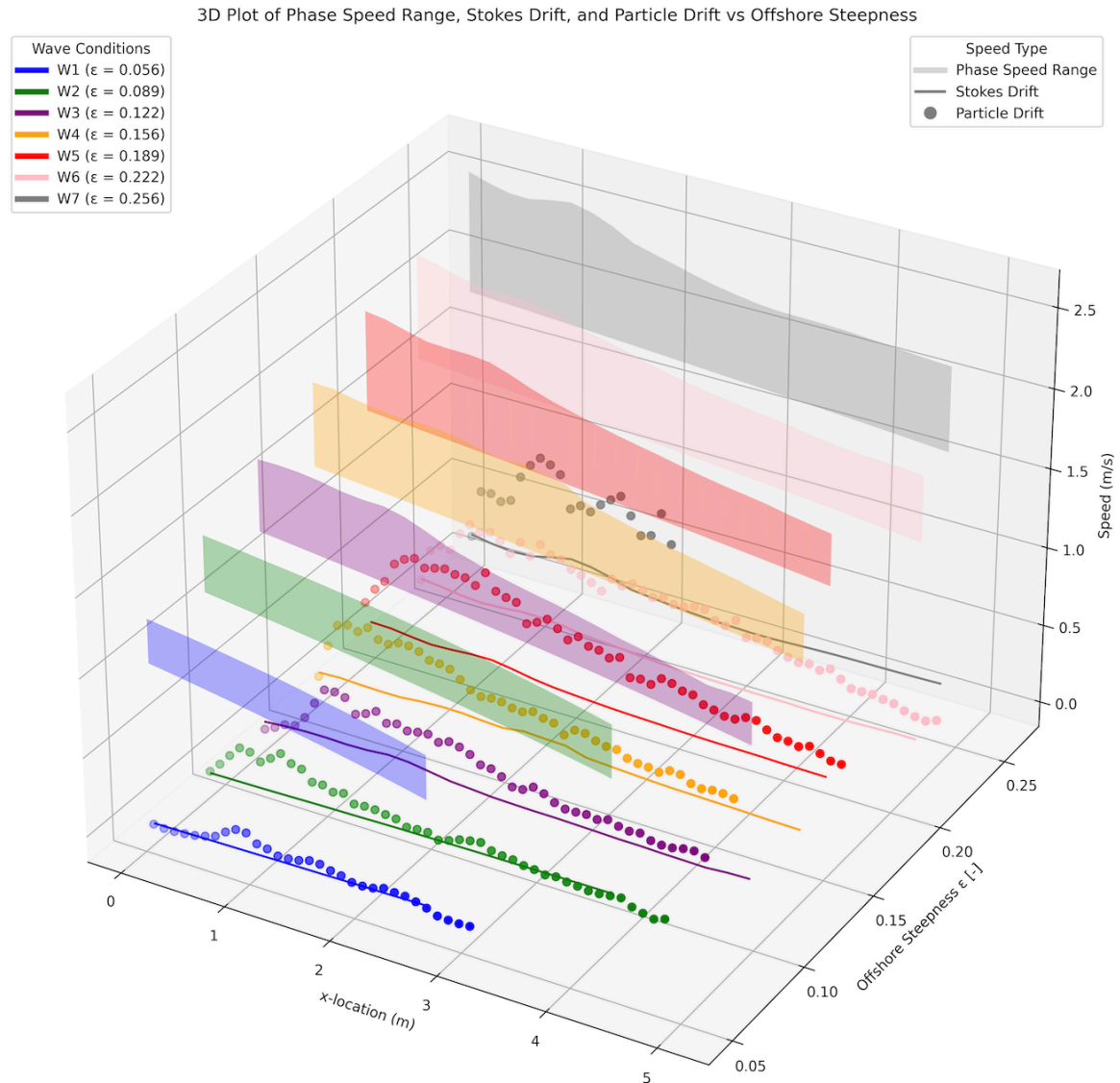


Figure 4.13: 3D plot showing the spatial evolution of particle drift (dots), Stokes drift (lines), and the theoretical phase speed range (shaded bands) along the flume for seven wave conditions with specific offshore steepness values represented in different colours.

For better visualisation, the results summarised in the 3D plot are displayed with seven different plots, one for each wave condition W1 - W7, showing particle horizontal drift speed, Stokes drift and a shaded area around the upper and lower bound of the phase speed estimates.

## Comparison of Particle Drift with Wave Propagation Estimates

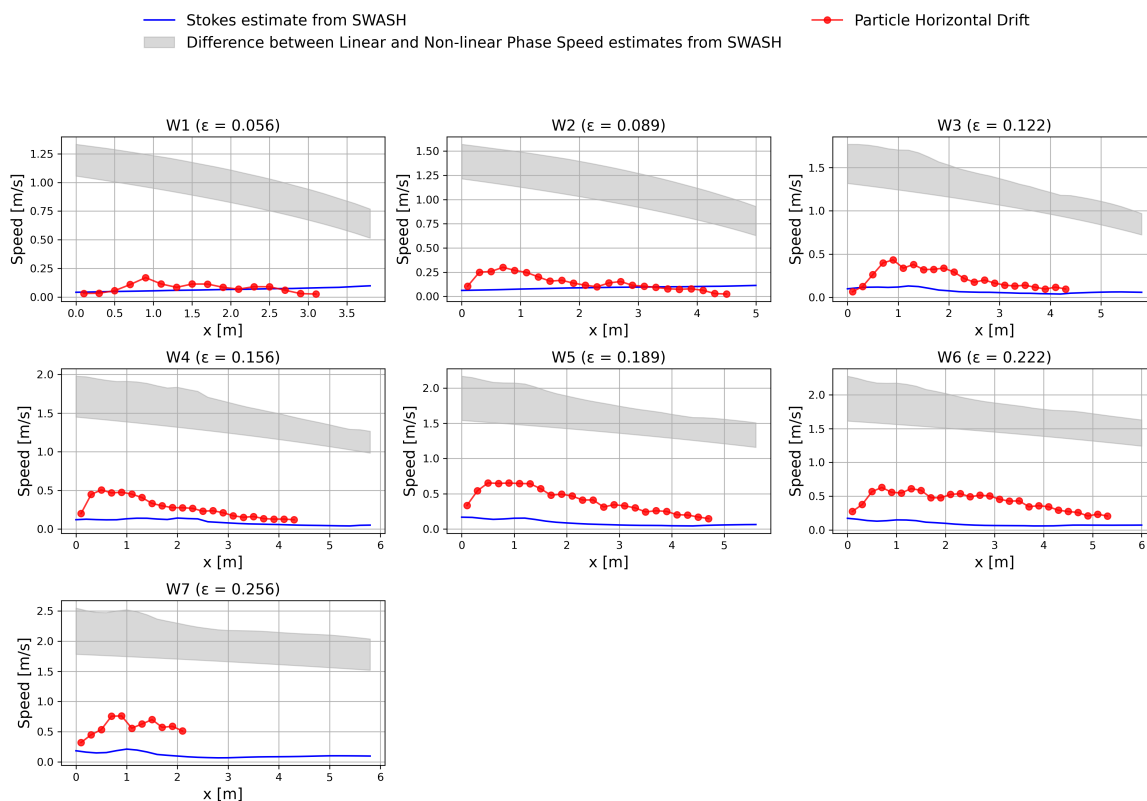


Figure 4.14: Spatial evolution of particle drift (dots), Stokes drift (lines), and the theoretical phase speed range (shaded bands) along the flume for wave conditions W1-W7.

The analysis conducted so far revealed how the particle horizontal drift speed starts to deviate from the Stokes drift right around breaking. This region was therefore further investigated by looking at speed metrics around the experimentally determined breaking zone. This allows for the elimination of one of the three dimensions as local steepness is assumed to be constant in the 0.5 metres interval around  $x = 1$  m, defined as the breaking zone.

Figure 4.15 provides an overview of the local wave steepness at breaking for wave conditions W1 - W7. It can be observed how the local steepness values increase progressively with wave condition (and relative offshore steepness) starting from a value of approximately 0.13 for W1 and reaching a value of almost 0.30 for W7. The change in local steepness at breaking between wave conditions W5 and W6 is minimal, it was therefore decided to exclude W6 from the analysis. This similarity can be observed by looking at the evolution of the local wave steepness over the  $x$ -direction for the two conditions provided in Figure 4.16. The shape of the graph suggests similar values of wave steepness up until after the breaking zone, supporting the decision to exclude W6. The overall trend confirms the increase in local steepness at breaking with increasing offshore steepness values.

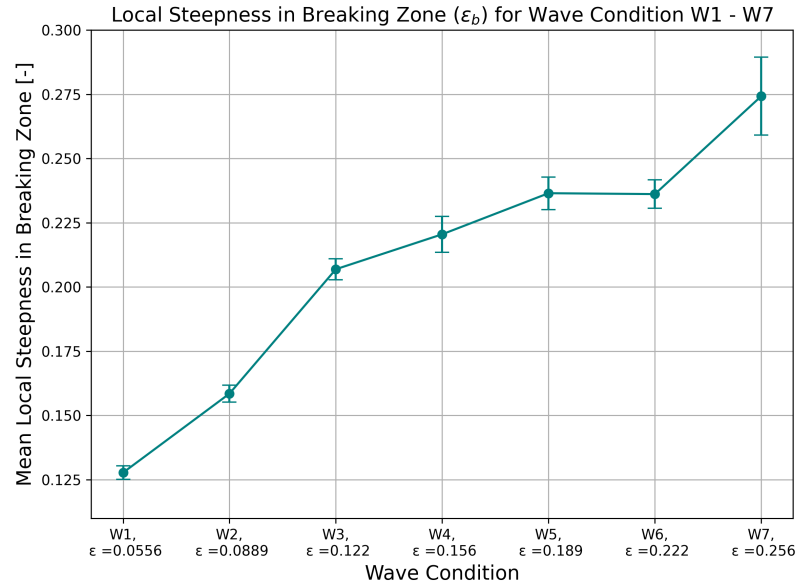


Figure 4.15: Mean local wave steepness in the breaking zone for wave conditions W1 to W7. Error bars represent the standard deviation within the considered zone.

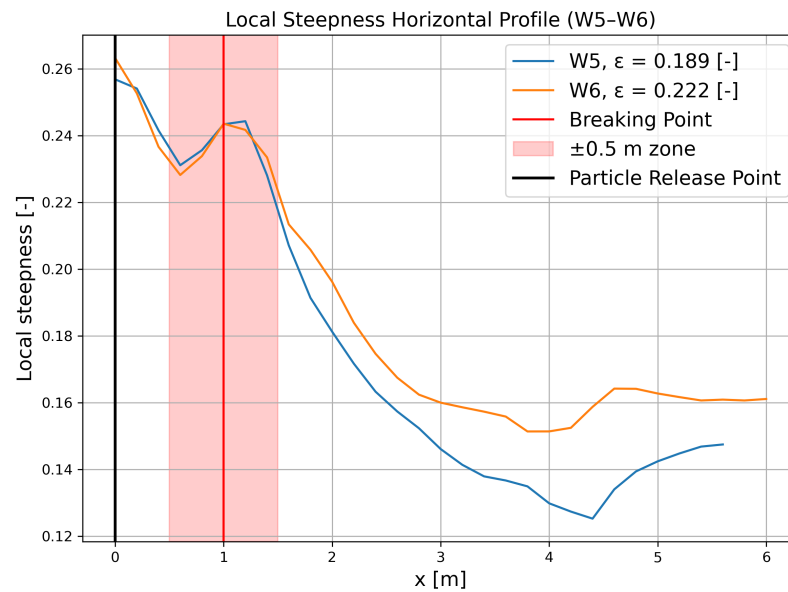


Figure 4.16: Evolution of local wave steepness along the x-direction for W5 and W6 with indication of the relative offshore steepness values.

Velocity estimates for crest speed, Stokes drift and particle horizontal drift speed were computed at breaking to assess their relations in this region. Figure 4.17 shows the relationship between local wave steepness at breaking and the three speed metrics. Each data point corresponds to a different wave condition with local wave steepness on the x-axis and speed on the y-axis.

Crest speed, shown with green crosses, shows the highest values among the metrics and increases gradually with local steepness. Stokes drift, indicated by orange dots, also increases with steepness but with a smaller magnitude.

Particle horizontal drift speeds at breaking are displayed with blue markers with error bars. These

values fall between Stokes drift and crest speed and increase with increasing local steepness. The observed increase in horizontal drift speed appears consistent, showing larger uncertainty at higher local steepness values.

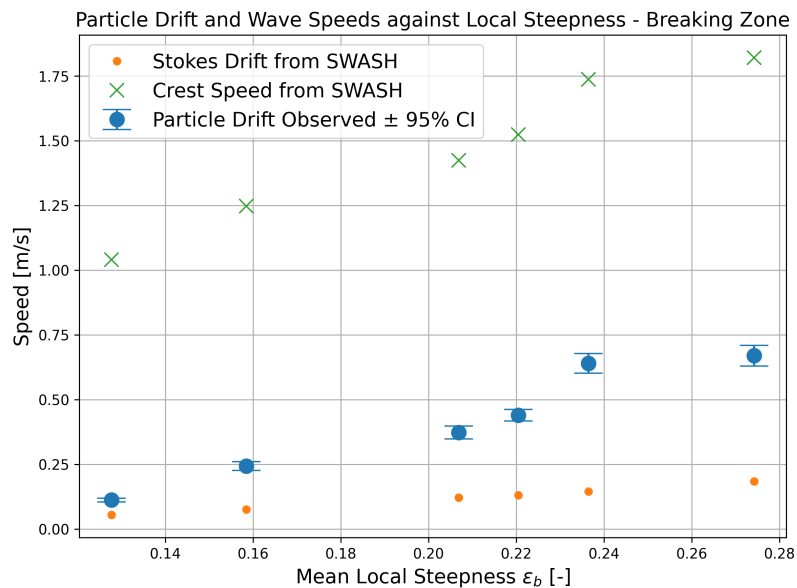


Figure 4.17: Relationship between local wave steepness at breaking and three speed metrics: Stokes drift (orange), crest speed (green), and particle drift (blue).

Particle horizontal drift speed values were normalised relative to Stokes drift and crest speed in order to evaluate which wave-driven mechanism could better represent the observed particle transport and test whether offshore wave steepness influences their relationship. Figure 4.18 shows the normalised particle horizontal drift speeds relative to Stokes drift (left panel) and crest speed (right panel) plotted against local wave steepness at breaking. A horizontal red line at 1 represents the baseline where the particle drift would equal the two reference speed metrics.

The ratio of particle drift to Stokes drift exceeds 1 at every local steepness value, showing that the particles move consistently at greater speeds than Stokes drift across all the wave conditions. The ratio values range approximately between 2 and 4 and show a slightly increasing trend as local steepness increases. This results in particle drift speed progressively deviating from the Stokes drift for progressively steeper waves at breaking.

On the other hand, the ratio of particle drift to crest speed never exceeds 0.4. A positive trend is still present and the linear fit shows better agreement with the data. Here, the increasing trend indicates that particle drift speeds become progressively closer to the crest speed estimates as local steepness at breaking increases.”

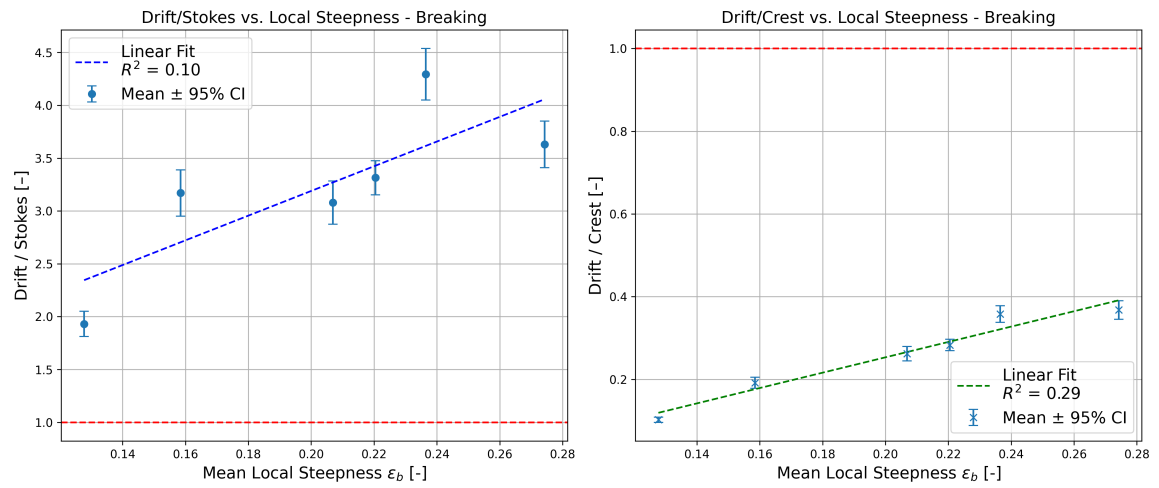


Figure 4.18: Mean local wave steepness in the breaking zone for wave conditions W1 to W7.

**Legend:** 100% overlap 90% overlap with minimal adjustments 0% overlap

# 5

## Discussion

The following sections provide the interpretation of the obtained results in relation to the research questions of this study. The main findings are presented and related to existing literature, highlighting both consistencies and discrepancies, and providing insights into their broader implications.

The primary research question guiding this study aims to understand and characterise the influence of wave steepness on the horizontal transport and beaching of marine plastic debris under controlled wave conditions. This was done by conducting laboratory experiments, which allowed for the comparison of the behaviour of identical plastic particles ( $l/\lambda = 0.014 - 0.05$ ,  $\rho_o/\rho_w = 0.75$ ) representing marine plastic debris undergoing seven different wave conditions characterised by an offshore steepness value ranging from  $\epsilon = 0.056$  to  $\epsilon = 0.256$ .

In order to characterise MPD transport under breaking waves in shallow water, the study focused on the influence of offshore wave steepness on MPD horizontal drift speed. Given the specific features of the experimental setup, which involved the presence of a sloped bottom and intermediate to very shallow water depths, the role of the breaking zone as a potential primary driver of onshore horizontal drift was investigated in detail. In order to relate the observed particle behaviour to known wave propagation speed components, the study aimed to compare particle speed to the wave crest speed and the Stokes drift. Finally, the study assessed whether offshore steepness could serve as a predictive parameter for classifying MPD behaviour in the nearshore zone, with the aim of improving the predictive performance of transport models.

Past studies have been investigating the influence of wave steepness on particle drift behaviour by conducting laboratory experiments (Alsina et al. 2020; Xiao et al. 2025; Huang et al. 2013; Li et al. 2023; He et al. 2016; Núñez et al. 2023; Huang et al. 2011; Calvert et al. 2024; Ross Calvert et al. 2021; Eeltink et al. 2023; Tanizawa et al. 2001). Table 5.1 provides a summary of the main experimental studies previous to this research, presenting the differences between the tested conditions. The considered body of literature highlighted the need for additional experimental work on shallow-water breaking waves in the nearshore environment. The current study seeks to complement the existing knowledge by addressing some of the most underrepresented experimental conditions. Specifically, waves that break and propagate in shallow-water regimes under the influence of a simulated beach. While most experimental research to date has been focused on the transport of free-floating objects under deep-water conditions, the effects of a sloped bottom and the associated transitions in flow regime with their impact on transport behaviour remain relatively unexplored. The current work aims to contribute to the improvement of the understanding of the nearshore MPD transport processes by considering the effects of offshore steepness and wave-slope interactions under shallow-water conditions.

| Study                      | Flow regime | Wave type | Breaking | Sloped bottom | Steepness    | Relative size [%] | Positive relation $\epsilon - u_b$ | Type of relation       |
|----------------------------|-------------|-----------|----------|---------------|--------------|-------------------|------------------------------------|------------------------|
| Tanizawa et al. (2001)     | I + D       | R + IR    | -        | No            | 0.03 - 0.20  | 12.7 - 63.6       | Yes                                | Size dependent         |
| Huang et al. (2011)        | D           | R         | No       | No            | 0.04 - 0.15  | 12.8 - 15.8       | Yes                                | Quadratic              |
| Huang et al. (2013)        | D           | R         | No       | No            | 0.04 - 0.32  | 61 - 308          | Yes                                | Linear, steepness dep. |
| He et al. (2016)           | D           | R         | No       | No            | 0.04 - 0.30  | 9.2 - 30.4        | Yes                                | Size dependent         |
| Lenain et al. (2019)       | D           | WG        | Yes      | No            | 0.24 - 0.46  | < <               | Yes                                | Breaking dependent     |
| Alsina et al. (2020)       | I           | R         | No       | No            | 0.05 - 0.22  | 1.2 - 14          | Yes                                | Quadratic              |
| Ross Calvert et al. (2021) | D           | WG        | No       | No            | 0.1          | 1.9 - 5.1         | -                                  | -                      |
| Calvert et al. (2024)      | D           | R         | Yes      | No            | 0.12 - 0.38  | 0.5 - 19.2        | Yes                                | Linear                 |
| Li et al. (2023)           | I + S       | R         | Yes      | Yes           | 0.07 - 0.36  | 1 - 3.4           | Yes                                | -                      |
| Núñez et al. (2023)        | I + S       | R + IR    | Yes      | Yes           | 0.081 - 0.21 | 0.1 - 12          | Yes                                | -                      |
| Eeltink et al. (2023)      | D           | IR        | Yes      | No            | 0.07 - 0.24  | 0.9               | Yes                                | Breaking dependent     |
| Xiao et al. (2025)         | D           | R         | No       | No            | 0.03 - 0.32  | 2.6 - 27.1        | Yes                                | Size dependent         |
| Present study              | I + S       | R         | Yes      | Yes           | 0.05 - 0.26  | 1.4 - 5           | Yes                                | -                      |

Table 5.1: Summary of literature on wave-induced drift: flow regimes, steepness ranges, object sizes, and particle drift-wave steepness relation. All the values were directly taken from the studies when available; when not directly made explicit, the needed entries were computed according to the linear dispersion relationship, applying the Fenton approximation for implicit solving. Flow regime is defined as D (deep water), I (intermediate water), and S (shallow water). Wave type is defined as R (regular waves), IR (irregular waves), and WG (wave groups).

## 5.1. MPD Horizontal Drift Speed and Wave Steepness

The analysis of plastic particle trajectories undergoing waves with increasing wave steepness showed a clear distinction between the tested conditions. A positive trend in particles horizontal drift speed was observed, as higher wave steepness conditions consistently produced faster transport of plastic particles across the flume. The overall horizontal drift speed increased by 60% for a doubling of the offshore wave steepness.

Analysing the uncertainty behind the computed particles drift speed reveals that particles response becomes more variable under wave conditions characterised by higher offshore steepness values. As particles travel over the sloped bottom, more violent breaking and overall turbulent dynamics lead to a greater spread in measured speeds.

The increase in particle horizontal drift speed according to steepness suggests that particles undergoing more energetic wave conditions may experience a higher likelihood of beaching. The observed pattern relates to occurring natural processes. Rapid stranding of widespread MPD was recorded during extreme weather conditions, analysed by Lo et al. (2020) and considered in the context of laboratory observation by Li et al. (2023). Similarly, a field campaign conducted along the South Wales coastline, UK, revealed how higher wave energies between surveys were associated with higher levels of previously unseen litter (Williams et al. 2001).

Overall, similar trends were observed in the studies presented in Table 5.1 which all agree with the current research on the positive relation of particle drift to wave steepness. The nature of the commonly identified positive correlation between steepness and particle drift is still under debate within the existing studies. The considered body of literature is divided between Authors who refer to the correlation as linear and Authors who instead observed quadratic scaling. It is important to acknowledge the limitations in direct comparison between different laboratory studies given the very specific experimental setup and tested conditions.

The current study allowed for the observation of a positive trend between offshore steepness and particle horizontal drift speed. However, the nature of the trend remains inconclusive as both linear and quadratic fits provide low values of coefficients of determination. It is still possible to observe how, despite the added second-order term of the quadratic model, the resulting curve almost completely overlaps with the linear fit. This suggests that the contribution of the added term would be negligible in practical terms, causing the quadratic fit to collapse on the linear model. The low values of both coefficients of determination should still be considered carefully.

Existing literature suggests that the trend observed in this research would be more likely explained by a linear relation between the particle drift and wave steepness. This hypothesis, considering the differences in experimental conditions, is in agreement with the conclusions of the experimental studies conducted by Tanizawa et al. (2001), Calvert et al. (2024), He et al. (2016), and Xiao et al. (2025), who observed how the relation between the two variables tends to divert from the purely quadratic dependence of the particles drift speed to steepness which would be expected for Lagrangian tracers. The mentioned studies observed a transition to a linear relation with the increase



of the relative size of the travelling objects. The objects used in the current study fall within the ranges of relative size for which a linear trend was observed ( $l/\lambda = 5\%$ ), confirming a tendency for floating objects diverging from purely Lagrangian tracers to travel at a drift speed linearly correlated to the offshore wave steepness in the nearshore environment.

A shift towards a linear relation was also observed by Lenain et al. (2019). Their experiments were conducted with objects considered by the authors to be good Lagrangian tracers transported by a deep-water breaking surface wave packet. The study revealed a sharp transition from a quadratic dependence of the drift speed on steepness below the breaking threshold to a linear dependence above the breaking threshold for deep-water conditions. This interestingly shows how, even for objects assumed to be Lagrangian tracers, a switch to a linear relation between drift speed and steepness can be observed when breaking is considered. This further supports the interpretation that the observed trend in the present study could be better captured by a linear relationship, given that the current experimental conditions consistently encompass wave breaking. Similar conclusions were made by Eeltink et al. (2023) whose experiments were conducted under irregular waves. In this case, the switch between quadratic and linear dependency was not as recognisable given the irregular nature of breaking under the tested conditions. The drift speed was therefore observed to increase continuously with wave steepness, without a clear shift between regimes.

Alsina et al. (2020) provided experimental proof of the quadratic relation between the measured net drift of the floating particles and the wave steepness, in good agreement with the classical Stokes theory. This disagreement with the previous studies and with the presented hypothesis of linear fit for the current research is to be attributed to the differences in experimental conditions. Alsina et al. (2020), in fact, considered the dynamics in intermediate water depth, similarly to the current study, but excluding breaking, therefore capturing a quadratic relation, in agreement with what Lenain et al. (2019) observed below the breaking threshold, which is assumed not to be applicable when breaking is considered.

## 5.2. Evolution of MPD Horizontal Transport

In order to further understand the evolution of plastic particles behaviour, the horizontal drift speed was spatially assessed along the flume and averaged over 0.2 metres intervals. This allowed for the observation of recurrent patterns in particles speed, which presented an accelerating phase during the shoaling zone, culminating with a peak speed at breaking, which gradually decreased following energy dissipation across the surf zone. The magnitude of the peaks in horizontal drift speed was most pronounced at the breaking zone, suggesting its relevance in the description of marine plastic debris motion in the nearshore environment. The spatial determination of the particles speed allowed for assessing its dependency on the offshore steepness across the different identified transport domains, the shoaling, the breaking and the surf zones. It was observed how the relationship between particles horizontal drift speed and offshore steepness remained positive considering the spatial discretisation into zones, and was mostly accentuated in the breaking zone. The coefficients of determination of the linear and quadratic fits don't allow for conclusive statements on the functional form of the relationship; nonetheless, no strong curvature is identified in the quadratic fit, which aligns closely with its linear counterpart across all the zones.

The presence of the sloped bottom strongly influenced the evolution of the shape of the waves. The different generated wave conditions, characterised by increasing offshore steepness, resulted in different behaviours when propagating along the flume. The main important point to notice is how the breaking point location differed across the seven tested wave conditions. This is because waves with greater initial wave heights will reach the depth-induced breaking threshold earlier than waves with lower wave heights. Such behaviour is most common in coastal natural environments where the water depth gradually decreases in the onshore direction. This resulted in different breaking locations for every wave condition, with steeper waves reaching the breaking criteria earlier onshore compared to less steep ones. Therefore, the particle drift speed was compared to the actual local steepness in the three analysed zones, in addition to the comparison with offshore steepness.

The clear positive relation between particle drift speed and steepness is maintained when consid-

ering the local steepness in the shoaling and breaking zones. This does not apply to the surf zone where the relation between particle horizontal drift and local steepness breaks down, causing local steepness to lose its validity as a predictor for particle drift speed. This was expected, as the classical definitions of wave steepness lose validity after breaking, where the flow transitions to highly non-linear dynamics, with bores, rollers, and rapid energy dissipation dominating the dynamics. In this regime, the shape of the waves becomes irregular and transient, making it difficult to define consistent wave height and wave number and thus meaningful steepness values. In addition, by the moment the particles enter the surf zone, waves have already undergone breaking, dissipating most of their energy. As a result, the transport in this region may be more influenced by residual momentum than local wave characteristics. Offshore steepness, however, was proved to effectively relate to MPD transport, as it consistently captured the dominant trends in particle drift speed across the different zones. This is particularly relevant as for natural environments, where local wave dynamics in the surf zone are complex, variable and difficult to measure directly, offshore steepness could be used to effectively describe MPD transport.

### 5.3. MPD Horizontal Drift Speed and Wave Propagation Speed Estimates

The horizontal drift speed of MPD was compared to wave propagation speed metrics relevant to the tested wave conditions to assess whether their motion could be effectively described using these parameters. The evolution of the phase speed, crest speed and Stokes drift was computed along the relevant flume regions. It was observed how the non-linear behaviour of the generated waves travelling over the sloped bottom was dominant for all the wave steepness scenarios. Therefore, the estimates of the phase speed according to the linear wave theory consistently underestimated the expected actual phase speed. A correction to account for non-linearities was applied, which resulted in higher phase speed values. It was observed how the estimated crest speed values fell between the linear and non-linear approximations of phase speed across all the tested wave conditions, the range between the two estimates for the phase speed was therefore considered a valid representation of the magnitude of both phase and crest speed. Together with the estimate of the Stokes drift, the characterisation of the wave field was considered complete.

The particle drift speed fell between the phase-crest speed range and the Stokes drift estimates for all the tested offshore steepness conditions, exhibiting a closer adherence to Stokes drift for the lowest wave steepness scenario ( $\epsilon = 0.056$ ) and progressively diverging from it until reaching the highest deviation for the steepest condition ( $\epsilon = 0.256$ ). These results suggest that particles do not perfectly follow either of the computed wave velocity estimates and find agreement with previous studies, which argued how the classical Stokes drift theory could fail in effectively representing the transport velocity of free-floating objects. Huang et al. (2013) concluded that for larger objects, drift velocities are significantly higher than the Stokes drift. Similarly, Xiao et al. (2025) confirmed that, for objects with a relative size greater than 3% ( $l/\lambda$ ), the particle drift speed significantly diverged from the Stokes drift predictions, showing greater resulting transport.

The deviation from the Stokes drift estimate was especially recognisable around the breaking zone. Even the particles undergoing the least energetic wave conditions, which showed close alignment to the Stokes drift overall, presented a significant deviation at breaking. Their horizontal drift speeds doubled the values predicted by the classical Stokes theory, increasing up to four times that prediction for the most extreme steepness condition. This, together with the previous observation on the evolution of particle drift speed, further supports the relevance of the breaking zone for the description of the nearshore MPD transport.

The behaviour of the objects around breaking was therefore further investigated by relating their horizontal drift speed to the local wave steepness measured in order to capture the actual hydrodynamic conditions driving the drift in that zone. Compared to local steepness, the particle horizontal drift speed consistently increased, falling between the lower boundary represented by the Stokes drift estimate and the upper boundary being the wave crest speed, across all the tested conditions. A progressive transition towards the upper boundary was observed as local steepness increased,

nonetheless, the drift values never reached more than 40% of the crest speed, indicating how the tested objects did not tend to surf on the wave throughout the breaking zone but were accelerated by the breaking in a progressively stronger manner as local steepness increased. This observation is highly influenced by the type of particle selected for the current study. Research conducted by Swuste (2025) showed how for an intermediate offshore wave steepness condition ( $\epsilon = 0.122$ ) particles characterised by lower density values ( $\rho_o/\rho_w = 0.09 - 0.23$ ) reached horizontal drift speed values close to the crest speed at breaking. This suggests that the limited drift response observed in the present study is at least partly attributable to the higher density of the tested particles, which reduced their ability to follow the rapid crest motion during breaking.

The role of wave breaking in enhancing the transport of floating objects has been previously investigated in deep-water conditions by Deike et al. (2017), Lenain et al. (2019), and Eeltink et al. (2023). The present study builds on these findings by extending the analysis to nearshore environments, where wave transformation occurs over a sloped bottom and the flow transitions from intermediate to shallow regimes. Despite the differences in hydrodynamic conditions and experimental settings, the results of this study show qualitative agreement with previous work, suggesting the broader applicability of the observed trends.

The mentioned studies consistently found that breaking increases particles drift speed and that this enhancement scales with wave steepness. Calvert et al. (2024) concluded that in deep-water conditions, steep, breaking waves are associated with a drift which is greater than the Stokes drift. This added drift was similarly observed by Deike et al. (2017) and Lenain et al. (2019), which affirmed how, for focusing wave packets that lead to breaking, the observed drift can be up to ten times larger than the classical Stokes drift for a non-breaking packet at the surface.

Finally, Eeltink et al. (2023) confirmed the enhancement of the transport caused by breaking under the influence of deep-water irregular waves. The Authors in this study provided an approximate comparison of the scaling of particle drift speed at breaking with steepness with the research conducted by Deike et al. (2017) and Lenain et al. (2019). The results of the comparison presented by Eeltink et al. (2023) show that the slope of the linear fit between the normalised particle drift speed (with respect to crest speed) and wave steepness is comparable across the studies, yielding slope values of respectively  $\alpha = 2.02$  and  $\alpha = 4.03 - 6.03$ . It is important to notice that direct comparison is limited by several factors. Both authors investigate the behaviour in deep-water conditions, with Eeltink et al. (2023) referring to irregular waves, whereas Deike et al. (2017) and Lenain et al. (2019) to a single focused wave group, both using Lagrangian tracers.

Considering the differences in experimental conditions between the referenced studies and the present one, and recognising the limited reliability of the linear fit obtained here, the slope of the currently hypothesized linear fit between crest-normalised particle drift and wave steepness is found to be 1.8, in good agreement with the values reported in the deep-water studies. This suggests that, despite differences in wave type, flow regime, and particle characteristics, the enhancement of particle drift with increasing wave steepness observed in deep-water conditions may also apply to shallow-water breaking. This mechanism is particularly relevant for the natural nearshore environment where wave breaking is a dominant process and is expected to result in a substantial increase of MPD onshore transport.

## 5.4. Limitations and Assumptions

The main limitations and assumptions behind this study are presented in this section and should be taken into consideration when interpreting the results and discussion arguments. First, the uncertainty behind the hydrodynamic conditions will be presented, followed by the limitations of the performance of the tracking process. Limitations behind the use of SWASH as a modelling tool for representing the experimental conditions will be presented. Further limitations in the experimental setup itself will be lastly addressed.

The generation of waves within a laboratory flume is commonly considered a potential source of uncertainty. In this study, by deploying measurement instruments within the flume, it was possible to

measure the accuracy of the generated conditions compared to the programmed ones, along with their consistency over time. Good agreement was found between the target wave heights and the observed ones close to the wave paddle over a test period of 30 minutes. This confirmed that the generated conditions closely followed the intended ones and remained stable over time, validating the assumption of reliable wave generation for the purposes of the study.

SWASH simulations of the experimental conditions were run in order to be able to get continuous estimates of the wave characteristics along the whole flume. The results of the simulations were validated against the available data obtained from the wave gauges installed in six locations within the flume. The outcomes of the validation showed good agreement between the observed and modelled hydrodynamic conditions up until the breaking zone. After the breaking zone, the results of the simulations started to progressively deviate from the measured data. This deviation has to be attributed to two main causes. First, SWASH models are known to be limited in the capturing of post-breaking dynamics (Stelling et al. 2009). In addition, the mismatch of the model with measured data is extreme for the measurement instrument positioned at Location 6, far onshore on the slope. The data retrieved from this instrument is considered less reliable, as the sensor was only barely submerged due to the low water level. According to the conducted validation, the uncertainty behind the use of the model was limited by only using its results for comparison with the measured particle drift for the shoaling, breaking and early surf zone, where the model was considered robust and reliable.

Limitations in the quality of the particle trajectory data are to be linked to the tracking process. The detection and tracking of particles were performed using the YOLOv5 model developed by Ultralytics (Jocher 2020). Its performance was variable and was mainly limited by setup-specific factors, which could be easily prevented in the case of new experiments. Specifically, tracking limitations were caused by visual interference, particle clustering, lightning issues and particles disappearing from view during wave breaking. Details on the encountered issues and the performance of the trained detection model are provided in Appendix E. These observations on the limitations of the setup should be considered when applying a similar methodology.

While the laboratory environment allows for reproducible, controlled experiments and therefore for the investigation of the role of one isolated variable, it presents main limitations in linking the observed behaviours to real-world processes and environments. First, the constraint of the flow in a wave generation tank causes additional effects to arise, which can be attributed to different factors such as friction with the side walls, vorticity caused by the wave generation, wave reflection, recirculation and setup-specific hydrodynamic behaviours. More specifically, in wave flume experiments, wave-induced Eulerian-mean flows are known to interfere with the observation of Stokes drift, as their behaviour is often unpredictable and sensitive to boundary conditions (Van den Bremer et al. 2017; Monismith 2020). In a closed tank the Stokes drift of a periodic wave train is expected to be accompanied by an Eulerian return flow which allows for the steady-state depth-integrated Lagrangian drift to be zero (Alsina et al. 2020). Return currents also occur in natural coastal environments, however, they are generally weaker and more variable than in flumes, where confined geometry and the presence of boundaries tend to increase their intensity. Such flow behaviours were observed in the current experimental setup and are further elaborated in Section B.3.

The return flow was quantified for the current experimental setup by integrating the Stokes drift vertical profile and redistributing the resulting transport uniformly along the water depth. This allowed for a preliminary estimate of the contribution of the potential return current, which was assessed to be around 40% of the superficial Stokes drift measured at the toe of the slope; its contribution progressively increased up to 100% in the onshore direction as the water depth decreased. Nonetheless, particles onshore horizontal transport was observed up until the end of the slope, where the contribution of the return current was expected to balance out the net forward motion caused by the Stokes drift. It is therefore hypothesised that the forward drift characterising the final stages of the particles trajectories might have been driven by other contributing processes which remain to be identified but may include residual effects of wave-induced transport or more dominant near-bed dynamics. The presence of a setup-driven return current is acknowledged here; however, more precise estimates of this and other flume-driven processes are necessary to consider their influence on the measured

particle transport.

When conducting experiments in laboratory environments, challenges related to dimensional scaling are almost inevitable (Forsberg et al. 2020). The main difficulties in this context refer to the scaling of the viscous and inertial forces, which respectively govern the resistance experienced by particles due to fluid friction and their response to acceleration, both of which influence particle motion under wave forcing. These effects are typically characterised using nondimensional numbers such as the Reynolds number, which is a measure of the relative importance of the effects of viscous drag and fluid inertia on the particle, and the Stokes number, which is a measure of particle inertia relative to the background flow (Sutherland et al. 2023). These nondimensional values are specific to the laboratory setup and cannot be directly scaled to natural coastal conditions. In order to be able to reliably relate laboratory findings to natural processes, adequate dynamic scaling must be performed to preserve the balance between dominant forces. While it is acknowledged that dimensional scaling would be desirable to allow for direct translation of laboratory-based results to the real-world environment, the current research did not include formal scaling considerations. Despite the setup-specific limitations, this study still represents a solid foundation on the isolated influence of offshore steepness on the nearshore plastic transport.

A physical limitation of the flume is the presence of the glass walls, which interacted with the particle motion mainly towards the end of their trajectories at the end of the surf zone and in the swash zone. This is a common issue for flume-based experiments. In the context of this research, the analysis was focused on the shoaling, breaking and early surf zones, where, while the interaction was present, it was not as substantial as later onshore in the flume.

Particles were consistently released in the middle of the flume (in y-direction), this was done with the goal of minimising their interaction with the flume glass walls. While travelling in the flume, some of the particles came in contact with its boundaries. Such trajectories were not excluded from the analysis to maintain its statistical significance. The side wall interaction was quantitatively assessed but not considered in this research; nonetheless is expected to have influenced the measured trajectories. Considering the spatial domain from the particle release point in the shoaling zone up until data was available (after around 3-5 metres depending on the wave condition) the share of trajectories interacting with the wall was assessed. This was done by counting the number of particles detected at least once within 0.05 metres of the flume boundaries in each 0.5-metres spatial bin in the x-direction of the flume. This was observed to be very low ( $< 10\%$ ) for the first three metres from the release point, the percentage of interfering particles increased to around 35% at 4.5 - 5.5 metres from the release point. No trend in interfering behaviour was observed based on the analysed offshore steepness conditions. The interference was visually observed to increase further along the flume as particles travelled towards the end of the surf zone and in the swash zone. This increase in interaction can be attributed to the decrease in particle horizontal drift speed towards the end of the flume, which made particles more likely to drift laterally (in the y-direction) and come in contact with the flume boundaries. This suggests limited side-wall interactions in the zones considered in the current study, supporting the reliability of the computed particles horizontal drift speed.

In addition, in the final onshore section of the flume, asymmetry in the wave arriving front was observed and was progressively accentuated as the offshore wave steepness increased. This asymmetry was observed to be interchangeably drawn to one side of the flume or the other across different experimental runs preventing the observation of any recurrent biases. Nonetheless, it was observed to cause an increase in particles transport towards the glass walls. The analysis within this research was limited to the shoaling, breaking and beginning of the surf zone where the asymmetry in the wave front remained very limited and was not expected to compromise the reliability of the results, supporting the validity of the conclusions drawn within the considered spatial domain.

In order to limit the interaction with the flume boundaries and allow for observations of particle motion along the cross sectional direction, experiments should be carried out at a scale as large as possible (Calvert et al. 2024). Additionally, large scale experiments are to be preferred in order to limit the dependency of the mechanisms driving particles drift on the drag the waves exert on the objects and thus on Reynolds and Stokes numbers (Ross Calvert et al. 2021; Sutherland et al. 2023).



A further consideration specific to the setup was the necessity of using fresh water in the flume, driven by practical limitations. This is expected to have limited influence on the specific tested conditions. A change in salinity and, therefore density ratio between the particles and the surrounding water would have still resulted in the particles used in this study floating on the water. In addition, their behaviour could be extrapolated in the natural environment by estimating the settling or buoyancy rate in saline fluids (Núñez et al. 2023).

Finally, reproducing realistic breaking dynamics remains a challenge within the current experimental setup. The waves generated in the flume started breaking as they approached the depth-induced breaking limit. In natural ocean conditions, however, additional factors such as wind-driven friction velocity and underlying currents contribute to wave breaking. Contributing to the differences, this study refers to unidirectional regular waves while natural wave fields are characterised by strong irregularities and directional spread. The main mechanisms linking particle drift speed to wave steepness are nonetheless identified, and their clear identification is facilitated by the great simplification of the dynamics. This allows for a better understanding of the basic processes, offering a valid basis for relating breaking to MPD transport in more complex natural environments.

Despite the discussed limitations and assumptions, the conducted controlled laboratory environment, together with a strict data validation procedure, provides a solid methodology for isolating the role of offshore wave steepness in nearshore plastic transport. The identified sources of uncertainty primarily contribute to the spread in the collected trajectory data. This was limited by only considering reliable measurements in the analysis and by clearly providing estimates of the uncertainty when presenting the results. Additionally, the study was intentionally focused on spatial zones where the influence of setup-specific effects was minimised.

## 5.5. Further Research

The current study explores the horizontal transport dynamics of identical spheres under the influence of progressively steeper regular breaking waves in a flume environment. The presented results aim to improve the understanding of the complex and non-linear transport of plastic in coastal environments, a process that remains poorly understood and has been widely recognised as needing further experimental investigation (Alsina et al. 2020; Núñez et al. 2023; Van Sebille et al. 2020). While the current methodology allowed for the observation of interesting patterns, additions and refinements could be applied to complete and improve the relevance of the findings.

Experiments were conducted generating regular waves within the flume. While this represents a valid method to observe transport behaviours, experiments with irregular and directionally spread waves based on realistic spectra should be carried out in future work. This would help link the observations on the influence of offshore steepness to actual irregular dynamics, validating the current results in more realistic wave fields. Núñez et al. (2023) conducted laboratory flume experiments generating both regular and irregular wave conditions. They concluded that the final cross-shore distribution of plastic debris may remain similar between regular and irregular sea states. However, the MPD transport mechanisms are likely to differ due to the varying energy distribution of irregular waves. It is therefore hypothesised that the general positive trend of increased particle drift speed with increasing offshore steepness will continue to hold considering irregular waves. Nonetheless, a broader spread of drift speeds and more complex transport pathways are expected due to the influence of temporal and spatial variability and the formation of transient wave groups.

The observed positive dependence of particle horizontal drift speed to offshore steepness suggested this parameter as useful predictor for describing plastic transport in the nearshore environment. Nonetheless, the functional relationship between the two variables was not conclusively captured within this study. Existing research supports the hypothesis that a linear relation better describes the observed trend, especially given the current experimental conditions of shallow breaking waves and the observed significant particles deviation from purely Lagrangian behaviour. The difficulties in identifying the nature of the positive relationship may be attributed to the level of variability in the results, which prevented a confident conclusion regarding a clear linear or quadratic scaling. Improving the sample size of the final analysed particle trajectories is considered to be a valid solution

to improve the robustness of the fit and allow for confident conclusions on its nature. An improvement on this side could be done in the processing phase, where a significant number of particle trajectories were lost. The material produced by the current experimental campaign could represent the starting point for applying more refined tracking and eventually shed light on the functional relation of offshore steepness to particle drift speed in the nearshore region.

Additionally, past studies conducted in deep-water conditions, under breaking and non-breaking waves suggested that the type of relation between steepness and particle drift is strongly influenced by the relative size of the travelling objects and by the presence of breaking. The conclusions drawn by the mentioned Authors should be extended to shallow-water nearshore environments by repeating the current study to account for MPD with variable relative size and assess the validity of the size-dependency.

The current study limited its scope to the horizontal onshore travel behaviour of MPD. Recent experimental efforts have started to focus on the role of land-based input of plastic material in coastal environments (Núñez et al. 2023). However, the role of plastic retention and resuspension remains underexplored in laboratory experiments (Van Sebille et al. 2020). The presented study provides a solid foundation for further advancing understanding in this context. In the current experiments, particle beaching was defined as stabilisation on the slope; when beaching was observed, particles would be removed from the flume. In reality, particles might reach the beach, stabilise and be picked up again by new incoming waves. Running long-duration experiments to observe multiple beaching-resuspension cycles and quantifying retention probabilities would represent a relatively simple but insightful extension of the current study. In addition, the sloped bottom used to simulate the beach environment was intentionally kept simple to be able to isolate offshore steepness as an investigation variable, this could be extended in future work. The influence of different beach types in terms of angle, direction and roughness could add to the current study to provide a more comprehensive understanding of how coastal morphology interacts with wave steepness to affect the transport and retention of MPD.

Finally, considering the previously discussed challenges associated with laboratory flume experiments, future research would benefit from complementary fieldwork campaigns. Conducting experiments in natural nearshore environments would allow for the validation of the findings of the current study under real-world conditions, where particle variability and realistic wave dynamics come into play, therefore strengthening the relevance of the current study.

Recent field work on marine plastic debris beaching was conducted by Haagsma (2025). The results highlighted the complexity of conducting research in the field where multiple environmental factors, such as wind speed, wind direction, tidal influence and wave action simultaneously influence the nearshore plastic transport. Among these, waves were recognised as one of the main contributors. Combining the results of the current study on wave steepness with field-based observations can be particularly valuable. While the former enables the isolation of a specific variable, providing initial conclusions on its influence, the latter captures the full complexity of natural systems, offering a more comprehensive understanding of nearshore plastic transport processes.

---

**Legend:** ■ 100% overlap ■ 90% overlap with minimal adjustments ■ 0% overlap

---





# 6

## Conclusion

The current study focused on the investigation of the influence of offshore steepness on the nearshore transport of marine plastic debris. This was accomplished by conducting laboratory experiments, which involved the generation of regular breaking waves characterised by varying offshore steepness values propagating over a sloped bathymetry. The analysed body of literature highlighted the need for experimental work on shallow-water breaking waves in the nearshore environment. The current study is positioned in that gap and investigates the role of offshore wave steepness as a research variable.

An overall positive relationship was observed between offshore wave steepness and particle horizontal drift speed. The consistent increase of particles horizontal drift speed with offshore steepness confirmed its potential as a classification metric. While it does not account for local dynamics directly, offshore steepness captures the intensity of transport and can be considered a valid predictor for marine plastic debris behaviour in the nearshore environment.

The particle horizontal drift speed was observed to follow a common evolution throughout their trajectory along the flume, with a clear peak occurring as waves transitioned from shoaling to breaking. The sharp increase and subsequent drop in particle speed around the breaking point highlighted its controlling role in both the magnitude and variability of particle horizontal drift speed.

The results showed that offshore steepness translates well into local steepness in the shoaling and breaking zones, suggesting that offshore steepness can represent the local wave conditions driving transport in these regions. In such spatial domains, both parameters are positively correlated with particle horizontal drift speed. However, in the surf zone, local steepness progressively loses its meaning as the flow becomes dominated by bores and a clear wave shape is no longer recognisable. As a result, it becomes an unsuitable metric for describing particle drift speed after breaking. Offshore steepness, however, was proved to effectively relate to marine plastic debris transport also for the surf zone, where it consistently captured the dominant trends in particle horizontal drift speed.

The functional nature of the identified relationship between offshore wave steepness and particle horizontal drift was investigated. While the experimental results combined with existing literature suggest a likely linear trend, the data did not allow for a definitive conclusion.

Finally, particle drift speeds were compared to Stokes drift and crest speed as characteristic metrics describing wave-induced transport. The results showed that particle horizontal drift speed consistently fell between the estimates for the Stokes drift and crest speed across all the tested wave conditions. Stokes drift was observed to underestimate particle drift speed, which, nonetheless, never reached speed values as high as the wave crest speed. The greatest deviation from the Stokes drift was observed near the breaking zone for all the tested conditions. Additionally, the deviation from the Stokes drift at breaking progressively increased as local wave steepness increased. This result extends the observations of the role of wave breaking in enhancing marine plastic debris transport

in deep-water conditions to the nearshore environment.

The current study was conducted in parallel with the work of Swuste (2025), focused on assessing the influence of particle density on marine plastic debris horizontal transport. The results demonstrated how horizontal drift and beaching dynamics of marine plastic debris are dependent on particle density. Overall, a negative relationship was observed between particles density and horizontal drift speed, as higher-density particles took significantly longer to reach the beach compared to lower-density particles (Swuste 2025). Combining the outcomes of the current and the mentioned study, it can be concluded that both wave conditions and particles properties are important parameters to be considered when describing marine plastic debris nearshore transport.

To build upon the findings of this study, several directions for future work are presented. Experiments using irregular and directionally spread waves based on realistic sea state spectra should be conducted. Future studies should also explore the influence of more complex beach morphologies, including variations in slope, orientation, and roughness, to better represent natural coastal environments. The proposed improvement of the setup should be complemented by the consideration of dimensional scaling challenges, either through larger flume facilities or by quantifying the scaling effects. This would allow to more confidently relate laboratory findings to the field.

Finally, the combination of controlled laboratory studies with targeted field observations would be valuable for validating and expanding the current experimental results. Parallel to the current study, Haagsma (2025) presented field-based observations of marine plastic debris nearshore dynamics considering the effects of waves, wind, tides and plastic density. The study highlighted the complex interactions of such environmental factors. Wave action was shown to be an important contributor, though not the only driver of the observed marine plastic debris transport dynamics. Field-based observations would therefore complement the current findings by capturing the dynamics of real coastal settings, thereby supporting laboratory-based conclusions and contributing to the development of more accurate and comprehensive parameterisations of nearshore marine plastic debris transport.

---

**Legend:**  100% overlap  90% overlap with minimal adjustments  0% overlap

---

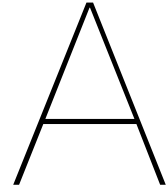
# Bibliography

- Alsina, José M, Cleo E Jongedijk, and Erik van Sebille (2020). "Laboratory measurements of the wave-induced motion of plastic particles: Influence of wave period, plastic size and plastic density". In: *Journal of Geophysical Research: Oceans* 125.12, e2020JC016294.
- Booij, Nico (1981). "Gravity waves on water with non-uniform depth and current". In: *Ph. D. Thesis*.
- Calvert, R, A Peytavin, Y Pham, A Duhamel, J van der Zanden, SM van Essen, B Sainte-Rose, and TS van den Bremer (2024). "A laboratory study of the effects of size, density, and shape on the wave-induced transport of floating marine litter". In: *Journal of Geophysical Research: Oceans* 129.7, e2023JC020661.
- Calvert, Ross, ML McAllister, C Whittaker, Alison Raby, AGL Borthwick, and TS Van Den Bremer (2021). "A mechanism for the increased wave-induced drift of floating marine litter". In: *Journal of Fluid Mechanics* 915, A73.
- Compa, Montserrat, Carme Alomar, Chris Wilcox, Erik van Sebille, Laurent Lebreton, Britta Denise Hardesty, and Salud Deudero (2019). "Risk assessment of plastic pollution on marine diversity in the Mediterranean Sea". In: *Science of the Total Environment* 678, pp. 188–196.
- Cunningham, HJ, C Higgins, and TS van den Bremer (2022). "The role of the unsteady surface wave-driven Ekman–Stokes flow in the accumulation of floating marine litter". In: *Journal of Geophysical Research: Oceans* 127.6, e2021JC018106.
- Deike, Luc, Nick Pizzo, and W Kendall Melville (2017). "Lagrangian transport by breaking surface waves". In: *Journal of Fluid Mechanics* 829, pp. 364–391.
- Eeltink, Debbie, R Calvert, JE Swagemakers, Qian Xiao, and TS van den Bremer (2023). "Stochastic particle transport by deep-water irregular breaking waves". In: *Journal of Fluid Mechanics* 971, A38.
- Fenton, John D. (1988). "The numerical solution of steady water wave problems". In: *Computers & Geosciences* 14.3, pp. 357–368.
- Forsberg, Pernille Louise, Damien Sous, Alessandro Stocchino, and Remi Chemin (2020). "Behaviour of plastic litter in nearshore waters: First insights from wind and wave laboratory experiments". In: *Marine pollution bulletin* 153, p. 111023.
- Geyer, Roland, Jenna R Jambeck, and Kara Lavender Law (2017). "Production, use, and fate of all plastics ever made". In: *Science advances* 3.7, e1700782.
- Haagsma, I. E. (2025). "Investigating the Beaching Dynamics of Plastic in the Nearshore Region: a Fieldwork Study". Master's thesis in preparation.
- Hale, Robert C., Mary E. Seeley, Aimee B. Lindstrom, and Mark J. Strynar (2020). "A Global Perspective on Microplastics". In: *Journal of Geophysical Research: Oceans* 125.9, e2020JC016933.
- He, Ming, Bing Ren, and Da-hong Qiu (2016). "Experimental study of nonlinear behaviors of a free-floating body in waves". In: *China Ocean Engineering* 30.3, pp. 421–430.
- Hedges, Terry S (1976). "An empirical modification to linear wave theory." In: *Proceedings of the Institution of Civil Engineers* 61.3, pp. 575–579.
- Higgins, Christopher, Jacques Vanneste, and TS van den Bremer (2020). "Unsteady Ekman-Stokes dynamics: Implications for surface wave-induced drift of floating marine litter". In: *Geophysical Research Letters* 47.18, e2020GL089189.
- Holthuijsen, Leo H. (2007). *Waves in Oceanic and Coastal Waters*. Cambridge, UNITED KINGDOM: Cambridge University Press. ISBN: 978-0-511-26845-8. (Visited on 01/02/2025).

- Huang, Guoxing, Adrian Wing-Keung Law, and Zhenhua Huang (2011). "Wave-induced drift of small floating objects in regular waves". In: *Ocean Engineering* 38.4, pp. 712–718.
- Huang, Guoxing and Adrian WK Law (2013). "Wave-induced drift of large floating objects in regular waves". In: *Journal of waterway, port, coastal, and ocean engineering* 139.6, pp. 535–542.
- Jalón-Rojas, Isabel, Xiao Hua Wang, and Erick Fredj (2019). "A 3D numerical model to Track Marine Plastic Debris (TrackMPD): Sensitivity of microplastic trajectories and fates to particle dynamical properties and physical processes". In: *Marine pollution bulletin* 141, pp. 256–272.
- Jocher, Glenn (2020). *Ultralytics YOLOv5*. Version 7.0. DOI: 10.5281/zenodo.3908559. URL: <https://github.com/ultralytics/yolov5>.
- Lenain, Luc, Nick Pizzo, and W Kendall Melville (2019). "Laboratory studies of Lagrangian transport by breaking surface waves". In: *Journal of Fluid Mechanics* 876, R1.
- Li, Huichao, Xi Feng, Xingye Ni, and Weibing Feng (2023). "Beaching process of floating marine debris associated with the evolution of the nearshore wave". In: *Marine Pollution Bulletin* 197, p. 115695.
- Lo, Hoi-Shing, Yan-Kin Lee, Beverly Hoi-Ki Po, Leung-Chun Wong, Xiaoyu Xu, Cheuk-Fung Wong, Chun-Yuen Wong, Nora Fung-Yee Tam, and Siu-Gin Cheung (2020). "Impacts of Typhoon Mangkhut in 2018 on the deposition of marine debris and microplastics on beaches in Hong Kong". In: *Science of the Total Environment* 716, p. 137172.
- Löhr, Ansje, Heidi Savelli, Raoul Beunen, Marco Kalz, Ad Ragas, and Frank Van Belleghem (2017). "Solutions for global marine litter pollution". In: *Current opinion in environmental sustainability* 28, pp. 90–99.
- Martins, Kévin, Philippe Bonneton, and Hervé Michallet (2021). "Dispersive characteristics of non-linear waves propagating and breaking over a mildly sloping laboratory beach". In: *Coastal Engineering* 168, p. 103925.
- McClenaghan, Elliot (2024). *Mann-Whitney U Test: Assumptions and Example*. <https://www.technologynetworks.com/informatics/articles/mann-whitney-u-test-assumptions-and-example-363425>. Accessed: 2025-05-07.
- Monismith, Stephen G (2020). "Stokes drift: theory and experiments". In: *Journal of Fluid Mechanics* 884, F1.
- Myrhaug, Dag and Søren Peter Kjeldsen (1986). "Steepness and asymmetry of extreme waves and the highest waves in deep water". In: *Ocean Engineering* 13.6, pp. 549–568. DOI: 10.1016/0029-8018(86)90039-9.
- Núñez, Paula, Alessandro Romano, Javier García-Alba, Giovanni Besio, and Raúl Medina (2023). "Wave-induced cross-shore distribution of different densities, shapes, and sizes of plastic debris in coastal environments: A laboratory experiment". In: *Marine Pollution Bulletin* 187, p. 114561.
- Onink, Victor, Cleo E Jongedijk, Matthew J Hoffman, Erik van Sebille, and Charlotte Laufkötter (2021). "Global simulations of marine plastic transport show plastic trapping in coastal zones". In: *Environmental Research Letters* 16.6, p. 064053.
- Pawlowicz, R (2021). "The grounding of floating objects in a marginal sea". In: *Journal of Physical Oceanography* 51.2, pp. 537–551.
- Plus, Machine Learning (2023). *Augmented Dickey-Fuller Test in Python: Complete Guide*. Accessed: 2025-05-18. URL: <https://www.machinelearningplus.com/time-series/augmented-dickey-fuller-test/>.
- Poulain-Zarcos, Marie, Nimish Pujara, Gautier Verhille, and Matthieu J Mercier (2024). "Laboratory experiments related to marine plastic pollution: a review of past work and future directions". In: *Comptes Rendus. Physique* 25.S3, pp. 1–32.
- Soulsby, Richard (1997). "Dynamics of marine sands". In:

- StatsKingdom (2024). *Shapiro-Wilk test with tables*. Accessed: 2025-05-01. URL: [https://www.statskingdom.com/doc\\_shapiro\\_wilk.html](https://www.statskingdom.com/doc_shapiro_wilk.html).
- Stelling, GS and M Zijlema (2009). "Numerical modeling of wave propagation, breaking and run-up on a beach". In: *Advanced computational methods in science and engineering*. Springer, pp. 373–401.
- Sutherland, Bruce R, Michelle DiBenedetto, Alexis Kaminski, and Ton Van Den Bremer (2023). "Fluid dynamics challenges in predicting plastic pollution transport in the ocean: A perspective". In: *Physical Review Fluids* 8.7, p. 070701.
- Swuste, L. M. J. (2025). "Density-Driven Effects on Marine Plastic Beaching: Observations from Laboratory Flume Experiments". Master's thesis in preparation.
- Tanizawa, Katsuji, Makiko Minami, and Yasuji Imoto (2001). "On the drifting speed of floating bodies in waves". In: *Journal of the Society of Naval Architects of Japan* 2001.190, pp. 151–160.
- Team, SWASH Development (2025). *SWASH User Manual*. Accessed May 5, 2025. URL: [https://swash.sourceforge.io/online\\_doc/swashuse/swashuse.html%5C#file-swashedt](https://swash.sourceforge.io/online_doc/swashuse/swashuse.html%5C#file-swashedt).
- Tissier, M., P. Bonneton, R. Almar, B. Castelle, N. Bonneton, and A. Nahon (2011). "Field measurements and non-linear prediction of wave celerity in the surf zone". In: *Coastal Engineering* 58.7, pp. 701–712. DOI: 10.1016/j.coastaleng.2011.03.003.
- TU Delft Faculty of Civil Engineering and Geosciences (n.d.). *Indoor Lab Facilities – Hydraulic Engineering Laboratory*. <https://www.tudelft.nl/citg/over-faculteit/afdelingen/hydraulic-engineering/sections/hydraulic-engineering-laboratory/indoor-lab-facilities>. Accessed: 2025-04-13.
- Van den Bremer, Ton S and Øyvind Breivik (2017). "Stokes drift". In: *Philosophical transactions of the royal society a: mathematical, physical and engineering sciences* 376.2111, p. 20170104.
- Van der Zanden, Joep (2016). "Sand transport processes in the surf and swash zones". In:
- Van Sebille, Erik, Stefano Aliani, Kara Lavender Law, Nikolai Maximenko, José M Alsina, Andrei Bagaev, Melanie Bergmann, Bertrand Chapron, Irina Chubarenko, Andrés Cózar, et al. (2020). "The physical oceanography of the transport of floating marine debris". In: *Environmental Research Letters* 15.2, p. 023003.
- Villarrubia-Gómez, Patricia, Sarah E Cornell, and Joan Fabres (2018). "Marine plastic pollution as a planetary boundary threat–The drifting piece in the sustainability puzzle". In: *Marine policy* 96, pp. 213–220.
- Wikipedia contributors (2024). *Kruskal–Wallis test — Wikipedia, The Free Encyclopedia*. Accessed: 2025-05-07. URL: [https://en.wikipedia.org/wiki/Kruskal%E2%80%93Wallis\\_test](https://en.wikipedia.org/wiki/Kruskal%E2%80%93Wallis_test).
- Williams, AT and DT Tudor (2001). "Litter burial and exhumation: spatial and temporal distribution on a cobble pocket beach". In: *Marine Pollution Bulletin* 42.11, pp. 1031–1039.
- Xiao, Q, ML McAllister, TAA Adcock, and TS van den Bremer (2025). "Laboratory study of the enhanced wave-induced drift of large rectangular floating objects". In: *Journal of Fluid Mechanics* 1008, A18.





# Camera Calibration and Distance Conversion

To translate the observed movement of particles in the video recordings into real-world trajectories within the flume, camera calibration was required. The camera calibration procedure considered in this study consisted of two components: The correction of lens-induced image distortion, and relating camera pixel-distances to real-world distances.

## A.1. Camera Distortion

Camera distortion is the geometric warping of images caused by the camera lens, resulting in curved lines or altered shapes, especially at the edges of wide-angle images. In the original recordings used in this research, distortion appeared minimal. The bottom of the flume —representing a real-world straight line across the entire frame— remained visually straight in the recordings as long as the GoPros were set to linear mode. Nevertheless, to quantitatively assess and confirm the extent of distortion, undistortion methods were applied. A Python script, available at the GitHub repository provided in Appendix G, using OpenCV was used to calibrate the cameras and correct for lens distortion.

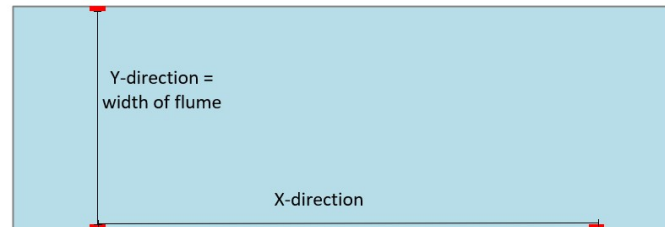
The calibration process began by shooting a calibration video in which the camera was set in place and a 9x7 checkerboard with 75mm squares was moved throughout the camera window in different locations and under varying angles. By extracting frames from the calibration video, the code mapped the 2D image coordinates of the squares on the board. This resulted in a set of object points (real-world coordinates) and image points (corresponding image coordinates), which were then used to estimate the specific camera parameters. The results of this were a camera matrix and distortion coefficients. These were applied to the videos, resulting in undistorted footage. The working calibration procedure was applied to multiple representative video recordings for the footage used in this research. A comparison between the original and the undistorted videos confirmed that the magnitude of distortion in these videos was in the order of millimetres, even at the edges of the camera's field of view where distortion was expected to be the most significant. Given the limited distortion observed and considering that the particle travel distances in this study are in the order of magnitude of meters, such a minor offset was deemed negligible. The videos used in this research were therefore not corrected for distortion.

## A.2. Distance Conversion

To establish an accurate relationship between recorded pixel distances and real-world distances, spatial reference markers were introduced into the experimental setup. Reference markers with

known real-world distances were placed on the interior glass walls of the flume in both the direction of the flume's length (x) and width (y) for the top-view cameras as can be seen in Figure A.1A. For the side-view cameras, the markings were made on the outside of the glass to mark once again in the direction of the length of the flume (x) and the height of the flume (z) as shown in figure A.1B. These markers were clearly visible in the video footage and served as fixed reference points, enabling the derivation of a pixel-to-real-world distance ratio. This approach allowed for consistent and accurate conversion of tracked particle positions from pixel coordinates to metric units across all recordings.

A. Top-View Flume



B. Side-View Flume

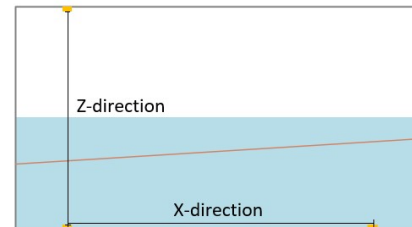
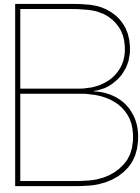


Figure A.1: Schematic showing the use of reference frames in the flume

**Legend:** 100% overlap 90% overlap with minimal adjustments 0% overlap





# Initial Testing and Setup Refinement

To gain a better understanding of the hydraulic dynamics within the flume and to establish a robust experimental procedure, the setup underwent a series of preliminary tests and adjustments.

## B.1. Spin-up Time

Prior to the experimental campaign, the spin-up time was estimated. The spin-up time refers to the time needed for the initial turbulence caused by the wave generation to decay in the flume. Once the wave maker was turned on, the paddle started moving forwards and backwards, pushing against the body of water. This initial motion introduced turbulence in the form of eddies and vortices near the paddle. A stabilisation period was required to allow these disturbances to propagate downstream towards the end of the flume, enabling the system to reach quasi-steady state along the length of the flume.

The time required to reach this steady state, the spin-up time, was estimated to be five minutes for the experimental setup used in this research. No experiments were conducted within these initial five minutes.

This estimation was based on observations using floating particles. A measurement window was established along the flume with a fixed distance  $x$ . Immediately after activating the wave generator, particles were released, and their travel time across this distance was measured over approximately 15 minutes. These measurements were conducted for wave conditions with a period of 1.5 seconds and wave heights of 0.05 m and 0.20 m. It was observed that the particles travel speed was highest during the first minutes, and after approximately four to five minutes, the travel speed stabilised. It was therefore decided to wait 5 minutes after starting the wave maker before beginning the experiments.

## B.2. Instrument Deployment Strategy

As outlined in Section 3.1.2, six wave gauges were placed along the flume length during this study. Prior to conducting the experiments, the target wave conditions were measured by running each case for 25 minutes: a 5-minute spin-up period to stabilise the wave field, followed by 20 minutes of measurements. This procedure generated wave data at six distinct locations along the flume for each wave condition. Following these measurements, wave gauges 2–6 were removed to prevent potential interference between the sensors and plastic particles during subsequent particle-tracking experiments. The assumption was made that the wave gauge data collected prior to particle deployment would remain representative of the wave conditions during the particle experiments, as the experimental set-up and settings of the wave maker remained the same during those experiments. To validate this assumption and collect additional wave condition data, the wave gauge placed at

Location 1 was kept in place during the particle experiments, as it was positioned behind the particle deployment location, avoiding any risk of sensor-particle interaction.

### B.3. Tipping point

During initial trial runs, it was observed that, following the spin-up period, floating particles introduced behind the shoaling zone experience a negative drift towards the wave generator. Specifically, particles placed further offshore (closer to the wave maker) in the flume consistently drifted towards the wave maker rather than in the onshore direction. This indicates the presence of a surface drift directed away from the beach. However, particles placed right before the breaking point of the wave all travelled towards the beach. It was thus observed that a tipping point appears to exist at which particles either drift onshore or offshore. The location of this tipping point—or tipping zone—relative to the breakpoint shifted further offshore as the wave height increased under constant wave period conditions.

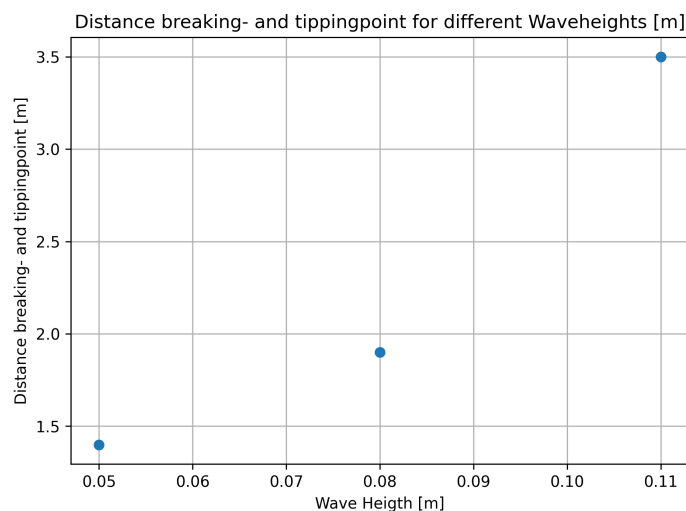


Figure B.1: The distance between the breaking and tipping point in meters expressed as a function of wave heights in the experimental set-up.

To give an indication, B.1 shows the distance between the breaking point and the estimated tipping point, or tipping zone, for several wave heights. It can be seen that as the wave height increases, the tipping point moves further offshore when compared to the breaking point. For wave heights of 0.17 metres or greater, all particles along the entire length of the flume appeared to travel towards the beach, with no negative surface drift observed at any location.

To better understand the dynamics in the flume, sinking particles were released. The sinking particles placed at the toe of the slope were observed to be moving forward towards the beach at increasing speed as they approached the breaking point. The particles were observed to collect at the breaking point, where they remained stationary. Sinking particles initially placed on the beach, downstream of the breaking point, travelled backwards towards the breaking zone until they also settled in that region. All sinking particles ultimately collected at the bottom of the flume at the wave breaking point.

Figure B.2 describes the observations made for the wave heights 0.05, 0.08 and 0.11 metres. As the wave height was increased, the breaking zone and tipping zone moved further offshore towards the wave generator, the general directions are described in Figure B.2. As previously mentioned, all sinking particles were observed to accumulate at the wave breaking point, referred to as the collection zone in the figure. Particles released beyond the tipping point tended to settle at the end of the slope, referred to here as the 'beach'. It is expected that particles transported in the backwards direction would accumulate near the wave maker, at the upstream end of the flume. However, the exact location of this potential collection zone could not be confirmed, as particles were retrieved

approximately three meters before reaching the wave maker for safety reasons.

### Surface and Bottom Drift

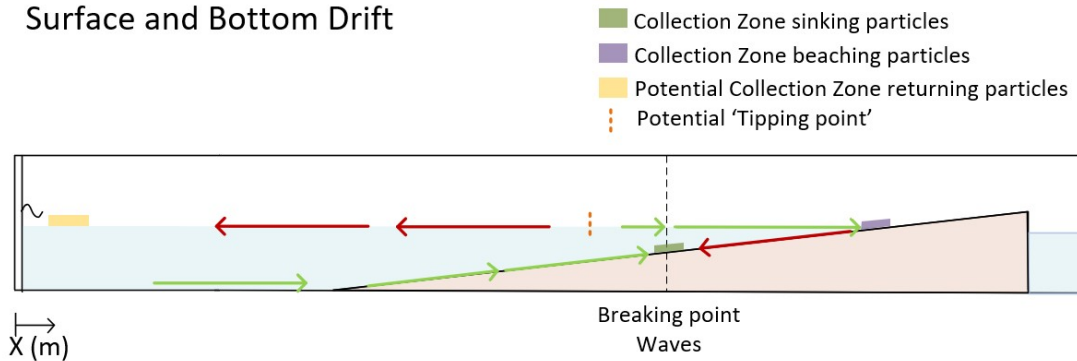


Figure B.2: Schematic of the drift directions observed for wave height 0.05 m, 0.08 and 0.11 m

Based on these observations, and considering the limitations imposed by the maximum length of the observation window, it was decided to release the floating plastic particles within the shoaling zone, one metre upstream of the wave breaking point. This placement consistently resulted in all particles reaching the beach. However, further research should be conducted investigating the vertical structure of the velocity profile. Understanding how surface and near-bed flows interact across different wave conditions could provide deeper insight into the mechanisms governing particle transport and accumulation within the flume, and would allow for a better understanding of how it relates to reality. However, this was beyond the scope of this research and is thus not further investigated in this report.

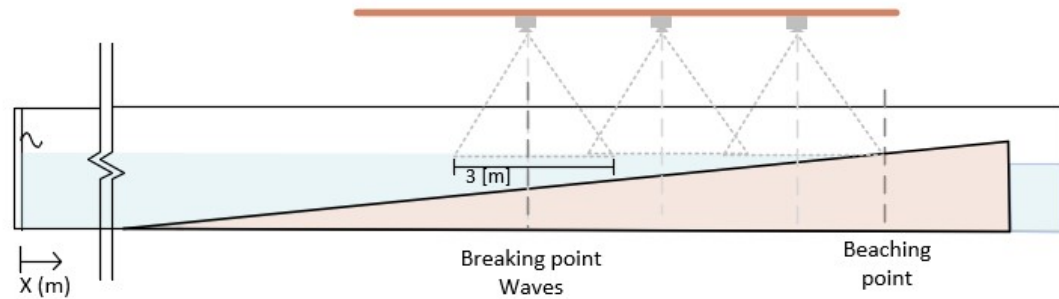
## B.4. Cameras Setup Variability Across Wave Conditions

The placement of the cameras along the flume (x-direction) was determined based on the beaching location and the breaking point location relevant to the seven wave conditions. To ensure continuous particle tracking, the camera view windows were strategically positioned to have an overlap between the different videos. This was not always possible due to the changing locations of the breaking points across the different wave conditions. For wave conditions W1 and W2, two top-view cameras provided complete coverage of a 6-meter stretch of the flume from the end of the shoaling zone until the end of the swash zone. For condition W3 three cameras were installed from the top and three from the side in order to cover the full length between end of the shoaling zone and the end of swash zone, covering a total stretch of 9 m. For conditions W4, W5, W6, W7, two of the top-view cameras were positioned with overlap filming the end of the shoaling zone, the breaking zone and the beginning of the surf zone, these were adjusted and moved for each wave condition based on the location of the breaking zone. The third top-view camera and side-view camera were kept fixed filming the swash zone for all the wave conditions. This resulted in 6-9 meters of the flume being filmed for all wave conditions. Specifically, for conditions W4, W5, W6, W7, for which the breaking point was located further upstream in the direction of the wave generator, a gap in coverage was left between the middle of the surf zone and the beginning of the swash zone.

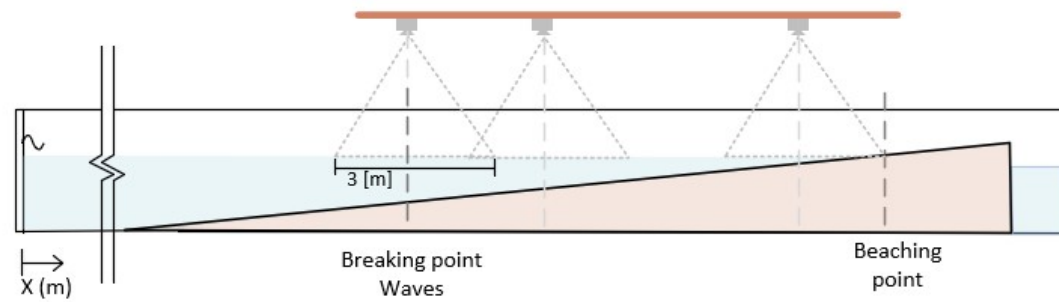
Figure B.3 shows the three different camera setups described above. Schematization A illustrates the setup used for wave condition W3, in which all three cameras had full overlap. Schematization B represents the setup used for conditions W4, W5, W6, W7 where there was partial overlap between the top-view camera capturing the end of the shoaling zone and the breaking zone and the top-view camera capturing the end of the breaking zone and the beginning of the surf zone. Schematization

C represents the setup used for wave conditions W1 and W2 for which the whole stretch between the end of the shoaling zone and the end of the swash zone was captured by only two overlapping cameras. For simplicity Figure B.3 does not report the side-view cameras as these were always placed in line with the top-view cameras as depicted in Figure B.3 as described in Section 3.1.3.

**A. Top-view Camera Setup (not to scale)**



**B. Top-view Camera Setup (not to scale)**



**C. Top-view Camera Setup (not to scale)**

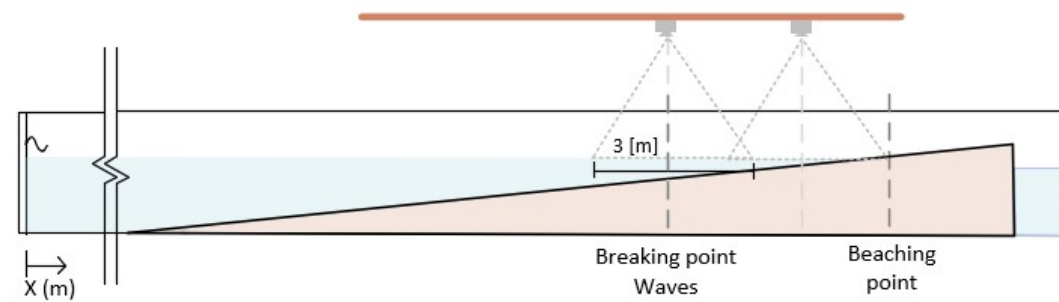
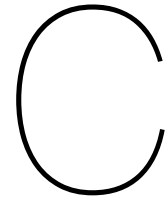


Figure B.3: Schematic representation of the three different top-view camera placement setups. Panel A applies for W3, panel B applies for W4, W5, W6, W7, panel C applies for W1 and W2.

**Legend:** ■ 100% overlap ■ 90% overlap with minimal adjustments ■ 0% overlap



# Preliminary Particle Drift Analysis

The transport behaviour of plastic particles within the flume was analysed based on multiple spatial scales. This section explores how this was done by first examining the computation of total travel velocities. The flume was then divided into hydrodynamic zones (shoaling, breaking, surf, and swash) and particle velocities were measured in each zone to better understand the difference along the x-direction.

## C.1. Total Travel Velocity

During the experimental campaign, the total travel time of each particle was manually recorded using a stopwatch, as outlined in Section 3.3. The moment of release in the shoaling zone and the moment of beaching—defined as the point at which the particle came to rest on the slope—were both noted down for each individual particle. A total of approximately 70-100 particles were measured for each wave condition, with the exception of wave condition W7, for which only 30 particles were used. The total travel distance covers the full extent of the nearshore zone, including the shoaling, breaking, surf, and swash zones. The travel time combined with the measured total travel distance allowed to get a first estimation of particle travel speed across the various wave conditions.

All manually recorded observations were transcribed and organised into their respective offshore steepness categories. For each category, mean travel speeds were calculated based on 30 to 100 observations. The obtained data is provided in Figure C.2 for wave conditions W1 - W7.

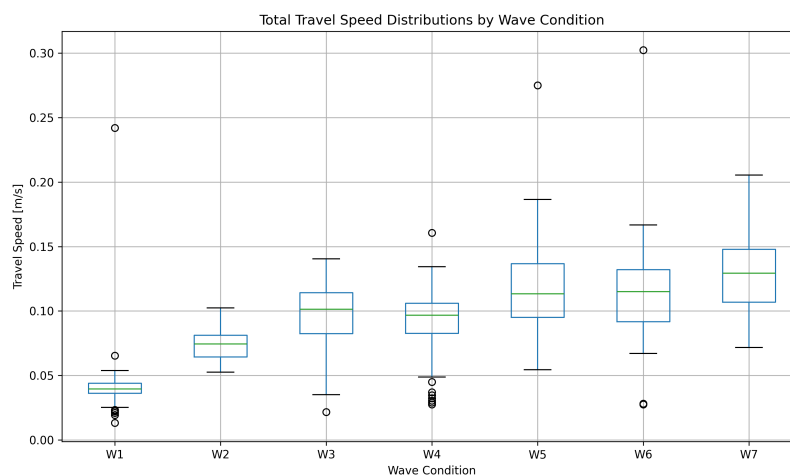


Figure C.1: Total travel speed for wave conditions W1 - W7 obtained from the manually measured travel times.

The data was used to calculate the mean travel time and travel speed for each category, as well as to assess the variability within categories. First, it was assessed whether the travel speed data followed a normal distribution using the Shapiro-Wilk test, applying a significance level of 0.05 (StatsKingdom 2024).

Once the nature of the distributions of the travel speed for each condition was assessed, a Kruskal–Wallis test was conducted (Wikipedia contributors 2024). This test is suitable for comparing more than two independent groups when the assumption of normality is not met. This initial statistical test was used to identify whether any of the categories showed significant differences in travel speed, which can indicate the need for more detailed pairwise comparisons in the following analysis.

When the Kruskal–Wallis test indicates that at least one group differs significantly in median, a more detailed pairwise analysis is required to determine which specific groups show statistically significant differences. This is done using the Mann–Whitney U test, a non-parametric test used to assess whether two independent samples originate from the same distribution (McClenaghan 2024). It is assumed that all observations are independent. The null hypothesis ( $H_0$ ) assumes that both groups have the same distribution, while the alternative hypothesis ( $H_1$ ) assumes that the distributions differ. The test is performed by pooling both groups, ranking all values, and then summing the ranks for each group. These rank sums are used to calculate the U statistic, which is then compared to a critical value to assess statistical significance. This process is repeated for each pair of groups.

The results of the Mann–Whitney U test are provided in Table C.1. The raw p-values have been adjusted using the Bonferroni correction, allowing for the comparison of multiple classes.

Most of the comparisons against W1 and W2 show extremely low p-values (order of magnitude  $10^{-08}$  -  $10^{-23}$ ) indicating that the distributions of this group differ significantly from all others. Comparisons involving W3 and W4 show generally weaker but still significant differences. In contrast, some comparisons (W5–W6, W5–W7, W6–W7, W3–W4) yield p-values which are not statistically different after the Bonferroni correction.

This analysis was intended to assess whether differences between the tested conditions existed. The results confirmed that such differences do exist and supported the continuation of the analysis.

| #  | Group 1 | Group 2 | U statistic | Raw p-value            | Bonferroni corrected p |
|----|---------|---------|-------------|------------------------|------------------------|
| 3  | W1      | W5      | 72.0        | $2.62 \times 10^{-24}$ | $5.51 \times 10^{-23}$ |
| 1  | W1      | W3      | 261.0       | $1.53 \times 10^{-22}$ | $3.22 \times 10^{-21}$ |
| 0  | W1      | W2      | 69.0        | $9.64 \times 10^{-21}$ | $2.02 \times 10^{-19}$ |
| 5  | W1      | W7      | 39.0        | $1.27 \times 10^{-17}$ | $2.67 \times 10^{-16}$ |
| 4  | W1      | W6      | 178.0       | $4.39 \times 10^{-17}$ | $9.22 \times 10^{-16}$ |
| 2  | W1      | W4      | 458.0       | $1.72 \times 10^{-16}$ | $3.61 \times 10^{-15}$ |
| 8  | W2      | W5      | 349.0       | $1.47 \times 10^{-14}$ | $3.09 \times 10^{-13}$ |
| 10 | W2      | W7      | 88.0        | $8.16 \times 10^{-14}$ | $1.71 \times 10^{-12}$ |
| 9  | W2      | W6      | 271.0       | $1.73 \times 10^{-11}$ | $3.62 \times 10^{-10}$ |
| 6  | W2      | W3      | 854.0       | $1.91 \times 10^{-08}$ | $4.02 \times 10^{-07}$ |
| 17 | W4      | W7      | 446.5       | $7.35 \times 10^{-08}$ | $1.54 \times 10^{-06}$ |
| 7  | W2      | W4      | 711.5       | $1.11 \times 10^{-07}$ | $2.33 \times 10^{-06}$ |
| 14 | W3      | W7      | 688.0       | $2.01 \times 10^{-06}$ | $4.23 \times 10^{-05}$ |
| 15 | W4      | W5      | 1219.0      | $8.94 \times 10^{-06}$ | $1.88 \times 10^{-04}$ |
| 16 | W4      | W6      | 792.0       | $3.22 \times 10^{-05}$ | $6.75 \times 10^{-04}$ |
| 12 | W3      | W5      | 1791.0      | $4.57 \times 10^{-04}$ | $9.60 \times 10^{-03}$ |
| 13 | W3      | W6      | 1196.0      | $1.59 \times 10^{-03}$ | $3.34 \times 10^{-02}$ |
| 19 | W5      | W7      | 1053.0      | $4.89 \times 10^{-02}$ | 1.00                   |
| 11 | W3      | W4      | 2847.5      | $7.74 \times 10^{-02}$ | 1.00                   |
| 18 | W5      | W6      | 1690.0      | $8.05 \times 10^{-01}$ | 1.00                   |
| 20 | W6      | W7      | 688.0       | $4.79 \times 10^{-02}$ | 1.00                   |

Table C.1: Mann–Whitney U test results between wave groups.

## C.2. Zonal Travel Velocity

After assessing the total travel velocity, a further step in the processing and analysis phase consisted of dividing the flume into three main zones (breaking, surf, swash) and computing the travel velocity of a sample of particles for each zone. For this purpose some of the top-view videos were visually inspected. The goal was to detect a potential trend in travel velocity within specific zones of the flume. To achieve this, the minimum number of trajectories required to identify a significant difference between the tested conditions was analysed. As a result, the trajectories of five particles for each wave steepness step/relative density step were manually observed.

The first step in this processing phase was to define the different zones based on visual observation of the videos. The breaking zone was defined as the area beginning approximately 50 cm before the wave breaking point (identified by visible deposits of sinking particles on the flume bed) and ending with the wave collapsing on itself, which was marked by the first appearance of white water at the crest of the wave. The beginning of the surf zone coincided with the end point of the breaking zone and extended until the last bore with a recognisable sinusoidal shape broke. This marked the transition from the surf zone to the swash zone, characterised by waves that no longer resembled a typical sinus form. The end of the swash zone was then identified as the location where the plastic particles stabilised and were defined as "beached".

This procedure was repeated for all the different wave conditions and therefore offshore steepness steps, for which the breaking point and subsequently all the following edges of the zones would change. This resulted in seven different definitions of the breaking, surf and swash zone for each tested wave condition.

Five particles were manually observed travelling the flume across the three zones for wave conditions W1, W4, W6. The time a particle entered and left each zone was recorded and the travel time for each zone was computed. This was then divided by the length of the relevant zone to obtain the zonal travel velocity. This was done to better understand whether the observed variation in total travel velocity computed according to Section C.1, could be linked to a specific location along the length of the flume and therefore a different moment in the wave evolution.

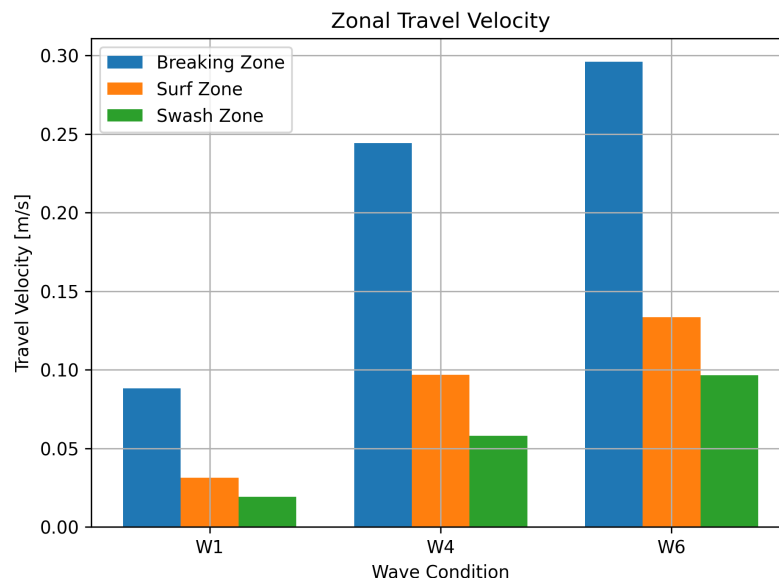


Figure C.2: Zonal travel speed for wave conditions W1, W4, W6.

As this preliminary result was produced before the actual data processing and the definition of the final methods for the analysis, the particles zonal travel velocities were computed in the breaking, surf and swash zone. It was then decided to focus on the shoaling, breaking and surf zones. Nonethe-

less, the result serves its purpose of assessing the presence of differences in travel velocity across different domains. It can be observed that the highest speed values are recorded in the breaking zone across the three tested conditions and that the speed values tend to increase when offshore steepness is increased, from W1 to W6.

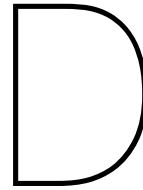
The presented preliminary results supported the decision to proceed with further analysis, as differences in particles horizontal speed were observed across both the tested wave conditions and the considered spatial domains.

---

**Legend:**  100% overlap  90% overlap with minimal adjustments  0% overlap

---





# SWASH Model

In the context of this study, a SWASH model was used to simulate the experimental wave conditions within the flume. This was done in order to fully understand the wave dynamics in the longitudinal direction for all investigated wave conditions. In this appendix the input file provided to the model is described to allow reproducibility of the methodology presented in Chapter 3.

## D.1. Model Input

The user should provide SWASH with a number of files containing the following information:

- A file containing the instructions of the user to SWASH (the command file);
- File(s) containing: grid, bottom, (initial) current and water level;
- File(s) containing boundary conditions.

The mentioned files are made available in a GitHub repository accessible from Appendix G.

### D.1.1. Command File

The command file is a plain text input file which contains all the necessary instructions to define:

- Simulation type
- Domain geometry
- Physical settings
- Boundary conditions
- Output options

An example of an input file (H11.sws) is provided below in Figure D.1. This specific input file was created to simulate regular waves with a wave height of 0.11 m and a wave period of 1.5 seconds propagating over a sloped bottom of 1:40.

A brief description of the input commands is provided below, more information can be found in the software manual available at Team (2025).

1. Definition of computational grid: The model is defined in 1D mode with normally incident waves propagating over a uniform beach. The simulation extent origin is set at  $x = 0$  and reaches up

- to  $x = 35$  m with 350 computational cells. In the vertical direction, a three-layer discretisation is applied.
2. Definition of bottom profile: the bathymetry of the flume is provided to the model by the file "bed\_profile.bot".
  3. Physics: Some physical features are specified. The mode is set to non-hydrostatic, the breaking model is activated and a standard friction coefficient is specified.
  4. Boundary conditions: the still water level is specified and set to 0.5 m. The boundary condition definition line specifies the location of the boundary to be on the West side (W) of the domain with a counter-clockwise direction (CCW). Continuous regular waves are programmed (CON REG) representing the monochromatic wave input with a wave height of 0.109 meters (in accordance with the mean wave height computed from the experimental data) and a period of 1.5 seconds.
  5. Output request(s): six measuring locations are defined following the real experimental setup.
    - The "POINT" command defines a point output with a specified name and location in the longitudinal direction. The variables time in seconds (TSEC), surface elevation (WATLEV) and velocity (VEL) are requested as output for every point and stored every 0.05 seconds ( $F_s = 20$  Hz) in a ".tbl" file. This pattern is repeated for gauges 1 to 6 at different positions following the experimental setup described in Section 3.1.2.
    - The "GROUP" command defines a group of points over a subgrid from cell 1 to 350 in x-direction. The variables time in seconds (TSEC), x-position (XP), surface elevation (WATLEV), bed elevation (BOTLEV), velocity (VEL) and water depth (DEPTH) are simulated every 0.05 seconds ( $F_s = 20$  Hz). This output provides the continuous wave dynamics over the longitudinal direction.

```

!*****HEADING*****
! H11, T1.5
!*****MODEL INPUT*****

MODE ONEDIMENSIONAL
CGRID 0. 0. 0. 35. 0. 350 0 (1)
VERT 3

INPGRID BOTTOM 0. 0. 0. 1750 0 0.02 0. (2)
READINPUT BOTTOM 1. 'bed_profile.bot' 1 0 FREE

NONHYDROSTATIC
BREAK
VISCOSITY VERTICAL KEPS (3)
FRIC MANNING 0.019

SET LEVEL = 0.50 (4a)

BOUNDcond SIDE W CCW BTYPE WEAK ADDBoundwave CON REG 0.109 1.5 (4b)

DISCRET UPW MOM
TIMEI 0.4 0.8

!***** OUTPUT REQUESTS ***** (5)

POINTS 'GAUGE1' 6. 0
TABLE 'GAUGE1' HEAD 'gauge1.tbl' TSEC WATLEV VEL OUTPUT 000000.000 0.05 SEC

POINTS 'GAUGE2' 14. 0
TABLE 'GAUGE2' HEAD 'gauge2.tbl' TSEC WATLEV VEL OUTPUT 000000.000 0.05 SEC

POINTS 'GAUGE3' 15.25 0
TABLE 'GAUGE3' HEAD 'gauge3.tbl' TSEC WATLEV VEL OUTPUT 000000.000 0.05 SEC

POINTS 'GAUGE4' 19.15 0
TABLE 'GAUGE4' HEAD 'gauge4.tbl' TSEC WATLEV VEL OUTPUT 000000.000 0.05 SEC

POINTS 'GAUGE5' 22.5 0
TABLE 'GAUGE5' HEAD 'gauge5.tbl' TSEC WATLEV VEL OUTPUT 000000.000 0.05 SEC

POINTS 'GAUGE6' 27 0
TABLE 'GAUGE6' HEAD 'gauge6.tbl' TSEC WATLEV VEL OUTPUT 000000.000 0.05 SEC

GROUP 'grp' SUBGrid 1 350 1 1
TABLE 'grp' NOHEAD 'grid_output.tbl' TSEC XP WATLEV BOTLEV VEL DEPTH OUTPUT 000000.000 0.05 SEC

COMPUTE 000000.000 0.05 SEC 002000.000 (6)

STOP

```

Figure D.1: Example of SWASH input file.

**Legend:** 100% overlap 90% overlap with minimal adjustments 0% overlap



## YOLO Detection Model

The performance metrics of the trained YOLO model used to detect yellow, green and pink particles from the footage relative to the experimental runs are provided in this appendix.

The normalized confusion matrix presented in Figure E.1 shows that each class is predicted with high accuracy ( $\geq 92\%$ ). However, a significant fraction of background pixels are misclassified as objects, specifically 37% for yellow and 31% for green and pink. This indicates some degree of over-detection, particularly in background regions affected by the presence of the yellow tape on the bottom.

Overall, the model performance in detecting particles of different colours is considered strong, supporting its use for the purposes of the current research.

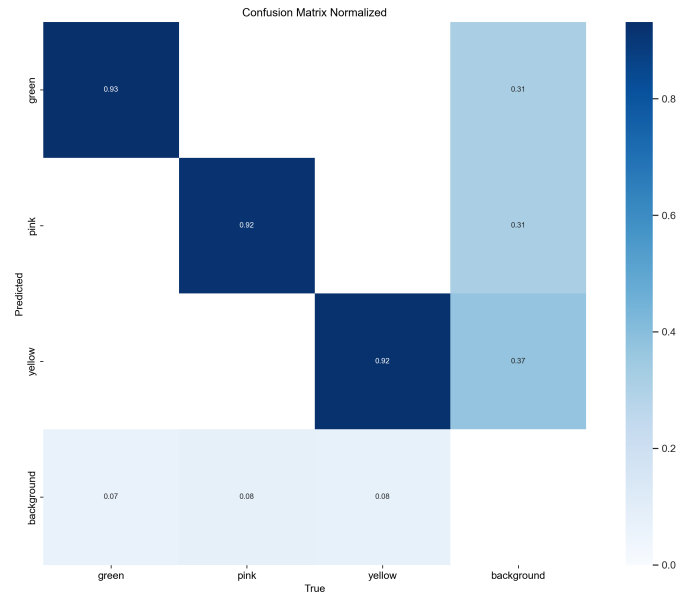



Figure E.1: Normalized confusion matrix showing classification performance across all four classes.

Several setup-specific factors affected particle tracking during the experiments. The bottom of the flume contained neon yellow tape lines, which ensured continuity between wooden panels; this interfered with the correct recognition of some of the particles, which were coated with a very similar yellow shade. The presence of multiple particles in close proximity caused issues in the detection,

which happened especially near the beaching area, where particles would accumulate. The presence of shading at the sides of the flume caused additional problems in tracking, as the appearance of the objects in the footage was affected by the varying light conditions. Finally, particles undergoing the most energetic wave conditions would get lost under the waves at breaking, preventing the tracking tool from detecting them correctly. The issues encountered during the current experimental campaign are acknowledged to inform and improve future repetitions of this methodology.

---

**Legend:**  100% overlap  90% overlap with minimal adjustments  0% overlap

---



# Results

## F.1. SWASH Model Output Validation

This section provide supplementary results of the validation of the obtained hydrodynamic conditions simulated by SWASH. A comparison between measured and simulated wave heights is presented in tabular form, reporting the mean values, standard deviations, and relative differences for each wave condition (W1–W7) and measurement location (Locations 1–6).

In addition, power spectral density plots are presented in Figure F.1 for wave conditions W1 - W7 at Locations 1 -6.

Table F.1: Comparison of measured and SWASH mean water levels — W1

| Location | Measured Mean [m] | Measured Std [m] | SWASH Mean [m] | SWASH Std [m] | Rel. Diff. [%] |
|----------|-------------------|------------------|----------------|---------------|----------------|
| Loc1     | 0.0482            | 0.0004           | 0.0476         | 0.0000        | 1.18           |
| Loc2     | 0.0474            | 0.0004           | 0.0484         | 0.0000        | 2.06           |
| Loc3     | 0.0479            | 0.0005           | 0.0484         | 0.0000        | 1.04           |
| Loc4     | 0.0418            | 0.0197           | 0.0504         | 0.0000        | 20.53          |
| Loc5     | 0.0572            | 0.0005           | 0.0540         | 0.0000        | 5.55           |
| Loc6     | 0.0162            | 0.0037           | 0.0381         | 0.0000        | 135.76         |

Table F.2: Comparison of measured and SWASH mean water levels — W2

| Location | Measured Mean [m] | Measured Std [m] | SWASH Mean [m] | SWASH Std [m] | Rel. Diff. [%] |
|----------|-------------------|------------------|----------------|---------------|----------------|
| Loc1     | 0.0779            | 0.0005           | 0.0722         | 0.0001        | 7.21           |
| Loc2     | 0.0786            | 0.0005           | 0.0739         | 0.0000        | 6.06           |
| Loc3     | 0.0780            | 0.0007           | 0.0737         | 0.0000        | 5.56           |
| Loc4     | 0.0657            | 0.0357           | 0.0761         | 0.0000        | 15.80          |
| Loc5     | 0.0992            | 0.0019           | 0.0815         | 0.0000        | 17.81          |
| Loc6     | 0.0121            | 0.0069           | 0.0449         | 0.0000        | 271.12         |

Table F.3: Comparison of measured and SWASH mean water levels — W3

| Location | Measured Mean [m] | Measured Std [m] | SWASH Mean [m] | SWASH Std [m] | Rel. Diff. [%] |
|----------|-------------------|------------------|----------------|---------------|----------------|
| Loc1     | 0.1086            | 0.0005           | 0.1070         | 0.0004        | 1.46           |
| Loc2     | 0.1080            | 0.0006           | 0.1084         | 0.0007        | 0.40           |
| Loc3     | 0.1096            | 0.0008           | 0.1081         | 0.0006        | 1.36           |
| Loc4     | 0.1227            | 0.0092           | 0.1163         | 0.0008        | 5.21           |
| Loc5     | 0.0868            | 0.0070           | 0.1133         | 0.0006        | 30.57          |
| Loc6     | 0.0137            | 0.0078           | 0.0350         | 0.0001        | 156.25         |

Table F.4: Comparison of measured and SWASH mean water levels — W4

| Location | Measured Mean [m] | Measured Std [m] | SWASH Mean [m] | SWASH Std [m] | Rel. Diff. [%] |
|----------|-------------------|------------------|----------------|---------------|----------------|
| Loc1     | 0.1379            | 0.0007           | 0.1328         | 0.0028        | 3.69           |
| Loc2     | 0.1400            | 0.0010           | 0.1331         | 0.0020        | 4.90           |
| Loc3     | 0.1423            | 0.0014           | 0.1313         | 0.0020        | 7.70           |
| Loc4     | 0.1594            | 0.0227           | 0.1422         | 0.0027        | 10.78          |
| Loc5     | 0.0651            | 0.0120           | 0.0875         | 0.0030        | 34.42          |
| Loc6     | 0.0187            | 0.0064           | 0.0403         | 0.0009        | 115.70         |

Table F.5: Comparison of measured and SWASH mean water levels — W5

| Location | Measured Mean [m] | Measured Std [m] | SWASH Mean [m] | SWASH Std [m] | Rel. Diff. [%] |
|----------|-------------------|------------------|----------------|---------------|----------------|
| Loc1     | 0.1703            | 0.0011           | 0.1632         | 0.0058        | 4.18           |
| Loc2     | 0.1753            | 0.0024           | 0.1792         | 0.0056        | 2.21           |
| Loc3     | 0.1719            | 0.0018           | 0.1737         | 0.0048        | 1.09           |
| Loc4     | 0.1153            | 0.0362           | 0.1328         | 0.0122        | 15.24          |
| Loc5     | 0.0632            | 0.0147           | 0.0792         | 0.0034        | 25.38          |
| Loc6     | 0.0207            | 0.0046           | 0.0503         | 0.0006        | 142.63         |

Table F.6: Comparison of measured and SWASH mean water levels — W6

| Location | Measured Mean [m] | Measured Std [m] | SWASH Mean [m] | SWASH Std [m] | Rel. Diff. [%] |
|----------|-------------------|------------------|----------------|---------------|----------------|
| Loc1     | 0.2018            | 0.0016           | 0.1980         | 0.0046        | 1.88           |
| Loc2     | 0.2039            | 0.0027           | 0.1920         | 0.0072        | 5.83           |
| Loc3     | 0.2091            | 0.0040           | 0.1875         | 0.0065        | 10.32          |
| Loc4     | 0.0772            | 0.0418           | 0.1009         | 0.0082        | 30.74          |
| Loc5     | 0.0683            | 0.0162           | 0.0920         | 0.0062        | 34.74          |
| Loc6     | 0.0227            | 0.0049           | 0.0583         | 0.0046        | 157.28         |

Table F.7: Comparison of measured and SWASH mean water levels — W7

| Location | Measured Mean [m] | Measured Std [m] | SWASH Mean [m] | SWASH Std [m] | Rel. Diff. [%] |
|----------|-------------------|------------------|----------------|---------------|----------------|
| Loc1     | 0.2336            | 0.0024           | 0.2354         | 0.0040        | 0.79           |
| Loc2     | 0.2376            | 0.0042           | 0.1594         | 0.0048        | 32.90          |
| Loc3     | 0.1645            | 0.0121           | 0.1313         | 0.0110        | 20.17          |
| Loc4     | 0.0777            | 0.0371           | 0.1358         | 0.0147        | 74.73          |
| Loc5     | 0.0859            | 0.0100           | 0.1158         | 0.0163        | 34.83          |
| Loc6     | 0.0241            | 0.0064           | 0.0483         | 0.0114        | 100.18         |



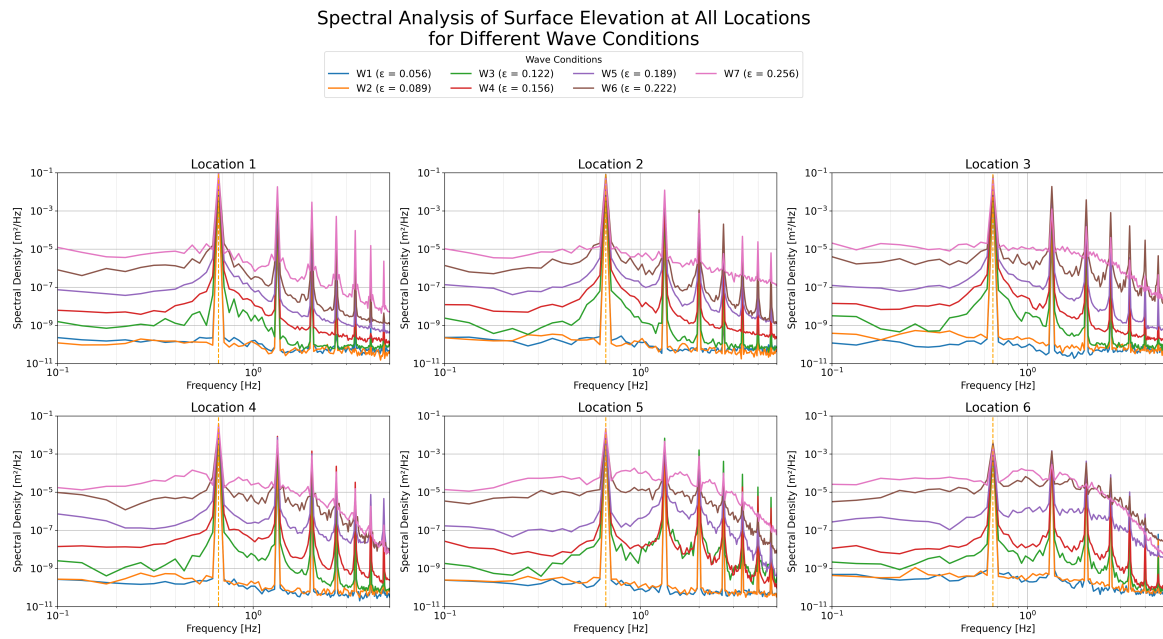


Figure F.1: Spectral analysis of surface elevation at all 6 measurement locations for different wave conditions (W1–W7). Each curve represents the SWASH-computed wave spectrum at a given location under a specific offshore wave steepness  $\epsilon$ . The vertical dashed line indicates the frequency  $f = 2/3$  Hz.

**Legend:** ■ 100% overlap ■ 90% overlap with minimal adjustments ■ 0% overlap





## Code and Data Availability

The main Python scripts used in the context of this research are made available at the following GitHub repository:

[https://github.com/camicocozza/Cocozza\\_Swuste\\_MSc\\_Plastic\\_Beaching.git](https://github.com/camicocozza/Cocozza_Swuste_MSc_Plastic_Beaching.git)

It includes:

- "Camera calibration" folder: contains a Jupyter notebook used to perform camera calibration and assess the level of image distortion.
- "YOLO\_Tracking" folder: contains the necessary scripts to perform particle tracking as described in Section 3.6.3. Additionally, the trained model is attached to allow for reproducibility of the current methodology.
- "SWASH" folder: contains the input files necessary to run the SWASH simulations.

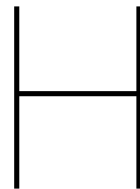
These Python scripts were developed collaboratively by Camilla Cocozza and Leanne Swuste.

---

**Legend:**  100% overlap  90% overlap with minimal adjustments  0% overlap

---





## Contribution Statement

This research serves as the foundation for an individual MSc thesis and is therefore presented as a singular document. However, the methodology applied in this study was developed jointly by Camilla Cocozza and Leanne Swuste, and large parts of the Theoretical Background and Methodology chapters within this document were written in collaboration. To acknowledge these shared contributions, this appendix provides a detailed overview of the individual inputs to ensure transparency and clarity for the reader.

A colour-coding system is used throughout this document to indicate individual contributions. A coloured line on the left side of the text identifies which author(s) were responsible for each section.

1. **Complete overlap:** These sections were written in collaboration between both authors and overlaps exactly between the two MSc thesis reports. The individual contribution of both students is within these exactly overlapping texts can be found below in table H.1
2. **Partial Overlap:** These sections were originally written in collaboration by both authors but was later adapted slightly to align with the specific research questions addressed in each thesis. While the core content remains largely the same (with approximately 85–95% overlap), minor modifications and additions were made to tailor the text to each research topic. A breakdown of individual contributions within these sections is provided in the table H.1.
3. **Individual:** These sections are written individually for each report by the respective author. These sections are specific for the topic addressed in this report.

Table H.1: Overview of Chapter Contributions and Feedback

| Section                        | Written by            | Feedback from |
|--------------------------------|-----------------------|---------------|
| Marine Plastic Debris          | Contributions of both | x             |
| Wave Basics                    | Contributions of both | x             |
| Coastal Wave Dynamics          | Contributions of both | x             |
| Wave Propagation Velocities    | Contributions of both | x             |
| Experimental Facility          | Camilla               | Leanne        |
| Wave Gauges                    | Camilla               | Leanne        |
| Electromagnetic Flow Meter     | Camilla               | Leanne        |
| Camera Setup                   | Leanne                | Camilla       |
| Spin-up Time                   | Leanne                | Camilla       |
| Instrument Deployment Strategy | Leanne                | Camilla       |
| Tipping Point                  | Leanne                | Camilla       |
| Experimental Procedure         | Camilla               | Leanne        |
| Hydrodynamic Conditions        | Leanne                | Camilla       |
| Swash Model                    | Camilla               | Leanne        |
| Particle detection YOLO        | Leanne                | Camilla       |
| Tracking Algorithm             | Camilla               | Leanne        |
| Trajectory Validation          | Camilla               | Leanne        |
| Trajectory Processing          | Camilla               | Leanne        |
| Phase Speed                    | Leanne                | Camilla       |
| Crest Speed                    | Leanne                | Camilla       |
| Stokes Drift                   | Camilla               | Leanne        |
| Total Travel Velocity          | Leanne                | Camilla       |
| Zonal Travel Velocity          | Camilla               | Leanne        |
| Swash Model                    | Camilla               | Leanne        |

**Legend:**  100% overlap  90% overlap with minimal adjustments  0% overlap